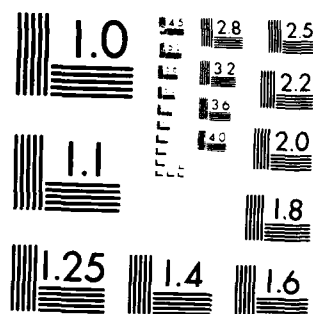


ADVANCED CONCEPTS THEORY ANNUAL REPORT 1983(U) NAVAL
RESEARCH LAB WASHINGTON DC J P APRUZESE ET AL.
18 MAY 84 NRL-MR-5330 SBI-AD-E000 573

1/2

F/G 7/4

NL



MICROCOPY RESOLUTION TEST CHART
NATIONAL BUREAU OF STANDARDS-1963-A

ADE000573

(2)

NRL Memorandum Report 5330

Advanced Concepts Theory Annual Report 1983

*Plasma Radiation Branch
Plasma Physics Division*

AD-A142 825

May 18, 1984

This research was sponsored by the Defense Nuclear Agency under Subtask T99QAXLA, work unit 00037 and work unit title "Advanced Concepts."



RECEIVED
JUN 01 1984
E

NAVAL RESEARCH LABORATORY
Washington, D.C.

Approved for public release; distribution unlimited.

UTC FILE COPY

84 06 29 084

AD-AM-2025

REPORT DOCUMENTATION PAGE				
1a REPORT SECURITY CLASSIFICATION UNCLASSIFIED		1b RESTRICTIVE MARKINGS		
2a SECURITY CLASSIFICATION AUTHORITY		3 DISTRIBUTION AVAILABILITY OF REPORT		
2b DECLASSIFICATION/DOWNGRADING SCHEDULE		Approved for public release; distribution unlimited.		
4 PERFORMING ORGANIZATION REPORT NUMBER: NRL Memorandum Report 5330		5 MONITORING ORGANIZATION REPORT NUMBER:		
6a NAME OF PERFORMING ORGANIZATION Naval Research Laboratory	6b OFFICE SYMBOL <i>If applicable:</i> Code 4720	7a NAME OF MONITORING ORGANIZATION		
6c ADDRESS (City, State and ZIP Code) Washington, DC 20375		7b ADDRESS (City, State and ZIP Code)		
8a NAME OF FUNDING SPONSORING ORGANIZATION Defense Nuclear Agency	8b OFFICE SYMBOL <i>If applicable:</i>	9 PROCUREMENT INSTRUMENT IDENTIFICATION NUMBER		
8c ADDRESS (City, State and ZIP Code) Washington, DC 20305		10 SOURCE OF FUNDING NOS		
		PROGRAM ELEMENT NO 62715H	PROJECT NO	TASK NO
11 TITLE (Include Security Classification) (See page ii)				WORK UNIT NO 147-0857-03
12 PERSONAL AUTHOR(S) Plasma Radiation Branch				
13a TYPE OF REPORT Annual Report	13b TIME COVERED FROM 1/83 TO 12/83	14 DATE OF REPORT (Yr. Mo., Day) May 18, 1984		15 PAGE COUNT 130
16 SUPPLEMENTARY NOTATION This research was sponsored by the Defense Nuclear Agency under Subtask T99QAXLA, work unit 00037 and work unit title "Advanced Concepts."				
17 COSATI CODES		18 SUBJECT TERMS (Continue on reverse if necessary and identify by block number)		
FIELD	GROUP	SUB GR		
		Radiation		
		Hydrodynamics		
		Plasma		
		Mixtures		
19 ABSTRACT (Continue on reverse if necessary and identify by block number) Results are presented on a variety of research activities concerned with investigating the radiative properties and x-ray conversion efficiency of dense hot plasmas. In this volume are analyses, discussions and numerical simulations on scaling laws for K-shell line power in Z-pinch plasmas, ionization dynamics and diagnostics, atomic processes, ion beam target interactions, and the radiative behavior of mixtures and their potential application as enhanced radiators.				
20 DISTRIBUTION AVAILABILITY OF ABSTRACT UNCLASSIFIED UNLIMITED X SAME AS RPT DTIC USERS		21 ABSTRACT SECURITY CLASSIFICATION UNCLASSIFIED		
22a NAME OF RESPONSIBLE INDIVIDUAL J. Davis		22b TELEPHONE NUMBER <i>(include Area Code)</i> (202) 767-3278	22c OFFICE SYMBOL Code 4720	

SECURITY CLASSIFICATION OF THIS PAGE

11. TITLE (Include Security Classification)

ADVANCED CONCEPTS THEORY ANNUAL REPORT 1983

SECURITY CLASSIFICATION OF THIS PAGE

CONTENTS

INTRODUCTION	1
DETAILED MODELING AND APPROXIMATE SCALING LAWS FOR K-SHELL LINE POWER IN Z-PINCH PLASMAS	2
IONIZATION DYNAMICS AND DIAGNOSTICS	16
DETAILED MODELING OF IONIZATION/RADIATION IN DENSE PLASMAS	35
DIELECTRONIC RECOMBINATION OF KRYPTON IONS	70
COUPLED PLASMA AND RADIATION TRANSPORT ION BEAM CODE	76
ENHANCED RADIATION SOURCES	111

Accession For	
NTIS GRA&I	<input checked="" type="checkbox"/>
DTIC TAB	<input type="checkbox"/>
Unannounced	<input type="checkbox"/>
Justification	
By _____	
Distribution/ _____	
Availability Codes	
Dist	Special
A-1	



ADVANCED CONCEPTS THEORY ANNUAL REPORT 1983

INTRODUCTION

The objectives of the Advanced Concepts Theory Program at the Naval Research Laboratory are to develop a variety of theoretical models, tools, and computational strategies to understand, guide, and predict the behavior of high brightness, laboratory x-ray plasma sources designed to simulate nuclear weapons effects. Specifically, to develop the capability to determine self-consistently the radiative properties of different materials in a variety of geometrical configurations that occur in exploding wire, gas puff, and pellet implosion experiments. These theoretical models must treat hard and soft x-ray emission from different electron configurations with K, L, and M shells, and they must include accurate treatments of the different broadening mechanisms that contribute to the emission and absorption profiles. The self-consistency of these nonlinear models is critical if they are to be used to (1) accurately diagnose both ongoing experiments and calculations and (2) properly understand the energy flow and partitioning that occurs during energy absorption, implosion, and x-ray emission. Such models can then be employed to interpret, explain, and guide present day experiments, on the one hand, and to predict how these experiments should be scaled with improved x-ray conversion efficiency to higher energy and power output levels on the other

In this report we will focus primarily on those activities not dealing with load dynamics which will appear in a separate report, but instead will focus on ion beam target interaction, ionization dynamics and radiation physics. Since a number of papers are published each year in the open literature emphasizing the emission/absorption physics and radiation transport aspects of the program, it was decided to omit lengthy discussion of these activities here and refer the reader to the open literature for the details.

Finally, this report represents the combined efforts of a number of people, namely, J. Davis, D. Duston, P. Kepple, J. Apruzese, R. Clark, J. Rogerson, V. Jacobs and F. Cochran (of Berkeley Research Associates). We would also like to acknowledge the assistance of Maxwell Laboratory for providing the data analyzed in this report; in particular to M. Gersten for making the reduced spectral data available.

Manuscript approved March 2, 1984.

A. Detailed Modeling and Approximate Scaling Laws for K-Shell Line
Power in Z-Pinch Plasmas

I. INTRODUCTION

Substantial progress was registered in two important areas directly relating to the x-ray yield obtained from high-energy Z pinch plasmas. For the first time the effects of fine structure opacity profiles on emission in hydrogen-like lines have been calculated. These effects were found to be of considerable importance for any future machines in the 50 TW or higher power range, although the Voigt profile approximation we have employed all along was found to be valid for present and earlier generations of pulsed-power devices.

Additionally, the analytic scaling law for K-shell yield which was developed previously for argon has been successfully extended to all low-to-medium Z elements. This scaling law gives the K-shell yield in kilojoules as a function of such plasma parameters as temperature and density. The next step is to couple such analytic expressions for accurate radiation yields to simplified hydrodynamics models in the effort to achieve a precise overall yield scaling law in terms of machine parameters.

II. DETAILED OPACITY MODELING

The effects of hydrogen-like line fine structure profiles may at first appear to be a minor, irrelevant physical detail. However, it turns out to be of substantial importance for contemplated future machines where the plasma optical depths would be substantially higher than those achieved to date. Each Lyman line has normally been modeled as a single line whose opacity is characterized by one Voigt profile. However, the single "line" is in reality two lines separated by as much as several thermal Doppler widths. The more realistic calculation of photon absorption therefore involves less opacity spread out over a greater frequency range. The true absorption is the superposition of two Voigt profiles whose separation varies both as a function of atomic number and the exact Lyman line under consideration. Obviously, the higher the optical depth, the greater is the

photon absorption and the more critical a precise description of the opacity becomes.

Complete details of our investigation are presented in the Appendix A, "Influence of Lyman Series Fine Structure Opacity on the K-Shell Spectrum and Level Populations of Low-to-Medium Z Plasmas." The finding most relevant to DNA applications is that the effect of the reduced opacity would produce power output enhancements of 30-50% in the principal hydrogen-like lines for plasmas of optical depths 5-10 times greater than those produced with present machines. Thus the construction of more powerful machines capable of producing these larger plasma masses could well result in even greater K-shell yields than indicated by extrapolations from opacity modeling which does not include this effect. The Lyman-line power enhancements are quite clearly seen in the line ratio curves presented in Figs. 3 and 5 of the Appendix a.

An additional result of this investigation is the discovery of a potentially valuable, independent plasma density diagnostic. In general for typical Z-pinch conditions, spectroscopic diagnosis of plasma density is far more difficult than that of temperature. In many cases, Z pinch plasmas produced by DNA machines are subjected to a density diagnosis based on matching the measured yield and size with the required density. As is illustrated in Fig. 6 of the Appendix A, the emitted Lyman- α line profile varies quite sensitively with density. To exploit this potential, however, development of spectrometers with spectral resolution of 1-2 mÅ will be required, regardless of the plasma element excited in the device.

III. ANALYTIC SCALING OF K-SHELL YIELDS

In the FY82 final report an analytic expression for predicting the K-shell yield of argon gas puff implosions was presented. This expression agrees within 10% with both detailed code predictions and experimental measurements for each of the 30 spatial elements in the most elaborately and completely diagnosed argon shot. In terms of the plasma radiating time t (in ns), the axial length l (in cm), the diameter d (in mm), the ion density N (cm^{-3}) and temperature T (in KeV), the argon K-shell yield is given as

$$Y(kJ) = 142 \left(\frac{t}{15}\right) \left(\frac{\ell}{3}\right) \left(\frac{N}{3.7 \times 10^{19}}\right)^{1.9} \left(\frac{d}{1.34}\right)^2 \exp\left(\frac{-2.0}{T}\right) \min\left(1, \frac{2.0}{T}\right) \quad (1)$$

We have generalized Eq. (1) to apply to arbitrary atomic number Z through use of basic atomic data and its scalings. Favorable comparison of yields for neon, aluminum, and titanium as well as argon has been achieved.

The temperature at which K-shell ions dominate the species of a plasma of atomic number Z scales as Z^2 . Therefore, the temperature functions of Eq. (1) - developed only for argon with $Z = 18$ - may be generalized to

$$\exp\left(-2.0 \left(\frac{Z}{18}\right)^2 / T\right) \min\left(1, 2.0 \left(\frac{Z}{18}\right)^2 / T\right) \quad (2)$$

The line photon energies themselves for analogous K-shell lines also scale as Z^2 . Assume for the moment that a plasma of atomic number Z emits the same number of photons as an argon plasma ($Z = 18$). In this case the yield would be changed by a factor $\left(\frac{Z}{18}\right)^2$. Therefore the proportionality constant of Eq. (1) would be changed to

$$142 \left(\frac{Z}{18}\right)^2 \quad (3)$$

To complete the Z -scaling of Eq. (1) we must consider the conditions which would result in the same number of photons being emitted from the plasma. Collisional excitation rates at the same relative temperature ($T \sim Z^2$) scale as Z^{-3} . An effectively thin plasma - one where the photons mostly escape even after many scatterings - emits photons proportional to the following factors: first the product of electron and ion density $N_e N_i \sim N^2 Z$; second, the volume, V ; and, third, the collisional excitation rates $W \sim C_1 Z^{-3}$.

$$N_{(\text{photons})} \sim V N_i^2 Z^{-2} C_1 \quad (4)$$

In Eq. (4) C_1 is a constant - independent of Z . Eq. (4) states that scaling the ion density as Z^{+2} would produce the same number of photons from different elements in the same plasma volume. The density function terms of Eq. (1) should therefore be generalized as

$$\left(\frac{\ell}{3}\right) \left(\frac{d}{1.34}\right)^2 \left(\frac{N}{3.7 \times 10^{19} \left(\frac{Z}{18}\right)^2}\right)^{1.9} \left(\frac{t}{15}\right) \quad (5)$$

The power law of 1.9 in Eqs. (1) and (5) accounts approximately for opacity effects on line yield reduction - a perfectly thin plasma would be characterized by an N^2 yield dependence. Combining Eqs. (2), (3), and (5) results in the following analytic expression for yield, valid for any low to medium element of atomic number Z

$$Y(kJ) = 142 \left(\frac{Z}{18}\right)^2 \left(\frac{t}{15}\right) \left(\frac{\ell}{3}\right) \left(\frac{d}{1.34}\right)^2 \left(\frac{N}{3.7 \times 10^{19} \left(\frac{Z}{18}\right)^2}\right)^{1.9} \exp \left(-2.0 \left(\frac{Z}{18}\right)^2 / T\right) \\ \cdot \min \left(1, 2.0 \left(\frac{Z}{18}\right)^2 / T\right) \quad (6)$$

We have applied Eq. (6) to the well-diagnosed shots which have been carried out with neon, aluminum, and titanium [as well as argon which was done last year]. The table summarizes the results.

Table 1
Comparison of Analytic Prediction (Eq. 6) and Measured Yields

<u>Neon</u>					
<u>SHOT</u>	<u>diam.(mm)</u>	<u>N_{ION}</u>	<u>T(keV)⁽¹⁾</u>	<u>Y(kJ,expression)</u>	<u>Y(actual)</u>
1472	1.0	5.0x10 ¹⁹	0.35	46	45
<u>Aluminum</u>					
<u>SHOT</u>	<u>diam.(mm)</u>	<u>N_{ION}</u>	<u>T(keV)⁽²⁾</u>	<u>(Y(kJ,expression)</u>	<u>Y(measured)</u>
174	1.5	2.2x10 ¹⁹	0.69	17.6	14.6
177	1.2	4.0x10 ¹⁹	0.53	22.2	29.2
182	1.2	3.4x10 ¹⁹	0.51	15.1	20.4
183	3.3	0.7x10 ¹⁹	0.79	11.7	6.7
184	5.5	0.13x10 ¹⁹	0.76	1.3	0.6
<u>Titanium</u>					
<u>SHOT</u>	<u>diam.(mm)</u>	<u>N_{ION}</u>	<u>T(keV)⁽³⁾</u>	<u>Y(kJ,expression)</u>	<u>Y(actual)</u>
360	1.5	1x10 ¹⁹	1.33	1.08	0.96
420	1.5	1x10 ¹⁹	1.48	1.35	1.48
422	1.5	1x10 ¹⁹	1.43	1.26	1.22
424	1.5	1x10 ¹⁹	1.53	1.45	1.50
426	1.5	1x10 ¹⁹	1.78	1.91	1.76
409	1.5	1x10 ¹⁹	1.65	1.68	2.02
423	1.5	1x10 ¹⁹	2.00	2.31	2.02
421	1.5	1x10 ¹⁹	2.13	2.52	2.27

(1) Line ratio and continuum temperatures agree.

(2) For shots 174, 177, and 182, T is the average of line ratio and continuum temperatures, for 183 and 184 it is the line ratio temperature (continuum not available).

(3) Average of continuum and line ratio temperatures.

The sequence of titanium shots presented involved changing the peak diode power from 5.2 TW for shot 360 to 7.5 TW for shot 421. As evident, essentially no change was observed in either the size or density of the resultant pinched plasmas. The increase in yield apparently reflects an increase in the temperature with peak diode power, and is tracked quite well by the temperature function of the scaling law, Eq. (6).

The only serious discrepancies present in the comparison of the table are for the large diameter, diffuse Al shots 183 and 184. The presumption of plasma homogeneity is doubtless responsible for most of this difference. The difficulty and inherent inaccuracy in assigning a "radiating diameter" to the entire 3 cm length of plasma could specifically account for most of the differences. The diagnosed line and continuum temperatures also diverged by 20-40% in these two cases. Overall, the predictions for the well-characterized high yield shots agree with the Al measurements within an average of 23% and this points to the overall validity of the general Z-scaled yield expression, Eq. (6).

Influence of Lyman-series fine-structure opacity on the *K*-shell spectrum and level populations of low-to-medium-*Z* plasmas

J. P. Apruzese, J. Davis, D. Duston, and R. W. Clark

*Plasma Radiation Branch, Plasma Physics Division, Naval Research Laboratory,
Code 4720, Washington, D.C. 20375*

(Received 13 July 1983)

As laboratory plasmas of increasing atomic number, temperature, size, and/or density are produced, it becomes likely that the details of the doublet opacity profiles of the Lyman series will influence the *K*-shell level populations and spectrum. Accordingly, we have analyzed these effects for a range of plasma parameters, confined to densities low enough for Stark broadening to be unimportant. An analytic model is developed which predicts line power enhancements and level-population changes for *K*-shell plasmas. This model is based upon photon escape probability and collisional quenching concepts and is valid for plasmas of atomic number ~ 13 –26. Additionally, an extensive set of numerical calculations of line ratios, line profiles, and level populations has been carried out for *K*-shell argon plasmas. Each computation was performed both with detailed fine-structure opacity profiles and with a single-Voigt-profile approximation. The results of these calculations may be scaled for plasmas of atomic number other than 18 using a simple set of rules discussed in the text.

I. INTRODUCTION

Recent years have witnessed dramatic technological advances in laboratory production of optically thick *K*-shell plasmas of low-to-medium-*Z* elements. Consistent with these developments, considerable theoretical effort has been devoted to elucidating the effects of opacity on the spectra and intrinsic properties of such plasmas. Typically—although not exclusively—the hydrogenlike and heliumlike resonance lines of the plasma are quite optically thick but the continua are optically thin in the x-ray region. Thus it is the line opacity which has properly attracted the most concern. As is well known from astrophysical literature, the precise form of the line-opacity profile—which determines the line-photon escape probability—plays a critical role in the formation of the spectrum and determination of the level populations. It is also true that—for quite specific physical reasons—regimes exist where simplified profiles such as pure Doppler may be employed with acceptable accuracy. For instance, Fig. 5(a) of Avrett and Hummer¹ reveals little difference in the steady-state source functions obtained for Voigt and Doppler profiles up to line-center optical depths of ~ 50 with a Voigt broadening parameter of 10^{-2} . One laboratory plasma counterpart of this situation would be a 1.5-mm aluminum plasma of ion density $\sim 10^{19} \text{ cm}^{-3}$ and 600-eV temperature. Detailed calculations² have shown that here, too, a Doppler profile is adequate as a representation for line opacity. We will consider *Z* scaling of all specifically quoted plasma conditions below. At higher densities and/or optical depths a Voigt profile is required to adequately describe photon transport in the line wings. At still higher densities, Stark effects must be considered.^{3–7} In this paper we will delineate the plasma conditions where the doublet-opacity profile due to fine structure in the Lyman lines must similarly be taken into

account. We analyze the underlying physics with both analytic and numerical models, and obtain *Z*-scaled expressions governing the safe use of simpler opacity approximations. In Sec. II an analytic model is developed which serves two basic functions. First, it provides a physical basis for comprehending the trends which appear in the numerical results. Second, approximate but useful *Z*-scaled formulas expressing some of the results are obtained. In Sec. III specific numerical results for an argon plasma ($Z=18$) are presented along with a prescription for scaling them to plasmas of different atomic numbers.

II. ANALYTIC MODEL

A. Assumptions and restrictions

Both the analytic and numerical results contained in this paper are restricted to plasma regions where Stark broadening has only a small effect on photon transport and can be neglected. The calculations encompass at most a few hundred optical depths in Ly α ; hence, for only the first three lines of the Lyman series will photon transport in the far line wings be significant. Stark profiles follow approximately an inverse 2.0–2.5 power law³ as a function of frequency separation from line center; for Voigt profiles, the asymptotic limit is an inverse power of 2.0. Therefore, if the Stark width is smaller than the Doppler width, the Stark wings will generally be considerably smaller than the Lorentz wings. This criterion is presently adopted in determining the maximum density to which our calculations can be reasonably extended. We obtain a specific density for argon from the tabulated Stark profiles of Kepple and Whitney,⁸ and scale the criterion analytically for different atomic numbers.

In examining the Stark profiles for Ly α , Ly β , and Ly γ , it is clear that the upper density limit is set by the

broad, double-peaked profile of Ly β . For argon, an electron density of $\sim 2 \times 10^{22} \text{ cm}^{-3}$ is required for the Stark width to equal the Doppler width at temperatures of maximum Ar XVIII abundance. Accordingly, the analytic theory presented below is valid only up to this density for argon and the numerical calculations described in the next section have not been carried to higher densities.

This criterion for the negligibility of Stark effects is readily Z-scalable. Griem, Blaha, and Kepple³ found that the Stark widths expressed in Å for analogous lines from different elements scale approximately as $Z^{-5} N_e^{2/3}$ near maximum ionic abundance temperature. The Doppler width, also expressed in Å, scales as $Z^{-1.5}$ at maximum abundance temperature. Therefore, the Stark width for the first three Lyman lines will be less than the Doppler width if

$$\left| \frac{18}{Z} \right|^5 \left| \frac{N_e}{2 \times 10^{22}} \right|^{2/3} \leq \left| \frac{18}{Z} \right|^{1.5} \quad (1)$$

or

$$N_e \leq 5.1 \times 10^{15} Z^{5.25}. \quad (2)$$

Consequently, the present results are not valid at electron densities higher than those indicated by Eq. (2).

The relative populations of the $2p_{3/2}$ and $2p_{1/2}$ fine-structure levels, which are likely to prevail under different plasma conditions, have been a subject of investigation and debate for quite a few years.⁸⁻¹⁴ Irons¹³ has summarized the status of this work. Briefly, at the high- and low-density limits, ϵ , the ratio of the $2p_{1/2}$ to $2p_{3/2}$ sub-level populations, will equal 0.5, the statistical weight ratio of the states. Rapid collisional mixing ensures statistical equilibrium at high densities, and in the low-density coronal limit there is little pumping of the $2p$ states from $2s$; therefore, statistical populations prevail because only this process can cause departures from $\epsilon = 0.5$. In the intermediate density regime, ϵ may reach values as high as 0.7–0.8, although the relative effects of electron-ion and ion-ion collisions are not yet precisely determined¹⁰ and render this conclusion still somewhat uncertain. As pointed out by Sampson¹² and Irons,^{13,14} substantial optical depth will reduce any tendency for a departure from statistical equilibrium. In view of the remaining uncertainties as well as the fact that the plasmas we analyze here are generally optically thick, we have assumed statistical population of the $j = \frac{1}{2}$ and $j = \frac{3}{2}$ sublevels ($\epsilon = 0.5$) for all the plasmas considered here, for each hydrogenlike level. We also assume that the ion thermal velocities are sufficiently greater than the plasma differential motion to enable the plasma to be treated as stationary. Irons^{13,14} has explored some of the consequences of substantial plasma differential motion for Ly- α opacity.

B. Analysis of opacity effects

The doublet splitting of the Lyman series is important as an opacity determinant when the separation of the components is comparable to the Doppler half-width ($\Delta\nu_D$) of the line. For specificity, the $\Delta\nu_D$ referred to here is the half-width of the Doppler line profile at e^{-1} of the central maximum. As pointed out by Irons,¹³ the ratio

of the fine-structure splitting to the Doppler half-width varies as $Z^{1.5}$ since the characteristic temperature for hydrogenlike-ion predominance varies as Z^2 . Specifically, for Ly α ,

$$(\Delta\nu)_f / (\Delta\nu)_D \approx 5.3 \left| \frac{Z}{18} \right|^{1.5}. \quad (3)$$

For Ly β , the splitting relative to the Doppler width is about one-fourth the above value; for Ly γ , about one-tenth. Therefore, fine-structure opacity effects will have by far their greatest impact on Ly α , both because of its greater optical depth and because the splitting is greater relative to the Doppler line width. Our semiquantitative analytic model consequently focuses on Ly α .

Consider the $n = 2$ hydrogenlike level, with the sublevels assumed statistically populated. For the moderate density plasmas considered here, this level is populated primarily by collisional excitation from the hydrogenlike ground state and by radiative excitation due to scattered Ly α photons. Depopulation occurs by a variety of processes, including spontaneous decay, collisional excitation and de-excitation, and (primarily collisional) ionization. We will follow the standard approximate procedure in accounting for radiative excitation by diluting the spontaneous decay rate A_{21} by the spatially averaged photon-escape probability P_e . This counts only those decays not resulting in re-excitation of the $n = 2$ level. Letting C_{12} stand for the collisional excitation rate from $n = 1$ in $\text{cm}^3 \text{ sec}^{-1}$, D_2 represents the sum of all collisional processes depopulating the $n = 2$ level; also in $\text{cm}^3 \text{ sec}^{-1}$, a qualitatively correct equation for the steady-state population of the $n = 2$ level is

$$N_1 C_{12} N_e = N_2 (A_{21} P_e + D_2 N_e). \quad (4)$$

In Eq. (4), N_1 and N_2 are the $n = 1$ and 2 level population densities (cm^{-3}), N_e is the electron density (cm^{-3}), and the other symbols are defined above. It is useful to define a quenching probability P_Q —the probability that the $n = 2$ level is collisionally depopulated during a Ly- α scattering

$$P_Q = D_2 N_e / (A_{21} + D_2 N_e). \quad (5)$$

Combining Eqs. (4) and (5) leads to the following expression for the $n = 2$ population density:

$$N_2 = \frac{N_1 C_{12}}{D_2} \left[1 / P_e \left| \frac{1 - P_Q}{P_Q} \right| + 1 \right]. \quad (6)$$

The significance of Eq. (6) becomes apparent when considering P_e . The escape probability obtained will depend on whether the single-Voigt-profile approximation or the true fine-structure profile is used in the calculation. Letting P_e now stand for the escape probability, which would be obtained from the spurious single-Voigt-profile approximation, and P_{ef} refer to the true fine-structure-escape probability, the ratio of population densities obtained with the correct opacity to that obtained with the single-profile opacity is

$$\frac{N_2(\text{with fine structure})}{N_2(\text{single Voigt})} = \frac{P_e(1 - P_Q) + P_Q}{P_{ef}(1 - P_Q) + P_Q}. \quad (7)$$

Equation (7) is obtainable from Eq. (6) with the (excellent) assumption that N_1 is not affected by fine-structure opacity. Note the limits implicit in Eq. (7). At very high densities, when $P_Q \rightarrow 1$, there is no difference in populations. Collisional processes control the level population. Also, when $P_e(1-P_Q)$ and $P_{ef}(1-P_Q)$ are both much smaller than P_Q , fine structure again has no effect on N_2 . This corresponds to the effectively thick case, where most photons do not escape, even after many scatterings. The number of radiative excitations, while possibly large, is determined by collisional quenching, not by the detailed behavior of P_e or P_{ef} . However, when $P_Q \rightarrow 0$ the computed populations of $n=2$ are inversely proportional to the ratio of escape probabilities. Radiative excitation dominates the level if P_e (or P_{ef}) is substantially smaller than unity. For fine-structure opacity to be negligible (defined as having less than a 10% effect on population of $n=2$) we require

$$P_e(1-P_Q) + P_Q > 0.9P_{ef}(1-P_Q) + 0.9P_Q. \quad (8)$$

In general, P_{ef} will exceed P_e . For Ly α , a single line of optical depth τ_0 is in effect replaced by two separate lines of optical depths $\frac{1}{2}\tau_0$ and $\frac{1}{2}\tau_0$ for $2p_{3/2}$ and $2p_{1/2}$, respectively. The escape probability at large optical depth for a Voigt profile is proportional to $\tau^{-1/2}$; hence, if there is no overlap of the doublet wings

$$\frac{P_{ef}}{P_e} = \left[\frac{1}{3} \left(\frac{\tau_0}{3} \right)^{-1/2} + \frac{2}{3} \left(\frac{2\tau_0}{3} \right)^{-1/2} \right] / (\tau_0)^{-1/2} \approx 1.4. \quad (9)$$

As discussed by Irons,¹⁴ the assumption of no wing overlap fails for $\tau_0 \geq 10^2$; this failure will arise at lower τ_0 for small Z and higher τ_0 for large Z , according to Eq. (3) for the doublet spacing. However, since we seek a criterion for the onset of fine-structure-opacity effects, the ratio of Eq. (9) will be presently assumed. More exact results are given below in the section on numerical modeling. Combining Eqs. (8) and (9) yields the following criterion for the negligibility of fine-structure-opacity effects on population densities:

$$0.38 \left[\frac{P_Q}{1-P_Q} \right] > P_e, \quad (10)$$

or employing Eq. (5)

$$0.38 \left[\frac{D_2 N_e}{A_{21}} \right] > P_e. \quad (11)$$

To cast Eq. (11) into a more useful form, note that $A_{21} \approx 5 \times 10^{13} (Z/18)^4 \text{ sec}^{-1}$. Also, depopulation of the $n=2$ level is temperature, density, and Z dependent. Following Refs. 9–11, we will refer to the temperature in units of $Z^2 \text{ Ry} = 13.6 Z^2 \text{ eV}$. For temperatures of $(0.18-0.57) Z^2 \text{ Ry}$ (0.8 to 2.5 keV for argon) the depopulation of $n=2$, summed over the levels, has been calculated from the Coulomb-Born approximation¹⁶ and is found to vary less than 20% from its value at $0.3 Z^2 \text{ Ry}$, where

$$D_2 = 2 \times 10^{-10} \left[\frac{18}{Z} \right]^3 \quad (12)$$

in units of $\text{cm}^3 \text{ sec}^{-1}$. The temperature range $(0.18-0.57) Z^2 \text{ Ry}$ covers a large range of plasmas where hydrogenlike species are significantly present. Combining Eqs. (11) and (12) yields our final, Z -dependent criterion for less than 10% level population change due to fine-structure opacity

$$9.3 \times 10^{-16} Z^{-7} N_e > P_e. \quad (13)$$

If the electron density is sufficiently high to render the inequality of Eq. (13) valid, fine-structure opacity—as compared to the single-Voigt-profile approximation—will affect the level populations by less than 10%. We again stress that Eq. (13) is to be applied to optically thick plasmas only—when the plasma is optically thin the fine-structure profiles cannot affect populations. The Voigt-profile escape probability P_e has been given in approximate analytic form by Athay.¹⁵

The effect on line emission of the doublet profile is perhaps of even more interest and importance than the change in population densities. Even though the populations may not be affected, the different effective escape probability can surely influence the Ly- α integrated intensity. The ratio of computed emission with fine-structure opacity to that obtained from a single Voigt profile is

$$\frac{I_f}{I_0} = \frac{N_2(\text{fine}) A_{21} P_{ef}}{N_2(\text{single Voigt}) A_{21} P_e}, \quad (14)$$

or, using Eq. (7),

$$\frac{I_f}{I_0} = \frac{P_{ef}}{P_e} \left[P_e + \frac{P_Q}{1-P_Q} \right] / \left[P_{ef} + \frac{P_Q}{1-P_Q} \right]. \quad (15)$$

The quantity $P_Q/(1-P_Q)$ is obtainable as above for the temperature range $(0.18-0.57) Z^2 \text{ Ry}$, from Eqs. (5) and (12), and the expression for A_{21}

$$\left[\frac{P_Q}{1-P_Q} \right] \approx 2.45 \times 10^{-15} N_e Z^{-7}. \quad (16)$$

Therefore,

$$\frac{I_f}{I_0} = \frac{P_{ef}}{P_e} \frac{P_e + 2.45 \times 10^{-15} N_e Z^{-7}}{P_{ef} + 2.45 \times 10^{-15} N_e Z^{-7}}. \quad (17)$$

Equation (17) is usable if P_e and P_{ef} can be calculated or estimated. If, as before, we assume $P_{ef} = 1.4 P_e$, an approximate criterion for 10% enhancement of emission due to fine structure is obtainable,

$$5.2 \times 10^{-15} N_e Z^{-7} > P_e. \quad (18)$$

The physical content of Eq. (18) is that, in an optically thick plasma with an electron density sufficiently high to validate the inequality, fine-structure opacity will result in a Ly- α intensity at least 10% higher than would be obtained from the single Voigt approximation.

We have demonstrated that the interplay of optical depth (as expressed by P_e) and the collisional quenching rate (as expressed by N_e), rather than either factor alone,

determines the importance of doublet-opacity effects on population densities and spectral emission. Several simple expressions obtained above express this interplay semi-quantitatively and convincingly demonstrate the trends to be anticipated. We now turn to specific numerical results for further illumination of the question.

III. NUMERICAL MODEL

A. Model description

In order to validate and clarify the analytic approximations presented above, as well as provide more specific spectral diagnostics, we have performed an extensive series of numerical calculations centered on one element (argon). The calculations consist of a set of simultaneous solutions of the coupled atomic-rate and radiative-transfer equations for argon plasma cylinders where the varied parameters are temperature, density, and radius r , presumed much smaller than the length. These solutions have typically been carried out with both the more realistic doublet opacity and an assumed single Voigt profile for each parameter set.

The atomic model consists of 38 levels ranging from neutral Ar I to the bare nucleus (Ar XIX). Since our focus is on K -shell radiation, only ground states are carried through Be-like argon (Ar XV). For Li-like Ar XVI, the $1s^2s$, $1s^2p$, $1s^23s$, $1s^23p$, $1s^23d$, and $1s^2$, $n=4$ (composite) levels are modeled. The Ar XVII manifold includes $1s^21S$, $1s2s^3S$, $1s2p^3P$, $1s2s^1S$, $1s2p^1P$, the $n=3$ triplets and singlets, and $n=4-7$ composite levels. For Ar XVIII, $n=1-5$ are included. The various levels are connected through electron collisional excitation and deexcitation, collisional ionization and radiative recombination, three-body recombination, and, where appropriate, dielectronic recombination. Photoionization and photoexcitation are accounted for by solving the radiative transfer. All the modeled ionization edges are included as part of the radiative-transfer model. Additionally, all the optically thick resonance lines inherent in the level structure described above are also transported, along with the 2-3 line of Ar XVIII and the $1s2p^1P-1s3d^1D$ line of Ar XVII. While some of the higher levels have been omitted because of storage and efficiency considerations, the model provides a substantially complete description of the processes which form the dominant spectral lines of K -shell argon. A discussion of the atomic rate calculations is contained in Ref. 17. In all results presented below, the plasma is assumed to be in collisional-radiative equilibrium (CRE); namely, that each level-population density is in a steady state consistent with the atomic rates and photon fluxes produced by the other level populations.

Some improvements have been effected in our technique for carrying out the simultaneous, steady-state solution of the radiative-transfer and rate equations.^{2,4,17-22} Reference 21 describes a multicell-coupling technique for radiative transfer in spherical and cylindrical geometries, based on frequency-integrated line escape probabilities. This method produces nearly exact solutions while employing only one ray angle and the computational equivalent of just one frequency per line. To account for doublet opaci-

ty, where escape probabilities have yet to be tabulated or fitted analytically, we have adopted a hybrid of the method of Ref. 21 and more conventional multifrequency approaches. The single-angle feature of Ref. 21 is retained but each line is divided into 17-43 frequency groups—depending on the line shape and optical depth. The coupling constants are defined in terms of individual frequencies (where the escape probability at each frequency is purely exponential) rather than individual lines. This also allows inclusion of continuum optical depths and line and continuum cross-pumping. Given the population densities a set of cell-to-cell photon coupling constants at each of more than 350 frequencies is thus obtainable.

The iteration technique by which self-consistency between the radiative-transfer and steady-state rate equations is obtained has also been significantly improved. The most straightforward and obvious procedure, using the radiation field from the previous iteration to calculate populations which then enables the radiation field to be recomputed until consistency is achieved, is known as Λ iteration. This technique is a very poor choice for low-density, high-optical-depth astrophysical problems²³ since the number of iterations required is approximately equal to the mean number of photon scatterings, which can be very large under such circumstances. However, the situation is not nearly so difficult for laboratory plasmas where the optical depths are smaller and the quenching probabilities larger than those which prevail in astrophysical situations, resulting in far fewer scatterings. We employ the mathematical equivalent of Rybicki's core-saturation method²⁴ and thereby render the Λ -iteration technique quite serviceable for laboratory plasma calculations. As noted by Rybicki,²⁴ the conceptual and computational simplicity of the technique is a very desirable feature, especially for complex multilevel problems.

To demonstrate our application of the core-saturation method for Λ iteration, we consider one line characterized by a profile-averaged photon escape probability from the plasma P_e and quenching probability P_Q . Let $N_u^{(i)}$ represent the upper level density obtained on the i th iteration and A the spontaneous decay probability. The photoexcitation rate for the i th iteration is therefore $N_u^{(i)}A(1-P_e)$. If C_u and D_u are the collisional creation and depopulation rates, respectively, for N_u , $N_u^{(i+1)}$ is obtained from the equation balancing gains and losses in the level

$$N_u^{(i+1)}(A + D_u) = C_u + N_u^{(i)}A(1 - P_e), \quad (19)$$

or

$$N_u^{(i+1)} = N_u^{(1)} + N_u^{(i)}(1 - P_e)(1 - P_Q), \quad (20)$$

where $P_Q = D_u / (A + D_u)$ as before, and the upper level population for an optically thin plasma is given by the first iterative solution

$$N_u^{(1)} = \left[\frac{C_u}{A + D_u} \right]. \quad (21)$$

Equation (20) yields a recursive sum for the n th iteration's solution

$$N_u^{(n)} = N_u^{(1)} \sum_{i=0}^{n-1} [(1-P_e)(1-P_Q)]^i. \quad (22)$$

The slow convergence of the sum of Eq. (22) when $P_e, P_Q \ll 1$ precisely expresses the difficulty of Λ iteration. Note, however, that the sum is analytically evaluable to give

$$N_u^{(\infty)} = N_u^{(1)} \left(\frac{1}{1 - (1-P_e)(1-P_Q)} \right) \quad (23)$$

and that this is exactly what is obtained for N_u on the first iteration if, in Eq. (19) A is replaced by AP_e instead of calculating excitations as $A(1-P_e)$. This is the essence of Rybicki's technique²⁴ of eliminating the readily absorbed line core photons. In practice, we apply the method by calculating, cell by cell, the escape probability from the plasma for each line by integrating over the absorption profile—including the continuum. The spontaneous emission coefficients are then diluted by this factor on the first iteration, which generally results in an excellent approximation to the final solution, especially near the plasma center. On subsequent iterations, the spontaneous emission coefficients are diluted in each cell by the escape probability from that cell and excitations are computed explicitly only for the line wing photons arriving from other cells. This completely general procedure usually converges within 20 iterations even for several hundred Ly- α optical depths. Convergence has been verified by starting with entirely different initial iterative solutions, and by quadrupling the number of iterations, both of which yield the same final level populations.

B. Z scaling of numerical results

In order that the results given below, specifically obtained for argon, may be readily applied to other low-to-medium- Z elements, we present the methodology for Z scaling in this section. Given a K -shell argon plasma of radius R_0 , ion density N_i , and temperature T_e , the results may clearly be applied to a plasma of atomic number Z at a temperature of $T_e(Z/18)^2$. However, scaling the density and size is not quite so straightforward. To maintain the analogous level populations and spectrum, it is evident from the discussion in Sec. II that both the quenching probabilities and optical depths must remain the same. The quenching probability is determined by the ratio of collision rates—which scale as Z^{-3} —to spontaneous decay rates—which scale as Z^4 . Since the quenching probability consequently scales as Z^{-7} , the electron density must scale as Z^7 to offset this. Therefore, the ion density must increase as Z^6 to maintain the same ratio of radiative to collisional rates as would prevail in an argon plasma. Finally, to maintain the same line optical depth τ_0 , note that it is proportional to $R_0 N_i \lambda (M/T_i)^{1/2}$ where λ is the wavelength, M the ion mass, and T_i the ion temperature. Since $N_i \sim Z^6$, $\lambda \sim Z^{-2}$, $M \sim Z$, and $T_i \sim Z^2$, $\tau_0 \sim R_0 Z^{3.5}$. Therefore, the size must scale as $Z^{-3.5}$ to maintain the optical depth. In summary, a K -shell plasma of atomic number Z , radius $R_0(18/Z)^{3.5}$, ion density $N_i(Z/18)^6$, and temperature $T_e(Z/18)^2$ will produce the same spectrum as an argon plasma of radius R_0 , ion den-

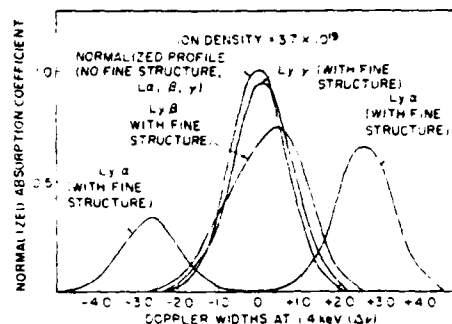


FIG. 1. Normalized fine-structure profiles of the absorption coefficients of Ar XVIII Ly α , β , and γ are compared to the single Voigt profile which would characterize the opacity in the absence of fine-structure splitting.

sity N_i , and electron temperature T_e . The "same" spectrum is defined as the same relative intensities of the lines. Absolute intensities will differ due to the differing line photon energies and total numbers of emitting ions. We recommend Z scaling only for $13 \leq Z \leq 26$ from the $Z=18$ results presented below, since the $Z^{1.5}$ scaling of fine-structure splitting [Eq. (3)] will spoil the applicability of the scaling far from $Z=18$.

C. Numerical results

In Fig. 1 the doublet absorption profiles for Ar XVIII Ly α , Ly β , and Ly γ are shown along with the single Voigt profile which would characterize the line opacity in the absence of fine structure. The profiles are normalized for case of comparison. Plasma conditions of ion temperature 1.4 keV and ion density $3.7 \times 10^{19} \text{ cm}^{-3}$ are assumed. Note that the Ly- α profile is split into two distinct features since the doublet components are ~ 5 Doppler widths apart. However, both Ly β and Ly γ appear quasi-Gaussian, with a skewing of the profile toward the stronger of the fine-structure components. For Ly γ , the change from the single Voigt profile is quite small.

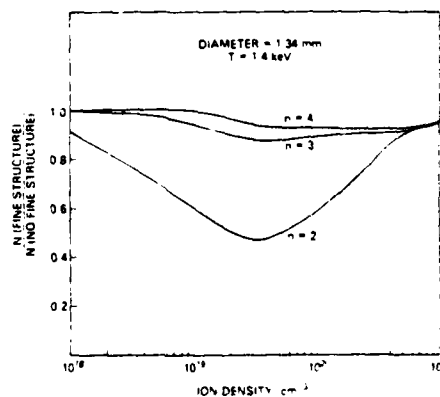


FIG. 2. Ratio of the $n=2, 3$, and 4 Ar XVIII populations obtained with the correct fine-structure profiles to those obtained using a single Voigt profile are plotted against ion density for the indicated cylindrical plasma temperature and diameter.

Therefore, the following results will concentrate on Ly- α and Ly- β power outputs and line ratios which could reflect those outputs as influenced by fine-structure opacity.

In Fig. 2 the ratio of populations calculated with realistic doublet opacities to those which would prevail in the absence of fine structure is plotted against density, for an argon plasma temperature of 1.4 keV and a diameter of 1.34 mm. The changes in $n=3$ and 4 are 15% or less, whereas, for an ion density of $\sim 3 \times 10^{19} \text{ cm}^{-3}$, the $n=2$ population is reduced by a factor of 2. For all three levels, the population ratio approaches unity at both low and high densities, consistent with Eq. (7). For the $1s_{1/2}-2p_{3/2}$ component, the line-center optical depths are 0.14, 2, 47, and 420 at ion densities of 10^{18} , 10^{19} , 10^{20} , and 10^{21} cm^{-3} , respectively. The corresponding optical depth of a single Voigt profile, τ_0 , would be 50% greater. Since $N_e \approx 18N_i$, $\tau_0 \approx 3.5 \times 10^{-20} N_e$ for ion densities between 10^{20} and 10^{21} cm^{-3} . The approximate escape probability for a Voigt profile¹⁵ is given as a function of the damping parameter a and optical depth τ_0 for $\tau_0 \gg 1$:

$$P_e \approx 0.85 \left(\frac{a}{\tau_0} \right)^{1/2} \quad (24)$$

The damping parameter a for a resonance line is

$$a = \frac{\Gamma}{4\pi\Delta\nu_D} \quad (25)$$

where the upper-state inverse lifetime Γ for Ly α is mostly determined by radiative decay in this density range. The Doppler width $\Delta\nu_D$ at 1.4 keV is $2.2 \times 10^{14} \text{ Hz}$. Including the collisional contribution, $a \approx 2.5 \times 10^{-2}$ for these densities, and Eqs. (24) and (13) may be combined to obtain the electron density at which a 10% departure of $n=2$ population due to fine-structure opacity would be expected according to the analytic theory

$$9.3 \times 10^{-16} (18)^{-7} N_e > 0.85 \left(\frac{2.5 \times 10^{-2}}{3.5 \times 10^{-20} N_e} \right)^{1/2} \quad (26)$$

which yields an electron density of $6.1 \times 10^{21} \text{ cm}^{-3}$, equivalent to an ion density of $3.4 \times 10^{20} \text{ cm}^{-3}$ which is in excellent agreement, considering the approximations, with the numerically calculated value of 4.5×10^{20} (Fig. 2).

The most experimentally detectable consequence of fine structure is certainly spectroscopic effects. The analytic results presented above also contain [Eq. (18)] an electron-density criterion for 10% enhancement of Ly α . In Fig. 3 we present two line ratios which are both temperature and density sensitive: $\text{He } 1s^2-1s4p^1P/\text{Ly } \beta$ and $\text{He } 1s^2-1s3p^1P/\text{Ly } \alpha$, as a function of density, with and without the correct doublet opacity. The ratios decrease substantially with density even with fixed temperature (1.4 keV) and plasma diameter (1.34 mm) since higher collision rates and optical depths increase the excitation and ionization state of the plasma. However, at the highest densities the Ar XVII to Ar XVIII line ratios level off and then increase. This is primarily due to the increased opacity of the Lyman lines coupled with the decreased opacity of the heliumlike lines as the average charge state of the plasma increases with density. The double valuing of line ratios

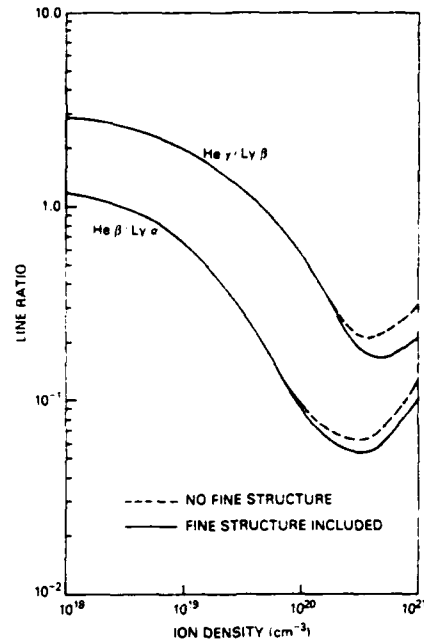


FIG. 3. Line ratios $\text{Ar XVII } 1s^2-1s3p^1P/\text{Ly } \alpha$ and $\text{Ar XVII } 1s^2-1s4p^1P/\text{Ly } \beta$ are plotted against ion density for a plasma diameter of 1.34 mm and temperature 1.4 keV. Where fine-structure opacity results in significant differences, it is indicated.

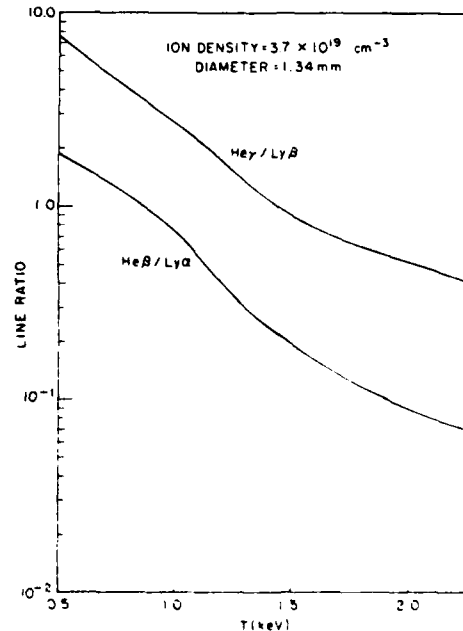


FIG. 4. Same line ratios of Fig. 3 are plotted against temperature for the same size cylindrical argon plasma (1.34 mm) at an ion density of $3.7 \times 10^{19} \text{ cm}^{-3}$, where the presence of fine structure makes no difference.

due to opacity effects has been noted elsewhere.¹⁹ At ion densities of $\sim 10^{20}$ and higher, the dichotomy between fine-structure and single-profile calculations is noticeable; it reflects the higher power outputs of both Ly α and Ly β due to the greater effective escape probabilities of the doublet profiles. For Ly α , these results provide another point of comparison with the theory of Sec. II. According to Eq. (18), the Ly- α line intensity should be enhanced by 10% when

$$5.2 \times 10^{-15} N_e Z^{-7} > P_e. \quad (18)$$

Equation (24), plus the fact that $\tau_0 \approx 3.5 \times 10^{-20} N_e$ allows Eq. (18) to be solved for N_e ; the result predicts a 10% power enhancement at $N_e \approx N_e / 18 = 1.1 \times 10^{20} \text{ cm}^{-3}$, in excellent agreement with the numerically calculated value of $1.3 \times 10^{20} \text{ cm}^{-3}$ (Fig. 3).

Figures 4 and 5 present this same ratio as a function of temperature, again for a plasma of fixed diameter 1.34 mm. In Fig. 4 the ion density is $3.7 \times 10^{19} \text{ cm}^{-3}$. At these relatively modest optical depths (~ 10 for Ly α) the ratios are single valued and a very good temperature indicator. Also, fine structure does not affect the power output at this density; therefore, only one curve appears for each line ratio. This may be contrasted with Fig. 5 where the same information is presented at the considerably higher ion density of 10^{21} cm^{-3} . Fine-structure opacity noticeably depresses the line ratios for the entire temperature range considered. Also, the much larger optical depths virtually eliminate the temperature sensitivity of the ratios above 1.0 keV; as the population of Ar XVIII increases with temperature, so does the opacity, which considerably reduces the tendency of the Lyman line to increase in intensity. At an ion density of $3.7 \times 10^{19} \text{ cm}^{-3}$, the Lyman photons generally escape after a few scatterings; at 10^{21} cm^{-3} , they are mostly collisionally quenched.

The fact that the enhancement of Ly β is comparable to that of Ly α may seem puzzling in light of the fact that the Ly- β profile is not so drastically affected by fine structure (Fig. 1). However, the Lorentz wings of the profile are substantially enhanced by the increase in damping parameter (i.e., reduction in level lifetime) when collisions transferring population among fine-structure levels are considered. At such high opacities, substantial numbers of photons can escape only in these far wings—resulting in the Ly- β power increase. For Ly α , as noted above, the upper level lifetime is still mostly determined by its very high radiative decay rate, even when collisions among fine-structure levels are considered.

Finally, in Fig. 6 we present the evolution of the emitted Ly- α profile as a function of density for a temperature of 1.4 keV and a plasma diameter of 1.34 mm. At $N_e = 10^{18} \text{ cm}^{-3}$, the $2p_{3/2}$ component is twice the strength of the $2p_{1/2}$ since the lines are optically thin at this density. At $6 \times 10^{18} \text{ cm}^{-3}$, $\tau_0 \approx 1$ and the $2p_{3/2}$ component begins to saturate to the value of the source function—allowing the $2p_{1/2}$ to begin to approach its intensity. At $3.7 \times 10^{19} \text{ cm}^{-3}$, full saturation has occurred—the components are of equal intensity and a small self-reversed core is seen in each. The profiles at ion densities of 10^{20} and $3 \times 10^{20} \text{ cm}^{-3}$ are qualitatively similar to that at

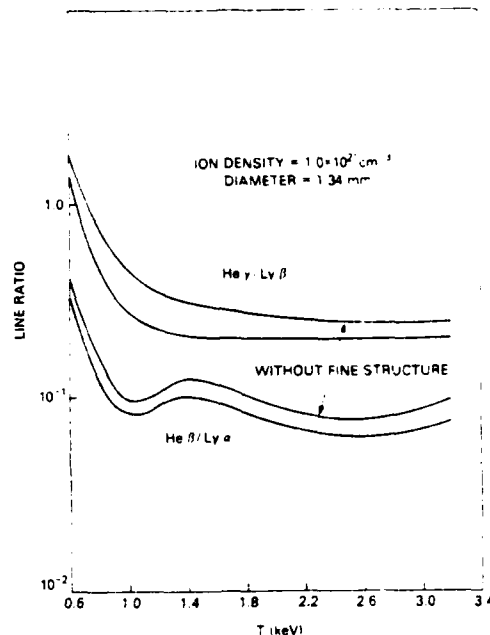


FIG. 5. Same as Fig. 4, except the density is 10^{21} ions per cm^{-3} . At this density the result depends upon the details of the fine-structure profile and such is indicated.

$3.7 \times 10^{19} \text{ cm}^{-3}$ except that the higher optical depths produce deeper self-reversed cores. At ion densities of $7.5 \times 10^{20} \text{ cm}^{-3}$ and 10^{21} cm^{-3} , the profiles have a peculiar three-pronged appearance. The three peaks appear where the profile optical depth is approximately unity—one peak on each of the far wings of the components, with another emission peak occurring at the absorption minimum between the two components.

Because of this density sensitivity, the Ly- α profile is potentially an excellent density diagnostic. Since the pro-

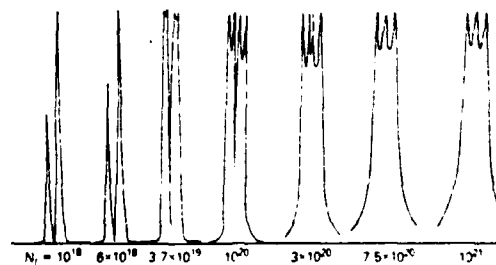


FIG. 6. Evolution of the emitted Ly- α profile is presented as a function of density for an argon plasma of 1.4 keV and diameter 1.34 mm. The splitting of the two components visible at the lowest density is 5.4 mÅ and this horizontal scale is maintained throughout. The absolute intensities have been normalized for ease of comparison.

files depend on optical depth as well as density, the size of the plasma must be ascertained to fully exploit this technique. Experimental methods such as x-ray pinhole photography would be quite valuable for this purpose. Also, spectral resolution of $\sim 1\text{--}2\text{ m}\text{\AA}$ will be required, independently of Z .

ACKNOWLEDGMENTS

The authors would like to express their appreciation to Dr. P. C. Kepple and Dr. H. R. Griem for several valuable discussions. This work was supported by the U. S. Defense Nuclear Agency.

- ¹E. H. Avrett and D. G. Hummer, *Mon. Not. R. Astron. Soc.* **130**, 295 (1965).
- ²J. P. Apruzese, J. Davis, D. Duston, and K. G. Whitney, *J. Quant. Spectrosc. Radiat. Transfer* **23**, 479 (1980).
- ³H. R. Griem, M. Blaha, and P. C. Kepple, *Phys. Rev. A* **19**, 2421 (1979).
- ⁴J. P. Apruzese, P. C. Kepple, K. G. Whitney, J. Davis, and D. Duston, *Phys. Rev. A* **24**, 1001 (1981).
- ⁵P. C. Kepple and K. G. Whitney, Naval Research Laboratory (NRL) Memorandum Report No. 4565, 1981 (unpublished).
- ⁶A. Hauer, K. G. Whitney, P. C. Kepple, and J. Davis, *Phys. Rev. A* **28**, 963 (1983).
- ⁷R. W. Lee, *J. Quant. Spectrosc. Radiat. Transfer* **27**, 87 (1982).
- ⁸R. J. Hutcheon and R. W. P. McWhirter, *J. Phys. B* **6**, 2668 (1973).
- ⁹I. L. Beigman, V. A. Boiko, S. A. Pikuz, and A. Ya. Faenov, *Zh. Eksp. Teor. Fiz.* **71**, 975 (1976) [*Sov. Phys.—JETP* **44**, 511 (1976)].
- ¹⁰A. V. Vinogradov, I. Yu. Skobelev, and E. A. Yukov, *Fiz. Plazmy* **3**, 686 (1977) [*Sov. J. Plasma Phys.* **3**, 389 (1977)].
- ¹¹V. A. Boiko, A. V. Vinogradov, S. A. Pikuz, I. Yu. Skobelev, A. Ya. Faenov, and E. A. Yukov, *Fiz. Plazmy* **4**, 97 (1978) [*Sov. J. Plasma Phys.* **4**, 54 (1978)].
- ¹²D. H. Sampson, *J. Phys. B* **10**, 749 (1977).
- ¹³F. E. Irons, *Aust. J. Phys.* **33**, 283 (1980).
- ¹⁴F. E. Irons, *J. Quant. Spectrosc. Radiat. Transfer* **24**, 119 (1980).
- ¹⁵R. G. Athay, *Radiation Transport in Spectral Lines* (Reidel, Dordrecht, 1974), pp. 22–24.
- ¹⁶L. A. Vainshtein and I. I. Sobel'man, *Lebedev Report No. 66*, 1967 (unpublished); I. I. Sobel'man, *Introduction to the Theory of Atomic Spectra* (Pergamon, New York, 1972).
- ¹⁷D. Duston and J. Davis, *J. Quant. Spectrosc. Radiat. Transfer* **27**, 267 (1982).
- ¹⁸J. P. Apruzese, J. Davis, and K. G. Whitney, *J. Appl. Phys.* **48**, 667 (1977).
- ¹⁹D. Duston and J. Davis, *Phys. Rev. A* **21**, 932 (1980).
- ²⁰K. G. Whitney, J. Davis, and J. P. Apruzese, *Phys. Rev. A* **22**, 2196 (1980).
- ²¹J. P. Apruzese, *J. Quant. Spectrosc. Radiat. Transfer* **25**, 419 (1981).
- ²²D. Duston, J. Davis, and P. C. Kepple, *Phys. Rev. A* **24**, 1505 (1981).
- ²³D. Mihalas, *Stellar Atmospheres* (Freeman, San Francisco, 1970), pp. 152–155.
- ²⁴G. B. Rybicki, Conference on Line Formation in the Presence of Magnetic Fields, National Center for Atmospheric Research Report, Boulder, 1971 (unpublished).

B. Ionization Dynamics and Diagnostics

I. INTRODUCTION

In response to the new experiments being planned on the Gamble II machine during FY84, several new atomic models have been constructed and implemented in the ionization/radiation models. With the acquisition of the Hartree-Slater atomic structure code of Cowan, the compilation of energy levels and radiative decay rates has been vastly improved, both in the increased comprehensiveness of the data as well as the enhanced accuracy. This improvement is directly reflected in the predictive capability of the radiation models.

II. MODELS

Two new K-shell models were completed this year, for silicon and titanium. Both models contain the sufficient level structure needed to accurately diagnose x-ray spectra from dense plasmas of these materials. In particular, this includes up to n-values (principal quantum number) of 5 in the hydrogenlike, heliumlike, and lithiumlike ions. The silicon models expected to be employed in imploding glass wire experiments on the pulse power generator at NRL. Conceivably, glass could be incorporated as a core element or a mixture with aluminum in order to test the cooperative photon pumping effects between the two materials. An example of a silicon K-shell spectrum is shown in Fig. 1.

The titanium K-shell model was likewise constructed to diagnose imploding wire arrays of this material. During previous experiments on the BJV generator, titanium received serious consideration as a PRS load material. With the upgrades on existing machines, it is possible that titanium wires will be re-examined as a viable radiation source. A typical titanium K-shell spectrum is shown in Fig. 2.

It has often been conjectured that it may be far easier to use the L-shell x-ray emission from a high-Z material rather than the K-shell x-rays from a lower-Z material (e.g., neon, aluminum, argon) to obtain radiation

emission of the right color for the DNA-PRS goals. To this end, experimentalists at PI have been working with a krypton gas puff during recent months. Krypton has also been selected as the primary load material to test the new gas puff capabilities presently being installed on the NRL Gamble II generator. In order to provide theoretical support for these programs, an L-shell model for krypton has been constructed. This model represents a Herculean effort in both data compilation and calculation and is the most advanced atomic structure modeling tool to date. In the construction of this model, over 15,000 oscillator strengths were calculated; these were reduced, via statistical averaging, to over 450 lines from over 100 different excited levels in 11 ions from Na-like Kr XXVI to H-like Kr XXXVI. Nearly 600 electron impact excitation rates, 150 collisional ionization rates and photoionization cross-sections, and 15 effective dielectronic recombination rates were necessary to complete a model suitable for use in our collisional-radiative equilibrium (CRE) ionization/radiation code. The atomic energy levels used in the krypton model are listed in Table I along with their statistical weights; as is evident, significant level averaging has been done to account for the bulk of the radiation while keeping only 12 excited states per ionization stage.

As an illustration of how the predictions of various approximations compare in dense plasmas, our CRE model has been used to calculate the values of various ionization and radiation quantities in a dense (10^{20} ions/cm³) krypton plasma. In Fig. 3, the effective ionization state of the plasma is plotted versus electron temperature, for three different models: CRE, LTE, and Corona. Also shown is the curve for CRE with opacity effects included for an optically thick cylindrical plasma (radius = 500 μ m). For this density, the plasma is nearly in LTE at low temperatures, while the corona model gives accurate results at high temperature. As the density increases, the CRE results will tend closer to the LTE curve. The fractional ion abundances (including excited state densities) are shown in Fig. 4 as a function of temperature. Only the L and K-shell ions are included as well as the Mg and Na-like ions since no excited-level structure was included in the model for Kr I - Kr XXIV. Also shown is the result for the Ne-like ion as predicted by the corona model. Notice both the peak abundance as well as the temperature at which it occurs are in disagreement. This is an important result for x-ray laser studies of

population inversions in Ne-like systems, since the gain prediction for an experimental plasma configuration is a strong function of the ground state density; an error from 1.0 to 1.8 keV in the temperature corresponding to peak Ne-like abundance will have a significant effect on this prediction.

However, the peak-abundance temperature is not necessarily the value one wants to attain experimentally. In Fig. 5, the line intensities for several Ne-like transitions are shown versus temperature for a krypton plasma at 10^{20} ions/cm³. Note that although the total ion population density peaks at about 1.0 keV (see Fig. 4), the line intensities peak at nearly 1.3 keV. This is due to the fact that the line intensities are nearly proportional (exactly proportional in coronal equilibrium) to the product of the ground state population and the electron impact excitation rate of the upper level of the bound-bound transition. Thus, if a population inversion can be attained in the plasma, the electron temperature at which maximum gain can be realized will probably be somewhere between the values predicted by Figs. 4 and 5.

The gross radiation characteristics of the krypton plasma are shown for the various models in Fig. 6 as a function of temperature. The CRE "thick" results are also shown for the same geometric conditions as stated earlier. Neither the LTE nor the coronal model predict the functional form of the radiational cooling very realistically, until 30-50 keV temperatures, where bremsstrahlung is the dominant radiative mechanism. The LTE predictions are by far the worst, calculating an intense peak in the K-shell radiation at the same temperatures that CRE results indicate the L-shell radiation is peaking. The corona model, on the other hand, predicts an incorrectly large M-shell peak at about 0.6 keV, since collisional quenching is neglected in the coronal approximation. Note that opacity effects tend to reduce the radiative cooling by about a factor of three for these conditions at plasma temperatures corresponding to peak L-shell emission (~2.5 keV).

Finally, a breakdown of the various radiating mechanisms is shown in Fig 7, for the same conditions as Fig. 6. The contributions due to bound-bound (lines), bound-free (recombination) and free-free (bremsstrahlung) radiation are illustrated, as well as the K-line radiation as a function of electron temperature. At low temperatures, line emission is totally

dominant, while bremsstrahlung takes over at about 30 keV. The radiative recombination, although clearly not a factor in the total radiation at 10^{20} ions/cm³, can become dominant as the density increases. However, the density at which this occurs is an increasing function of plasma material Z. Thus, in laser-heated targets, for example, bound-free processes may dominate the radiational cooling for carbon and aluminum while materials like molybdenum and gold radiate mainly via line emission.

As an illustration of a typical krypton emission spectrum, the emission from a puff plasma with a linear temperature gradient (1.0-8.0 keV) is shown in Figs. 8a-8d.

Interesting features of the spectrum include line emission gap from 1.0-1.6 keV (Fig. 8b); the $\Delta n=0$ L-shell transitions lie below the gap while the $\Delta n=1,2,\dots$ transitions all lie above it. The M-shell lines (not included in this model) all lie below 900 eV and, hence, will not fill the empty region with line emission. Above 2.8 keV, the line emission ceases once more (Fig. 8c) until finally the K-shell Lyman series lines appear at 13.0 keV (Fig. 8d).

This model can be used both as a diagnostic post-processor (in conjunction with our CRE model) or as an on-line radiation routine, used with our 1-D MHD gas puff implosion code. Presently, we are attempting to reduce the size of this model significantly for more efficient and economical implementation in the hydro codes, while yet maintaining the bulk radiation energetic properties of the model to high accuracy. It will be possible to insure this accuracy by detailed comparison between the reduced and full-blown versions of the krypton model.

III. DIELECTRONIC SATELLITE LINE MODEL

The main emphasis of the program in plasma diagnostics development this year centered on the construction of a model for dielectronic satellite lines. Satellite lines are emitted as a consequence of the radiative decay of doubly-excited levels and lie close to main resonance lines in the emission spectrum. The importance of these spectral features to the DNA-PRS program lies in their value as plasma temperature and

density indicators coupled with their prominence in the spectrum of gas puff and wire array implosions; the lines of special interest to the program are the lithiumlike and heliumlike satellites.

One of the main advantages of using satellite lines as plasma diagnostics is that both they and the resonance lines are populated by electron collisions with the same ground state. This removes, somewhat, the uncertainty of the ionization balance from the density and temperature determinations. The preliminary study of these features, describing the construction of the model and the temperature and density variation of the satellite line intensities have been documented in a detailed publication; a reprint of this paper can be found in the Appendix B of this report.

Table 1 - Atomic energy levels and statistical weights for krypton

<u>Kr I - Kr XXV</u>		<u>Kr XXVIII (F-like)</u>	
ground states only			
<u>Kr XXVI (Na-like)</u>			
$1s^2 2s^2 2p^6 3s$	2	$1s^2 2s^2 2p^5 (^2P)$	6
3p	6	$2s 2p^6 (^2S)$	2
3d	10	$2s^2 2p^4 3s$	30
4s	2	$2s^2 2p^4 3p$	90
4p	6	$2s^2 2p^4 3d$	150
4d	10	$2s 2p^5 3s$	24
4f	14	$2s 2p^5 3p$	72
5s	50	$2s 2p^5 3d$	120
6s	72	$2s^2 2p^4 4s$	480
		$2s 2p^5 4s$	384
		$2s^2 2p^4 5s$	1350
		$2s 2p^5 5s$	1944
		$2s^2 2p^4 6s$	
		$2s 2p^5 6s$	
<u>Kr XXVII (Ne-like)</u>			
$1s^2 2s^2 2p^6 (^1S)$	1	<u>Kr XXIX (O-like)</u>	
$2s^2 2p^5 3s (3/2)$	8	$1s^2 2s^2 2p^4 (^3P_2)(^1S_0)$	6
$2s^2 2p^5 3s (1/2)$	4	$2s^2 2p^4 (^3P_1)(^1D_2)$	8
$2s^2 2p^5 3p (3/2)$	24	$2s^2 2p^4 (^3P_0)$	1
$2s^2 2p^5 3p (1/2)$	12	$2s 2p^5 (^3P)$	9
$2s^2 2p^5 3d (3/2)$	40	$2s 2p^5 (^1P_1)$	3
$2s^2 2p^5 3d (1/2)$	20	$2p^6 (^1S_0)$	1
$2s 2p^6 3s$	4	$2s^2 2p^3 3s$	360
$2s 2p^6 3p$	12	$2s 2p^3 3s$	270
$2s 2p^6 3d$	20	$2s^2 2p^3 4s$	640
$2s^2 2p^5 4s$	192	$2s 2p^4 4s$	480
$2s^2 2p^5 5s$	300		
$2s^2 2p^5 6s$	432		

Table 1 (Cont'd) - Atomic energy levels and statistical weights for krypton

<u>Kr XXX (N-like)</u>		<u>Kr XXXII (B-like)</u>	
$1s^2 2s^2 2p^3 (^4S_{3/2})$	4	$1s^2 2s^2 2p (^2P_{1/2})$	2
$2s^2 2p^3 (^2D)(^2P_{1/2})$	12	$2s^2 2p (^2P_{3/2})$	4
$2s^2 2p^3 (^2P_{3/2})$	4	$2s 2p^2 (^4P)$	12
$2s 2p^4 (^4P)$	12	$2s 2p^2 (^2D)(^2P_{1/2})$	12
$2s 2p^4 (^2D)$	10	$2s 2p^2 (^2S)(^2P_{3/2})$	6
$2s 2p^4 (^2S_{1/2})(^2P_{3/2})$	6	$2p^3 (^4S)$	4
$2s 2p^4 (^2P_{1/2})$	2	$2p^3 (^2D)(^2P_{1/2})$	12
$2p^5 (^2P)$	6	$2p^3 (^2P_{3/2})$	4
$2s^2 2p^2 3s$	270	$2s^2 3s$	18
$2s 2p^3 3s$	720	$2s 2p(1/2) 3s$	82
$2s^2 2p^2 4s$	480	$2s 2p(3/2) 3s$	134
$2s 2p^3 4s$	1280	$2s^2 4s$	32
		$2s 2p 4s$	384
<u>Kr XXXI (C-like)</u>		<u>Kr XXXIII (Be-like)</u>	
$1s^2 2s^2 2p^2 (^3P_0)$	1	$1s^2 2s^2 (^1S_0)$	1
$2s^2 2p^2 (^3P_1)(^1D_2)$	8	$2s 2p (^3P)$	9
$2s^2 2p^2 (^3P_2)(^1S_0)$	6	$2s 2p (^1P_1)$	3
$2s 2p^3 (^5S_2)$	5	$2p^2 (^3P_0)$	1
$2s 2p^3 (^3D)$	15	$2p^2 (^3P_1)(^1D_2)$	8
$2s 2p^3 (^3P_{0,1})(^1D)(^3S)$	12	$2p^2 (^3P_2)(^1S_0)$	6
$2s 2p^3 (^3P_2)(^1P_1)$	8	$2s 3s/3p$	16
$2p^4 (^3P_{0,2})$	6	$2s 3d$	20
$2p^4 (^3P_1)(^1D_2)$	3	$2p(1/2) 3s$	44
$2p^4 (^1S_0)$	1	$2p(3/2) 3s$	64
$2s^2 2p 3s$	108	$2s 4s$	36
$2s 2p^2 3s$	540	$2p 4s$	192
$2s^2 2p 4s$	192		
$2s 2p^2 4s$	960		

Table 1 (Cont'd) - Atomic energy levels and statistical weights for krypton

Kr XXXIV (Li-like)

$1s^2 2s$	2
2p	6
3s	2
3p	6
3d	10
4d	32
5d	50

Kr XXXV (He-like)

$1s^2 (^1S)$	1
$1s2s (^3S)$	3
$1s2s (^1S)$	1
$1s2p (^3P)$	9
$1s2p (^1P)$	3
$1s3d (^3L)$	27
$1s3d (^1L)$	9
$1s4d$	64
$1s5d$	100

Kr XXXVI (H-like)

1s	2
2d	8
3d	18
4d	32
5d	50

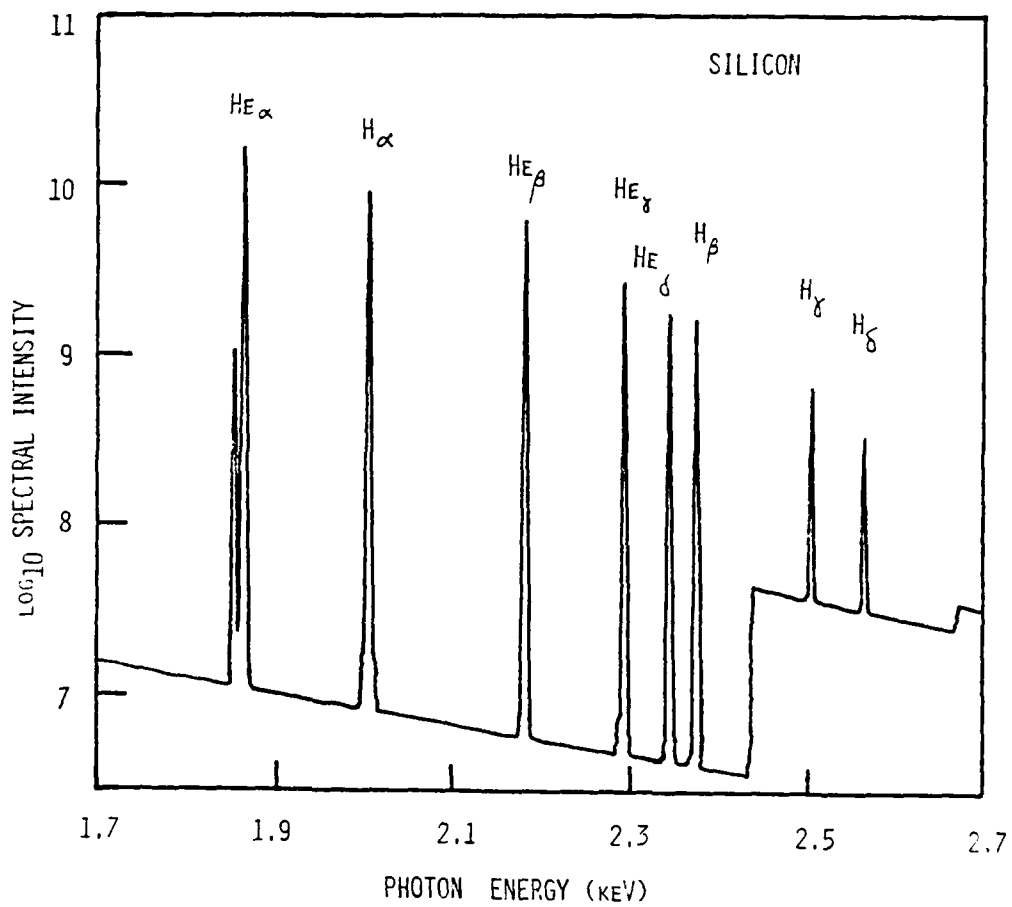


Fig. 1 Theoretical CRE silicon K-shell spectrum at $T_e = 1.0$ keV.

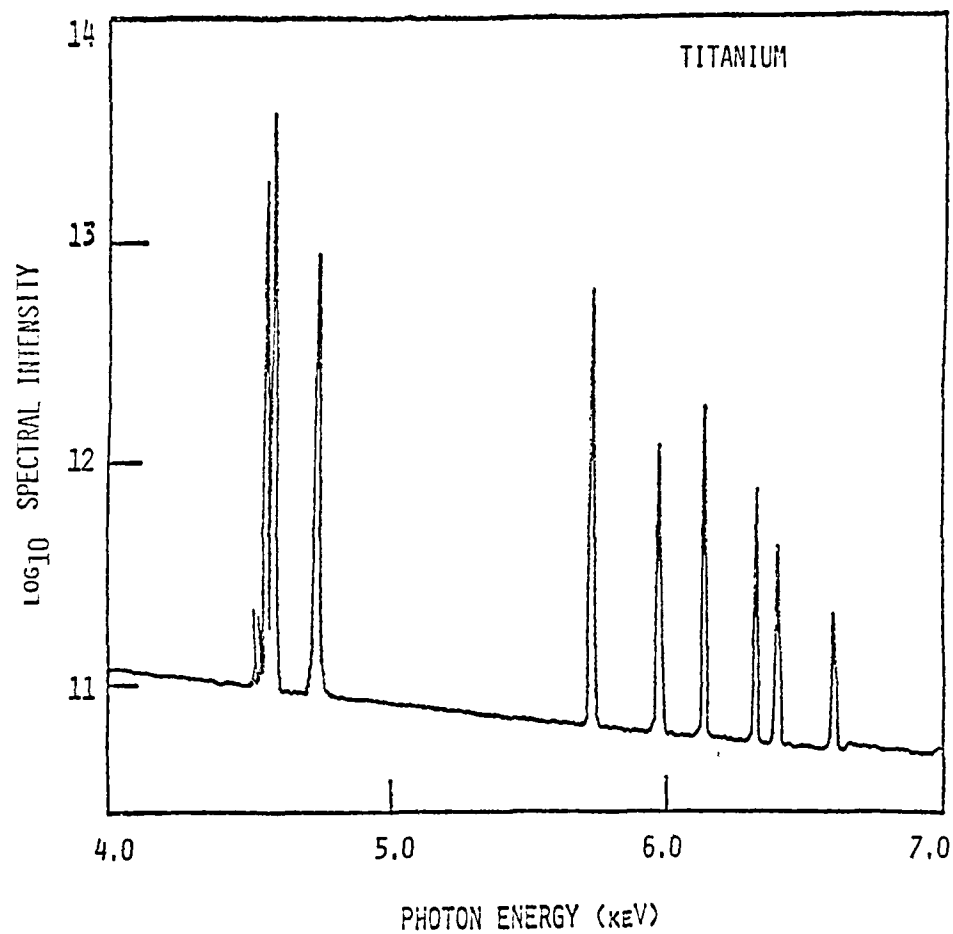


Fig. 2 Theoretical CRE titanium K-shell spectrum at $T_e = 2.0$ keV.

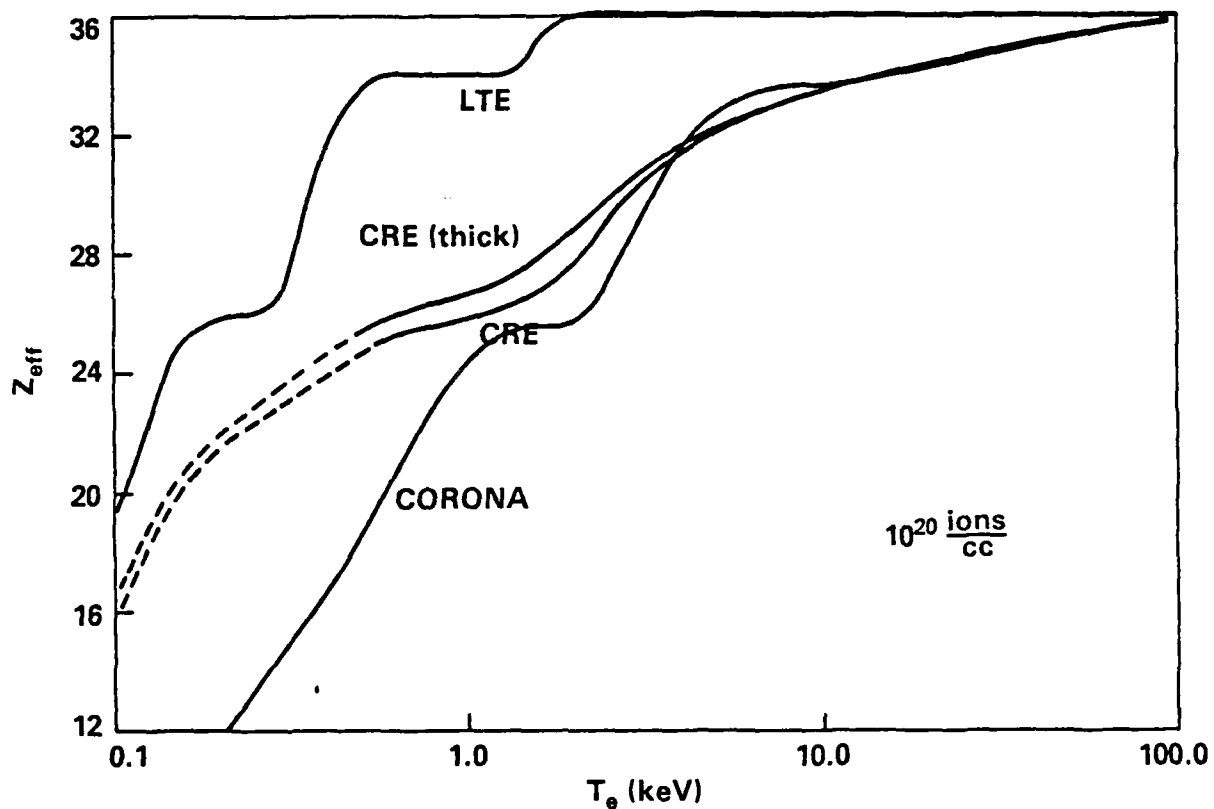


Fig. 3 Comparison of the Z_{eff} of a krypton plasma at $10^{20} \text{ ions/cm}^3$ as predicted by LTE, Corona, CRE (thin), and CRE (thick, radius = $500 \mu\text{m}$) by a corona model.

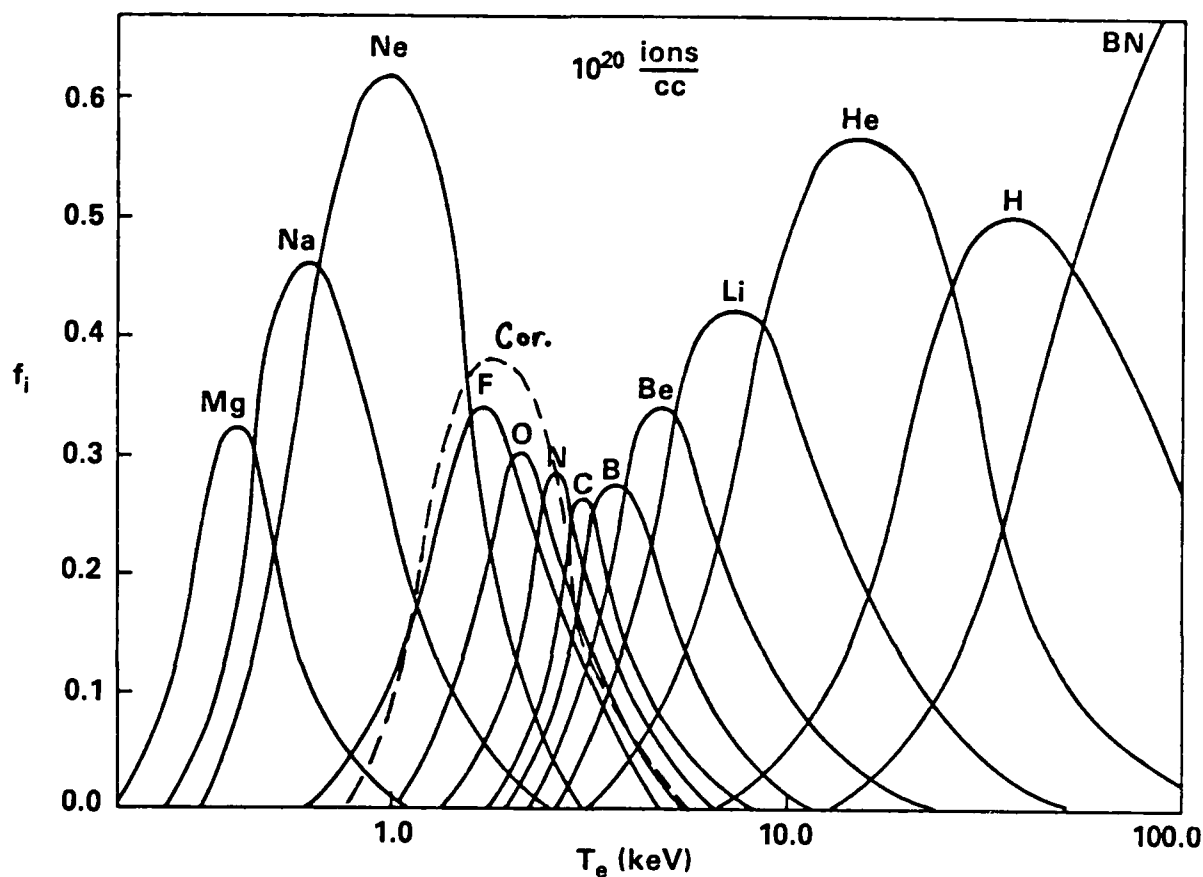


Fig. 4 Fractional ion abundances (CRE) of an optically thin krypton plasma at 10^{20} ions/cm³. Also shown is the Ne-like abundance as predicted by a corona model.

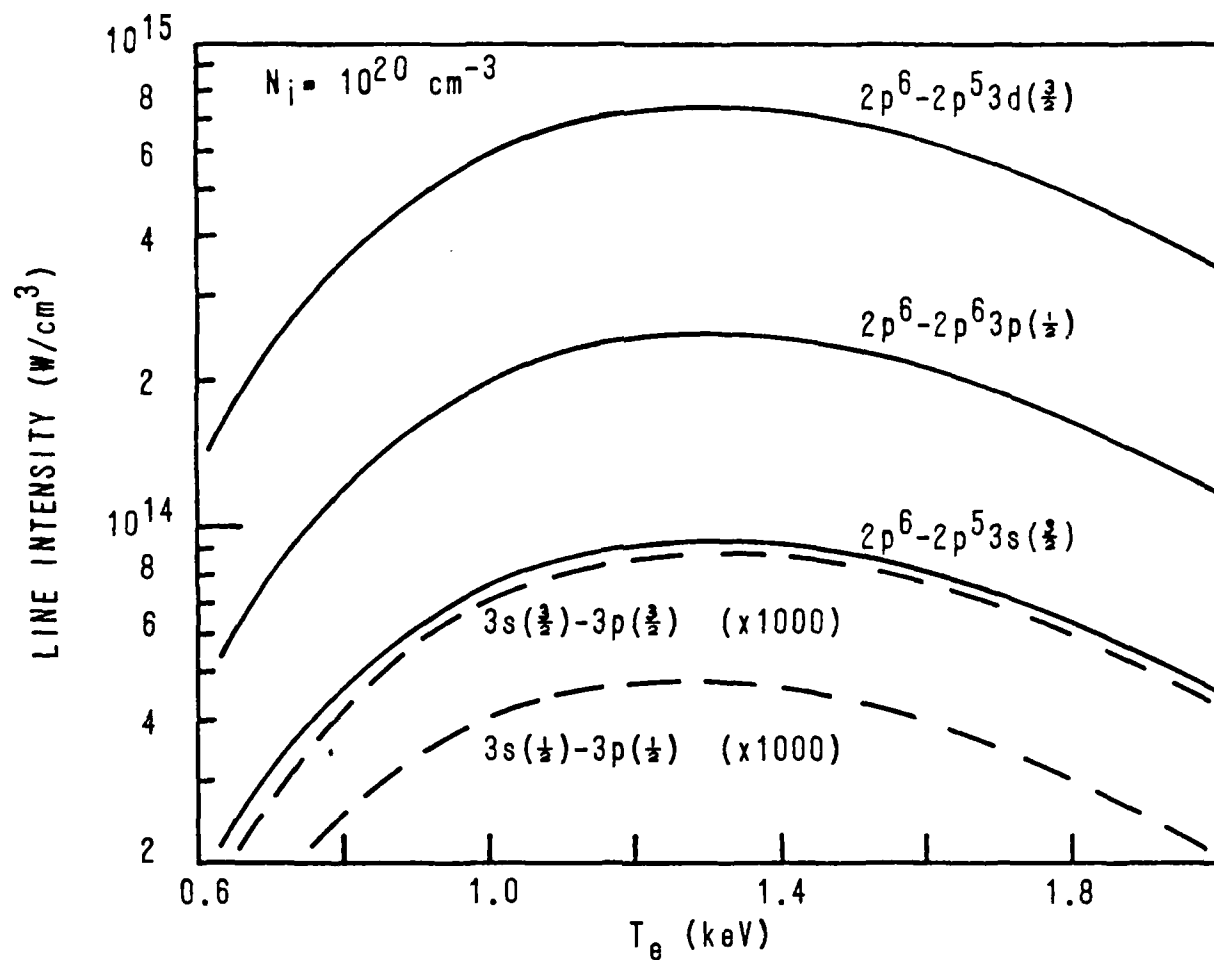


Fig. 5 Line intensities for several Ne-like emission lines from an optically thin krypton plasma at 10^{20} ions/cm³.

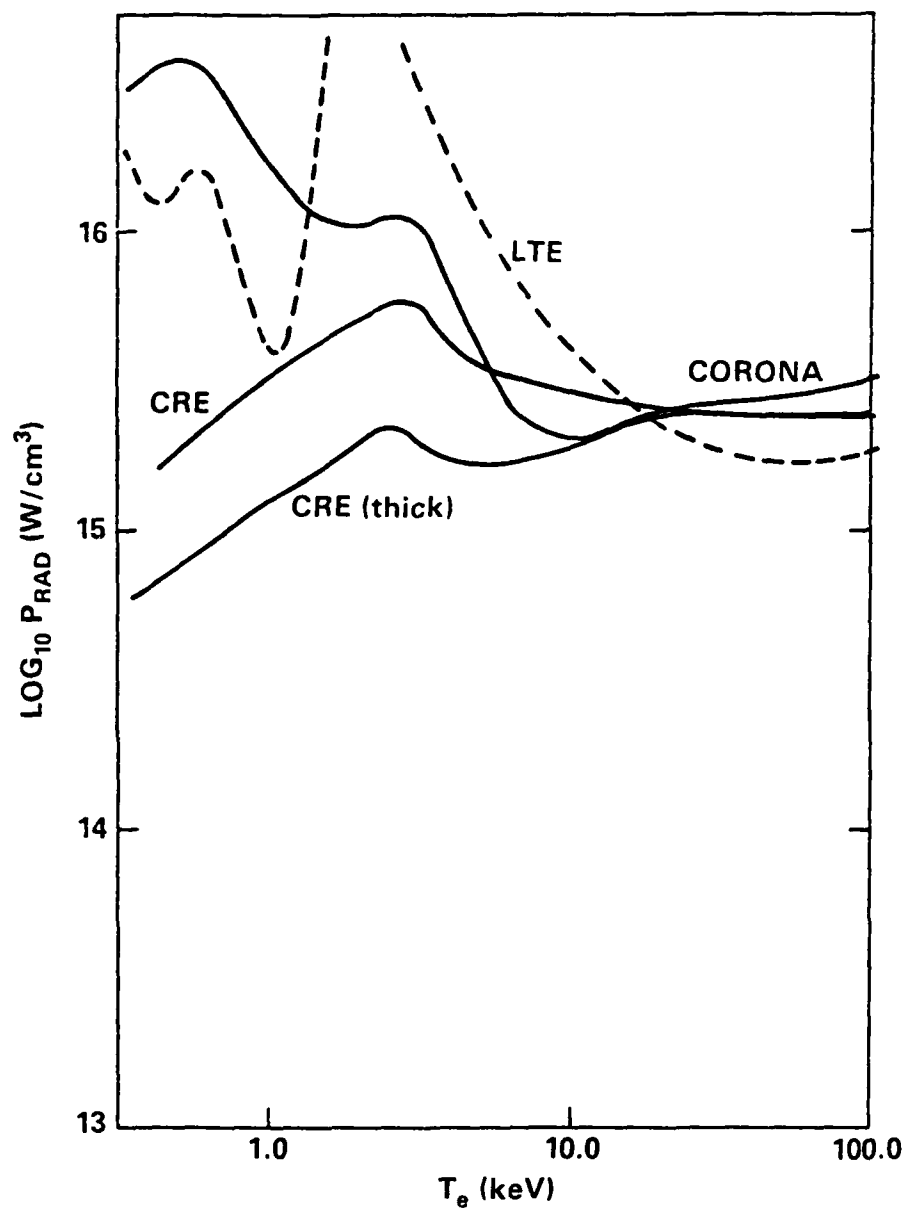


Fig. 6 Radiative cooling curve for a krypton plasma at 10^{20} ions/cm³ comparing predictions from LTE, Corona, CRE (thin), and CRE (thick, radius = 500 μm) models.

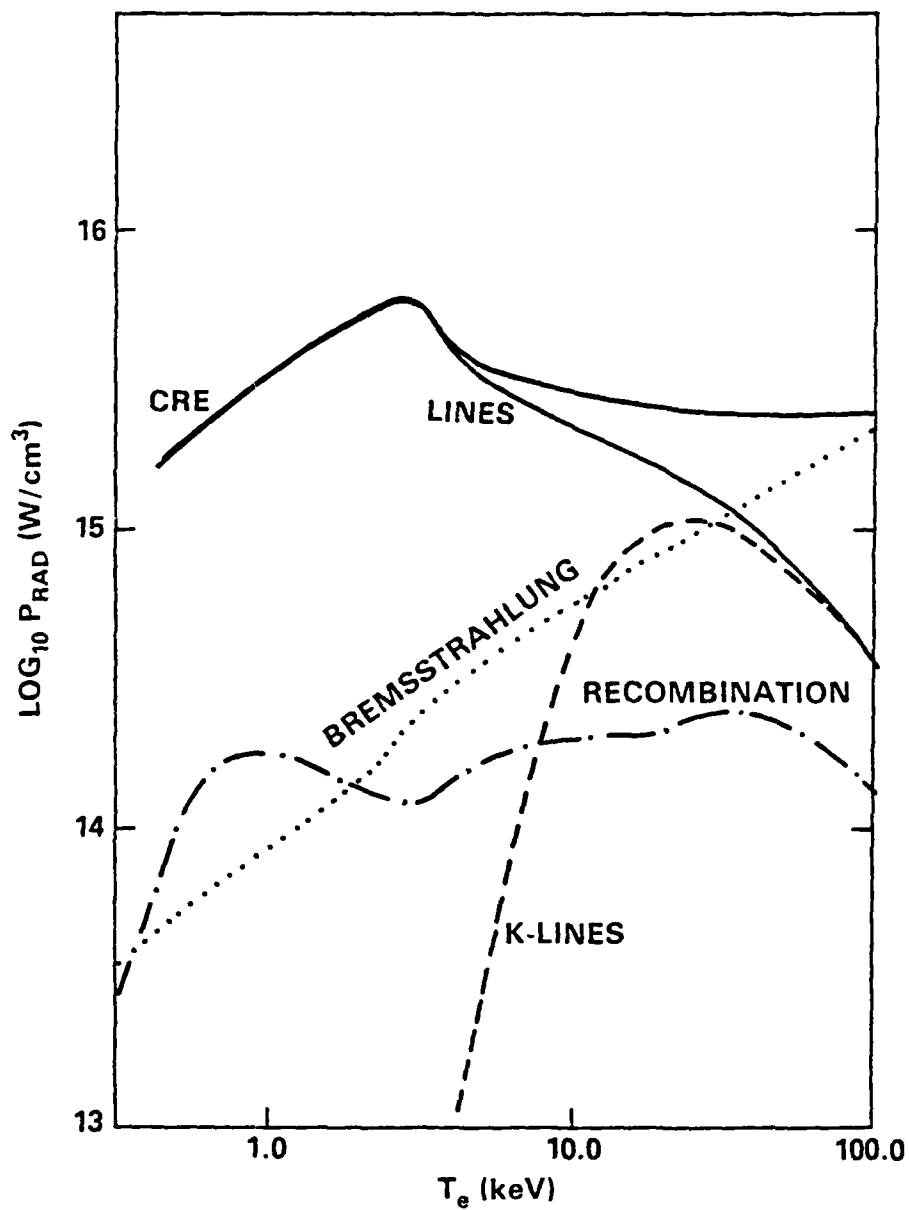


Fig. 7 The CRE radiative cooling curve for krypton, as in Fig. 6, showing the contributions by line, recombination and bremsstrahlung emission, also shown in the K-line radiation.

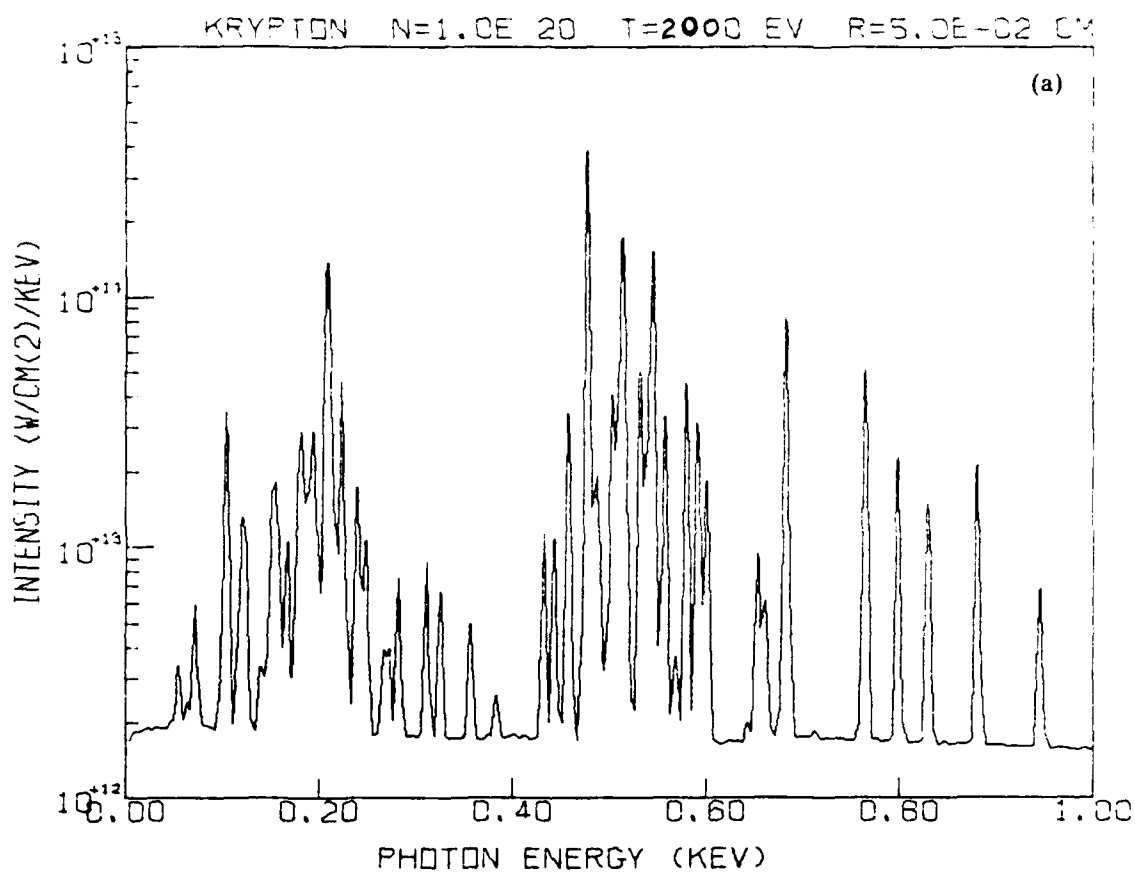


Fig. 8 Theoretical CRE krypton spectrum from 0-18 keV at $T_e = 2.0$ keV.

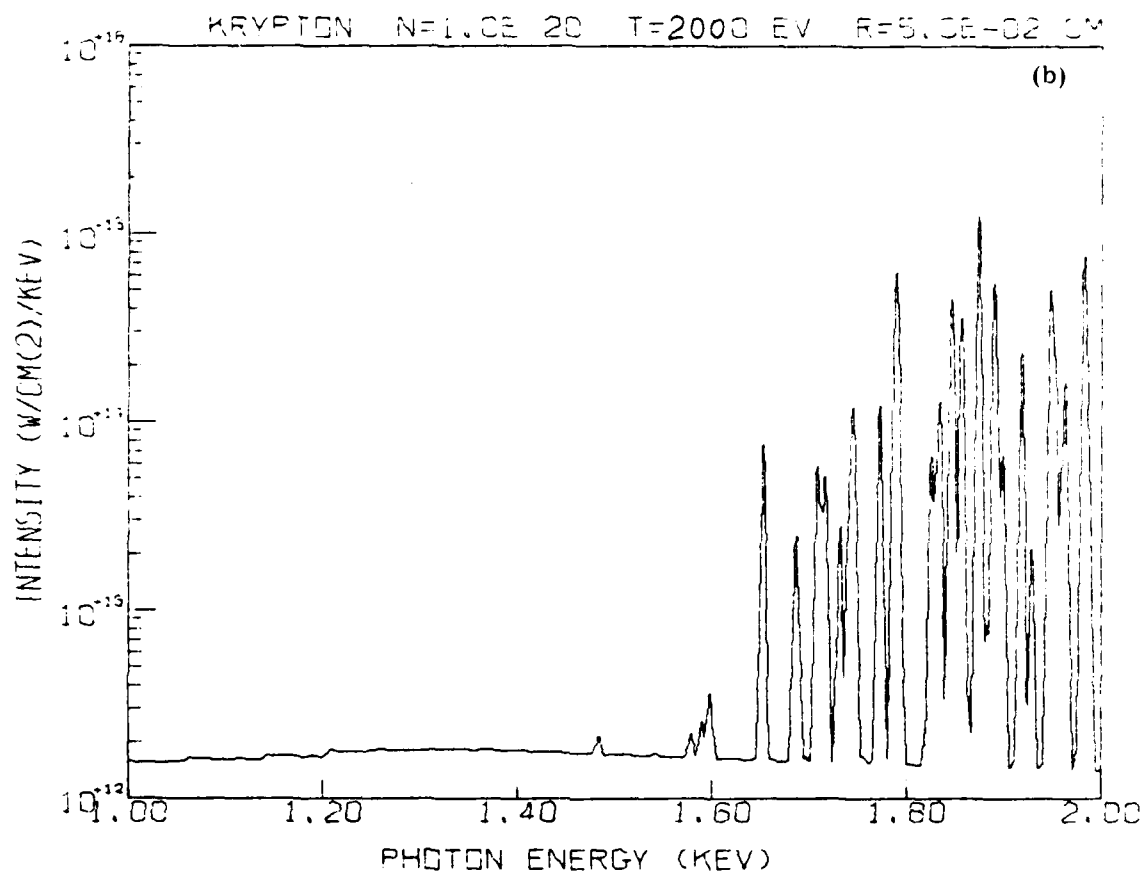


Fig. 8 (Cont'd) Theoretical CRE krypton spectrum from 0-18 keV at $T_e = 2.0$ keV.

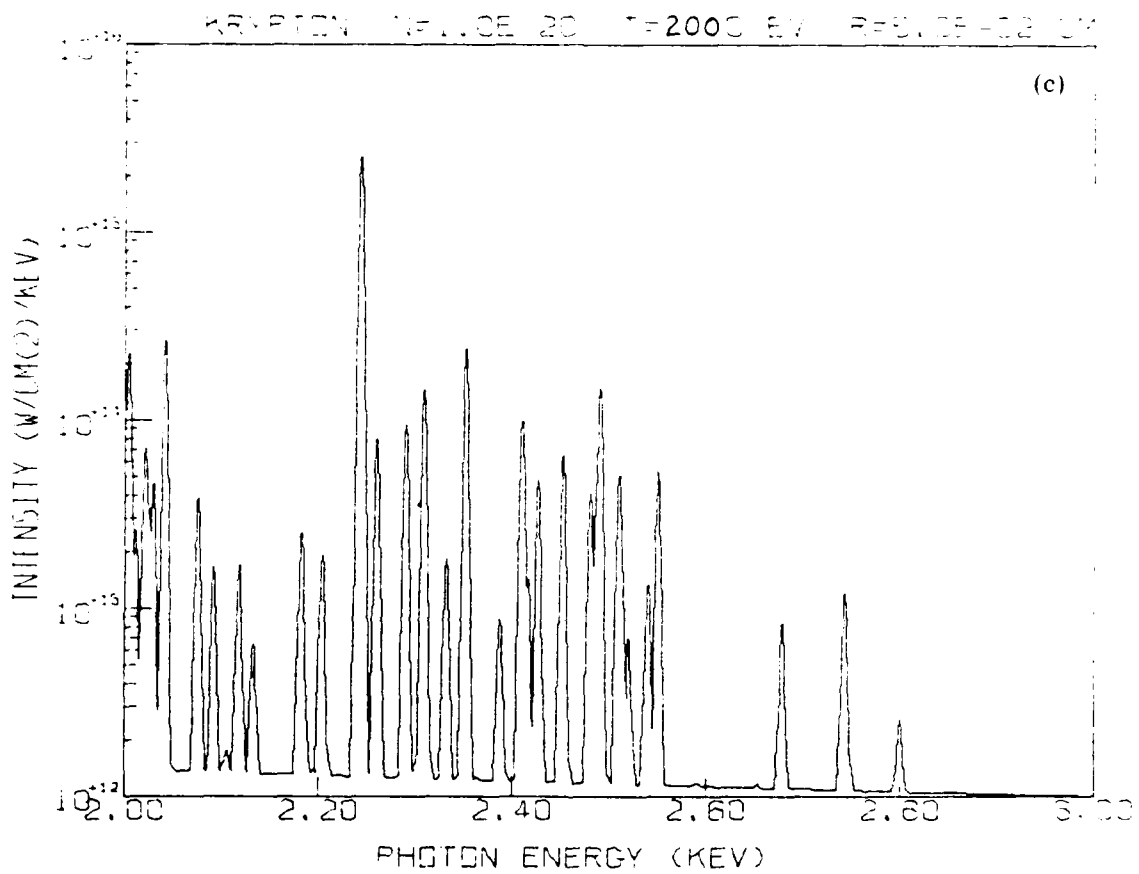


Fig. 8 (Cont'd) Theoretical CRE krypton spectrum from 0-18 keV at $T_e = 2.0$ keV.

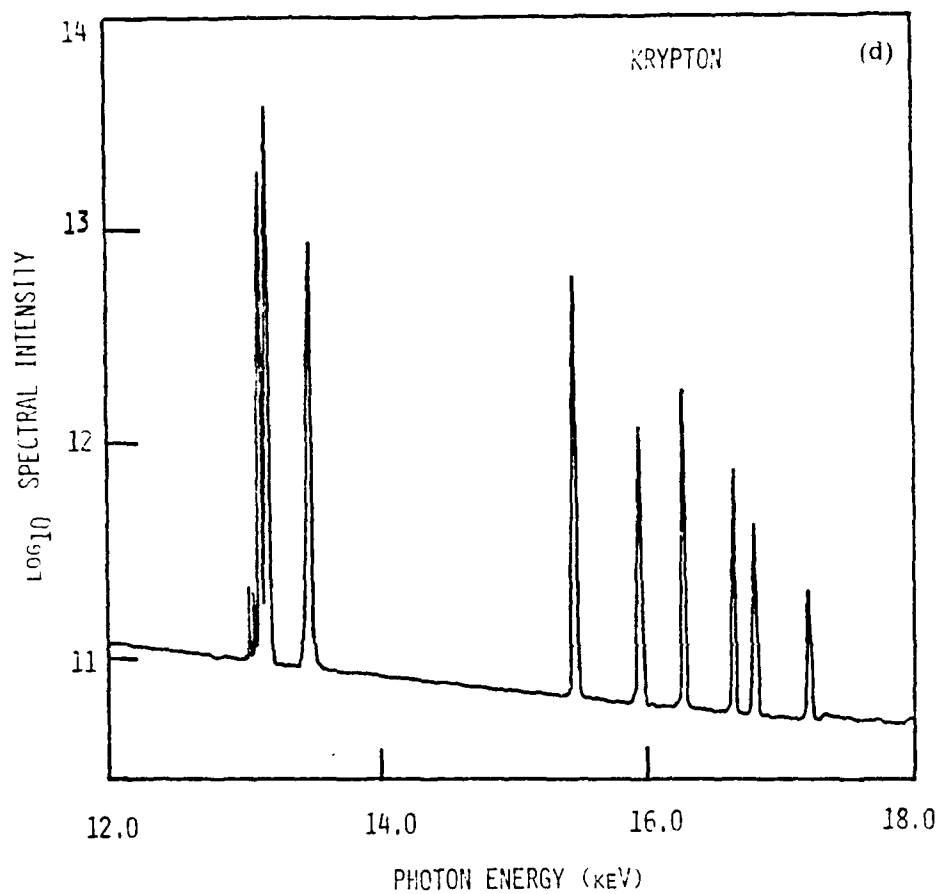


Fig. 8 (Cont'd) Theoretical CRE krypton spectrum from 0-18 keV at $T_e = 2.0$ keV.

C. Detailed Modeling of Ionization/Radiation in Dense Plasmas

I. INTRODUCTION

In this section, some of the problems involved in modeling plasma radiation via the detailed configuration accounting method are discussed. This consists of a collection of ideas, suggestions and difficulties encountered over several years of work on the DNA-PRS program by several members of the NRL Plasma Radiation Branch. The main thrust of this discussion is an illustration of why such detailed methods are necessarily brought to bear on DNA radiation programs and why more approximate modeling techniques yield unacceptably incorrect predictions. In order to make this point as clearly as possible, the discussion will be maintained in a totally qualitative context.

As a preview of how the calculations from which the results were gleaned are performed, a short description of the modeling techniques is required. Briefly, a set of atomic rate equations is solved for the population densities in a plasma as a function of ion density, electron and ion temperature, and geometric configuration. Each equation describes collisional processes affecting a specific atomic level and includes rate coefficients from all important atomic processes. In addition to particle collisions, radiation transport is also included in the model using either photon probabilistic techniques or a multi-frequency ray-trace solution of the equation of transfer, solved in variable 1-dimensional geometry. The basis for the accuracy of such calculations is the quality of the cross-sections employed. Presently we use a mixture of state-of-the art calculations and simple hydrogenic approximations to generate the atomic data; a more in-depth discussion of data compilation, however, will be presented below.

The discussion has been divided into three areas:

- (1) Atomic Data Compilation
- (2) Model Construction and Numerical Constraints
- (3) Model Implementation and Application.

II. ATOMIC DATA COMPILATION

A. Level Structure

The first stage in the radiation modeling is usually the calculation or compilation of the necessary data base. Before this can be accomplished, a suitable or appropriate level structure must be selected. The selection involves a decision to limit (i) the number of ions to model in detail and (ii) the number of excited levels to include in these ions. The former depends on the temperature and density regime to be modeled. To analyze soft x-ray spectra from a laser microballoon implosion with argon-doped fuel¹, for example, the two K-shell ions and the lithiumlike system (which can effect the x-ray diagnostics, especially satellite lines) are sufficient. A radiation-hydrodynamic treatment of a gas-puff implosion or a laser-heated foil², on the other hand, requires the modeling of excited levels in many ions to adequately treat the radiation over the wide range of electron temperatures encountered in these experiments. Since this is a rather obvious point, let me proceed directly to the second (and much more subtle) point. One wants to limit the number of excited levels per ion for two reasons:

(1) the number of cross-sections required to be calculated increases by almost n^3 (where n is the principal quantum number) as more excited states are included, and,

(2) the required computation time for radiation modeling increases as the number of bound-bound transitions (hence, levels) increases, particularly due to radiation transport.

Presented below are two examples of how the number of excited levels included in a model can disturb the population densities. In Fig. 1, the fractional ion abundances (ground plus excited states) of an aluminum plasma at 10^{22} ions/cm³ versus electron temperature is shown. The calculation is for a plasma in collisional-radiative equilibrium (CRE) in an "optically thin" plasma environment (radiation transport is not included). Notice the variation in the lithiumlike Al XI abundance as fewer excited levels are included in the level structure. One is spared the endless task of including higher n -values only by the lowering of the

ionization limit, which, at this density, lies just above the $n=6$ levels (using the interparticle-distance criteria)³. In fact, at 10^{22} ions/cm³, Fig. 1 illustrates one of the worst cases, since the effect of excited states on the ionization balance decreases as the density decreases. However, a careful determination of the lowering is obviously necessary in order to accurately predict the required number of levels and the ionization balance.

While this large effect on the ion abundances is present only at higher densities, we have discovered, very recently, that limiting the level structure in an ion can also affect the diagnostics, even at lower densities. As a consequence of our tracer-dot spectroscopy program at NRL,^{4,5} it was found that K-shell x-ray diagnostics can be misinterpreted if adequate structure is not included in the model. As an example, Fig. 2 contains a plot of several hydrogenlike to heliumlike resonance line intensity ratios for a cylindrical aluminum plasma typical of that produced by laser heating of a 115 μ m tracer-dot implant. The ion density is fixed at 10^{20} ions/cm³ and the plasma is assumed to be in CRE. Three calculations were performed with different excited level structure: (1) the solid curves represent $n \leq 10$ for both K-shell ions, (2) the dashed-dotted curves represent $n \leq 10$ for the heliumlike system and $n \leq 5$ for the hydrogenic ion, and (3) the dashed curves are with $n \leq 5$ for both K-shell ions. As can be seen from the curves, all ratios are affected by limited level structure in the heliumlike system, while only higher Rydberg members of the hydrogenic ion are affected by limiting the levels in that system. The error in the temperature determination is 50-200 eV at this density, depending on which line ratio is used. Of course, the effect is exacerbated at higher ion densities but, again, is limited by the cutoff in n due to lowering of the ionization limit. The message of Figs. 1 and 2, however, is clear: care must be taken in selecting level structure adequate to describe the main population densities in the density regime the model is to be applied, particularly if one's intention is to analyze experimental spectra.

B. Large Data-Base Generation

One major obstacle that must be overcome when the modeling of a large number of ions is required (as usually occurs where combined radiation/hydrodynamic simulations are performed) is the assembly of large numbers of cross-sections and/or rate coefficients. This can be a problem not only in the computational expense that must be incurred but also simply due to the large amount of time invested in amassing a large data base. For example, the krypton model just completed contains all 37 ground states, typically 10 excited levels in each of 11 ions (Na-like through H-like), over 500 oscillator strengths, nearly 150 collisional ionization rates, 150 photoionization cross-sections, 12 effective dielectronic recombination rates and over 600 electron impact excitation rates. To construct such models efficiently requires rapid, inexpensive mathematical expressions, such as: the exchange classical impact parameter (ECIP)⁶ or Lotz formula⁷ for impact ionization, the hydrogenic Seaton formula for photo-ionization, the Bates-Damgaard⁸ formula for oscillator strengths, a semi-classical impact parameter (SCIP)⁹ calculation for impact excitation, and the Burgess-Merts¹⁰ formula for dielectronic recombination. From these rates or cross-sections one calculates collisional and radiative recombination and electron collisional de-excitation via detail balancing. Although these (and other) methods reduce the expense and time requirements significantly, the quality of the coefficients is questionable in several cases. This leads us to the discussion in the next section.

C. Quality of the Rate Coefficients

Of course, we are all aware of the effect that the fusion effort and scientific space program have had on the atomic physics community over the last two decades. The need for comprehensive sets of accurate collisional data for higher Z materials and higher charge states has stimulated many workers to develop highly sophisticated theoretical techniques for calculating these cross-sections. This allows model builders to be more selective in making a "wish-list" for the type of rate coefficients they would like to include in the models. For example, with a Hartree-Slater atomic structure code (such as those of Cowan or Scofield) one can obtain highly accurate bound and continuum wave functions, energy level

eigenvalues and oscillator strengths. With these wave functions and the proper potentials, one can also generate quality photoionization cross-sections. Also, using these wave functions, autoionization rates are obtained for use in calculating accurate ionization cross-sections via a Coulomb-Born Distorted Wave calculation (with the effects of excitation-autoionization included, of course). Similarly, excitation rates can be computed via either the distorted wave or close-coupling techniques, including the relevant autoionizing resonances. One now has a highly accurate set of computer codes for calculating everything needed for a sophisticated atomic model; however, the expense and time investment required to exercise them is still prohibitive. Eventually, atomic physicists will no doubt be persuaded to use their expertise, coupled with their sophisticated structure and scattering codes, to parameterize large numbers of coefficients, perhaps along iso-electronic sequences in a way that can be easily adapted or implemented by the model builders. Some of that has already been accomplished by Sampson¹¹ and co-workers at Penn. State U. with impact excitation collision-strengths, but more work along this line is sorely needed if comprehensive sets of accurate rate coefficients are to be made easily accessible to the community of workers who need them.

III. MODEL CONSTRUCTION AND NUMERICAL CONSTRAINTS

A. Diagnostics or Energetics?

The question posed by the preceding subtitle may be puzzling to some of you, but to radiation modelers it's an all too familiar one. Often, a choice has to be made during the construction of a model as to whether it will be used in conjunction with a hydrodynamic model for predicting radiation energetics or as simply a stand-alone tool for post-processing or diagnosing experimental data. While these applications are not necessarily at cross-purposes with one another, a model is usually designed exclusively for only one application for reasons discussed earlier in the section on limiting the number of levels. However, in many cases where an energy level is required for both energetic and diagnostic purposes, one can still reduce computational time by cleverly averaging over a group of levels

which lie close in energy. As an example, there are eight $n\ell$ levels in the $n = 4$ state of heliumlike ions: the 4s, 4p, 4d, and 4f states in the single and triplet systems. In a dense plasma, however, one can often make the safe assumption that electron-ion or ion-ion collisions¹² will maintain a Boltzmann statistical equilibrium among the $n\ell$ components. Thus, by taking appropriate weighted averages of the various rate coefficients coupling the 4ℓ levels to surrounding states, the eight $n = 4$ levels can be reduced to one with little loss of accuracy in calculating the radiation from decay of the $n = 4$ state. Of course, what is sacrificed is the finer details of the spectral emission, since, for example, a single 3d-4 line will be calculated whereas both a 3d-4p and 3d-4f will be detected in the experimental spectrum. In this way, one sacrifices more detailed spectral calculations for reduced memory storage and computation time, both of which can impact the usefulness of large radiation-hydrodynamic calculations. At NRL, the solution to this problem is currently being pursued by way of a two-pronged attack. The full models with more-detailed level structure are constructed first. These are then used in experimental analysis (e.g., tracer-dot spectroscopy and Z-pinch diagnosis) or in post-processing hydro code plasma profiles (e.g., x-ray laser studies). Then, extensive averaging of levels and rates is done to construct a much-reduced model suitable for hydro code applications, with the advantage that the predictive capabilities of the reduced model can be checked and benchmarked with the more complete version for accuracy. Using this technique, we are currently reducing our 500-level krypton model to a 66-level version for implementation in our MHD codes. The differences between these models will be discussed in depth in a report to appear later.

B. Short-Cuts to Population Densities

As was stated earlier, our CRE radiation/ionization models are based on the solution of coupled atomic rate equations to calculate the various level populations. Because of the complexity of the method and the large data base requirements, attempts are often made to use simpler but more approximate alternatives to determine the state densities. Considering only schemes which still maintain detailed configuration accounting (as opposed to average-atom models), the methods fall into three basic categories: (1) local thermodynamic equilibrium (LTE) models,¹³ which

solve the Saha and Boltzmann equilibrium relations to get population densities, and are applicable in the high plasma density limit, (2) corona models¹³ which solve a set of equilibrium balance equations, neglecting collisions when in competition with radiative processes, and are valid in the low density limit, (3) a group of "approximately CRE" models which, like CRE, are valid over a wide range of plasma densities, but employ some special mathematical techniques to reduce the necessary atomic data or computation time. Examples of these would be the method based on population probabilities by Salzmann¹⁴ and the "mixed model" of Busquet.¹⁵ In general, all of these models can give rather accurate results for the population densities when applied to the plasma regimes for which they were designed, and it is not our intent to detract from their value in determining the level distributions. However, we have found that using short-cuts to determine the population densities does little to reduce the labor or cost of accurately predicting the radiation output. There are two fundamental reasons for this. First, one still requires all the oscillator strengths to make accurate predictions of line emission, as well as all the radiative recombination rate coefficients to accurately calculate the bound-free emission. Second, the major computational cost of performing radiation calculations lies in the radiation transport algorithm, not in the ionization balance calculation. Hence, one avoids neither the toil of compiling the atomic data nor the necessary cost of computation by using more approximate models, if the radiation field is a required result. The inevitable conclusion we have arrived at, therefore, is that one may as well construct and implement the complete CRE model.

C. Radiation Transport

As well as calculating the collisional effects on the ionization balance, reabsorption and transport of radiation must also be taken into account in these dense plasmas. Since the transport calculation usually accounts for a major portion of the computational time, it is crucial that the method be made as efficient and economical as possible. Our group at NRL uses two different techniques to transport radiation in ionization/radiation models: (1) probabilistic photon reabsorption, and (2) frequency-by-frequency ray-trace solution of the transfer equation.

The details of both of these methods have been published previously^{2,16-20} and so I will spare you complicated descriptions and formulas. Basically, the probabilistic technique treats individual spectral features (e.g., lines or recombination edges) distinctly, and calculates probabilities that photons emitted in one plasma zone will be absorbed in another. By taking into account various line broadening mechanisms and geometric factors in summing and differencing the probabilities, the emitted radiation intensity as well as the photon pumping rates (the effect of re-absorbed photons on the rate equations) can be calculated. The frequency-by-frequency method, on the other hand, involves tracing the photon paths via rays through the plasma at individual frequencies, obtaining a solution for the radiative intensity, I_ν , by solving the equation of radiative transfer. The difference between the methods is that the probabilistic method is essentially the ray-trace technique averaged over path angle and over the frequencies of the spectral feature. Both methods have been carefully benchmarked with each other to insure that the predicted spectral intensities and energy transfer compare well over the regime of applicability of the models. What is lost by the probabilistic method are the finer details of the line profile or recombination edge; these, on the other hand, are accurately calculated by the ray-trace technique. Of course, many more spectral features can be treated by the former (due to decreased memory requirements) as well as being significantly more economical in terms of required computational time. Presently, we can use these techniques interchangeably or in combination with each other. For example, in lower density gas-puff or wire implosions ($N \approx 10^{19}$ ions/cm³) the probabilistic technique is completely adequate for both lines and recombination continua. However, at very high densities, like laser-microballoon target simulation, the multi-frequency ray-trace method is needed due to the dominance of Stark and opacity broadening. At medium densities, such as those found in laser-foil or ion beam-foil interactions, a "hybrid" model is used, whereby lines are treated probabilistically and photoionization is calculated via the multi-frequency model. Bremsstrahlung is always transported frequency-by-frequency since no probabilistic technique has as yet been developed. However, due to the smooth nature of the free-free source function with photon frequency, very few frequencies are required for accurate transport.

The final statement about radiation transport, however, is simple and to the point: newer, faster transport techniques need to be developed! The present algorithms are economical enough for implementation in one-dimensional hydro models; we demonstrated this fact in a paper earlier this year.² However, if ionization/radiation models are to be successfully integrated with 2-D codes, new, faster techniques are needed!

IV. MODEL IMPLEMENTATION AND APPLICATION

A. $\Delta n = 0$ L-Shell Transitions

It is an obvious fact to those who work at low densities (primarily the astrophysics and magnetic fusion workers) that the bulk of the non-K-shell line emission results from transitions between levels of similar quantum number ($\Delta n=0$ transitions), where $n=2$ in the L-shell, $n=3$ in the M-shell, etc. It is also well-known that as the plasma density increases to values of interest to the audience here, the $\Delta n=0$ radiation is overwhelmed at some point by the $\Delta n=1,2,\dots$ emission, due to the fact that at higher densities the excited $n=2$ states (in the L-shell) become collisionally quenched; at the same time, the rates for populating the higher n levels become great enough that the lines from these states become more intense. The question most relevant to model builders regarding this topic is: "Can one, at some point in the density, neglect the excited $n=2$ levels in the model and include levels characterized by principle quantum number along?"

To address this question, the ratio of the $\Delta n=0$ emission to the total line radiation for the carbonlike ion of krypton versus ion density is shown in Fig. 3. The electron temperature was fixed at 3 keV, corresponding to roughly the maximum of the carbonlike abundance (as shown in Fig. 4). At low densities, the $\Delta n=0$ transitions account for 80% of the total ionic line emission, but this drops to less than a percent in the high density limit. The interesting fact is that the $\Delta n=0$ emission is strong up to densities of several times 10^{19} , indicating that including the $n=2$ excited states is imperative for modeling krypton Z-pinch implosions or plasmas heated by x-ray lasers, non-coherent radiation sources, or ion beams (where low-temperature, medium-density plasmas are generated); but,

perhaps they can be neglected in laser-plasma interactions where the low-temperature L-shell emitting region is usually at high densities during much of the emission phase. Also, the density at which the $\Delta n=0$ radiation becomes negligible decreases with smaller- z materials, although no attempt has been made to quantify this with our other models, as yet. Nevertheless, all indications are that some accounting of $\Delta n=0$ line emission is necessary for accurate radiation energetics in a wide range of plasma modeling applications. Because of the limitations of several other techniques, such as the "average-ion" method, no account of Δn radiation can be taken, making them unsuitable for modeling of PRS sources.

B. Non-Maxwellian Electron Distributions

The effects of non-thermal electron distributions on various physical processes in dense plasmas is a topic of very recent interest. Areas presently under investigation include such fundamental processes as heat conduction, laser absorption and bremsstrahlung emission, for example. Recently, we have taken an interest in how non-Maxwellian distributions affect the ionic abundances and subsequent atomic radiation. To model these effects requires complete re-shaping of the atomic data base, since rate coefficients thermally averaged over Maxwellian distributions are not applicable to the problem. Instead, tables of cross-sections or collision strengths are required, enabling one to include the electron distribution as an input variable, over which the data can be averaged to obtain rate coefficients. This problem was recently addressed in an NRL paper which discussed the possibility of obtaining population inversion and gain in neon-like systems by pumping with a suprathermal electron distribution.²¹ A graph depicting the ion abundance of neonlike iron as a function of the hot electron-to-cold electron number density is shown in Fig. 4 for fixed $T_e(\text{cold}) = 70$ eV, $T_e(\text{hot}) = 800$ eV, and $N_e(\text{cold}) = 4 \times 10^{20} \text{ cm}^{-3}$. For a purely thermal plasma at 70 eV, the fraction of Fe XVII ions is below 20%. As the number of suprathermals is increased, the abundance increases to over 70% and then to zero as all the neonlike electrons are burned off. The figure to note here is that only a 1% concentration of hot electrons can totally disturb the ionization balance calculated due to a thermal bath alone. Whereas many laser-plasma interactions at high

irradiance generate this percentage of suprathermals, it is not clear that neglecting this effect in modeling such plasmas will result in an accurate assessment of the population distributions. This may be particularly true of K-shell populations where x-ray lines from K-shell ions are used to determine the local electron temperature and infer the extent of preheat due to electron thermal conduction, flux limits, etc. Some of the recent unexplained pre-heat measurements²² which attribute K-shell resonance line emission deep in the plasma to thermal conduction pre-heat may, in fact, be partly due to enhanced ionization by a low-level suprathermal electron population, as shown in Fig. 4.

C. Time-Dependent Effects

Another topic of current interest is time-dependent effects on the atomic rate equations: the deviation from ionization equilibrium due to changes in plasma parameters occurring faster than atomic collisional time scales. The standard form for the atomic rate equations is

$$\frac{dN_j}{dt} = \sum_i W_{ij} N_i - \sum_i W_{ji} N_j$$

where W_{ij} is a collisional or radiative rate from level i to level j . For a plasma in collisional-radiative equilibrium, the time derivative is set to zero and the set of steady-state equations is solved for the population densities. If the plasma is changing too rapidly to relax to an equilibrium state, the time-dependence must be retained. By expanding the total time derivative, we get two components:

$$\frac{dN_j}{dt} \equiv \frac{dN_j}{dt} + \bar{v} \frac{\partial N_j}{\partial x}$$

The first term is the explicit time dependence and comes into play when local plasma variables (N_I and T_e) change very rapidly compared to atomic transition times. Thus, when the plasma is being heated rapidly, ionization lags behind the instantaneous distribution of populations as predicted by an equilibrium model, and a lower state of ionization actually persists; the opposite is true in a cooling, or recombining plasma. As an

illustration of this effect, a comparison between the Z_{eff} in a CO_2 laser-heated plasma as calculated by a CRE and time-dependent CR model is shown in Fig. 5 as a function of time. The time-dependent temperature and density profiles for one zone of the aluminum plasma were taken from a LASNEX hydrodynamic simulation provided by Los Alamos. The standard early-time lag in ionization followed by the late-time lag in recombination is evident. Since the atomic collisional time scales are a strong function of the plasma density, that curve is also shown. For this particular shot, the deviation from equilibrium occurs as the density falls through approximately 10^{20} ions/cm³. This value will, of course, depend on the laser pulse width, irradiance, and Z of the target material. These effects are rather well-known and since quantitative studies have been published by Colombant et al.²³ and Matzen and Pearlman²⁴ several years ago, we will not dwell on it further.

Instead, we turn attention to the second term in the equation, the convective derivative. This term becomes important when the plasma flow velocity into a local region of interest is faster than the atomic collisions governing relaxation to equilibrium. If this is the case, the ionization state of this region will reflect temperatures and densities from some other location in the plasma, not the local values. This term is usually neglected in most calculations since either the flow velocity is assumed to be small or the ionization state is calculated on a Lagrangian hydro mesh which moves with the fluid, obviating the need for invoking the convective derivative in the rate equations.

Recently, however, we have become aware of flow-velocity effects in conjunction with the analysis of x-ray spectra from implanted tracer-dot experiments at NRL. To provide a little background, tracer-dot spectroscopy is a new diagnostic technique developed at NRL, by which small "dots" of a higher Z material are implanted in a lower Z laser target in order to localize in space the emission from the dot material. The spatially resolved K-line spectra thus allow the plasma profiles to be determined. This technique, as shown schematically in Fig. 6 for an aluminum dot in a carbon target, has a number of advantages over standard laser-plasma spectroscopy and has been discussed in detail elsewhere.^{4,5,25} In addition, preliminary studies of the density and temperature profiles in the blowoff region of a long density scalelength laser plasma have recently

been published²⁵ illustrating the valuable diagnostic contributions that tracer-dot spectroscopy can make. However, the nature of the technique (essentially, spectral measurements made in the lab frame of a perpendicularly flowing laser-plasma ablation) lends itself to being susceptible to the flow velocity problems alluded to earlier. Although agreement between spectroscopy, interferometry, and 2-D hydrocode modeling was good in the long-scalelength case, errors and discrepancies arose when we attempted to analyze short density scalelength plasmas. We surmised that the spectra we were analyzing were in fact not representative of the plasma region localized by the spectrometer slit, but were colored by the rapidly flowing plasma upstream from the region being detected.

To test this hypothesis, hydro profiles from the Eulerian laser code, FAST2D,²⁶ were transformed to represent time-dependent temperatures and densities which reflected the flow velocity of plasma from the laser target. These profiles were then post-processed (assuming a steady-state flow) using a time-dependent version of our CR model to predict K-line intensity ratios as a function of distance from the target. These ratios, therefore, represented the emission that would be measured from a typical laser-plasma interaction. A sample set of line ratios versus distance from the target, Z , is shown for the $H-\alpha/He-\alpha$ ratio in Fig. 7; both a long-scalelength and short-scalelength case are shown. For comparison, the set of ratios from a time-independent post-process (reflecting the actual temperature and density in the plasma) are also shown. As you can see, the line intensity ratio which would be measured (t-dep) is lower than those which reflect true plasma conditions (t-ind) at Z values close to the target, while at larger Z 's where the temperature (and, hence, the line ratio) drops, plasma flow velocity maintains the line ratio at higher values. As was expected, the faster the flow velocity (as typified by the shorter scalelength case), the greater is the discrepancy between the actual and flow-affected spectra.

How are these effects manifested in actual spectral diagnostics? Unfortunately, the affect can be devastating. In Fig. 8, a plot of the plasma electron temperature with Z is shown; both the hydrocode profile and spot spectroscopy diagnosis are shown (for the long density scalelength case). The characteristic signature of convective flow effects on the spatially-resolved spectra is evident: underestimates of the temperature

near the target (where plasma upstream is cooler) and overestimates of the temperature far from the target (where the upstream plasma is hotter). For shorter scalelength plasmas the errors are expected to be significantly larger than those shown in Fig. 8. This is a very disappointing result from the standpoint of the spectroscopist since it implies that tracer-dot analysis no longer depends on only the experimental data and an ionization/radiation model, but the diagnoses is linked to a hydrodynamic simulation in order to predict the effect of the plasma flow. One would like to benchmark or verify the validity of hydro models by using spot spectroscopy techniques; now that the results are presumably tied with the hydrocode predictions absolute verification is a bit more questionable via the technique.

It would be very helpful to develop a method by which the flow problem is eliminated since it will manifest itself not only with tracer dots but in any spectroscopic analysis where the emission is detected perpendicular to the flow, whether it be low concentration tracer material doped in targets or just straightforward spatially-resolved full-target spectroscopy. Are there any ways to avoid the convection effects? One idea we are presently pursuing at NRL is to investigate using only diagnostic indicators from the same ionization stage. This would, in principle, eliminate non-equilibrium ionization effects caused by either explicit or flow-velocity time dependence, since the atomic collisional rates populating levels within a single stage of ionization are usually much faster than either the rates between ionization stages or the hydrodynamic time scales. If this proves to be a valid assumption, plasma temperature could be determined via dielectronic satellite line ratios as opposed to the present method of comparing hydrogenic and heliumlike resonance lines. (A recent paper²⁷ describes the numerous diagnostic indicators possible using satellites in dense plasmas.) Although the plasma density is presently determined by lines from the same stage of ionization (the resonance-to-intercombination line intensity ratio in the heliumlike system), errors infiltrate the measurement since temperature is required in order to determine density. Thus, if bogus temperatures are obtained from, for example, the $H-\alpha/He-\alpha$ line ratio, they will disturb the density measurement. If an alternative temperature diagnostic is used which makes accurate predictions, unaffected by flow velocity, then

accurate density measurements can also be assured. These concepts are presently under study at NRL and the results will be made available in a forth coming report.

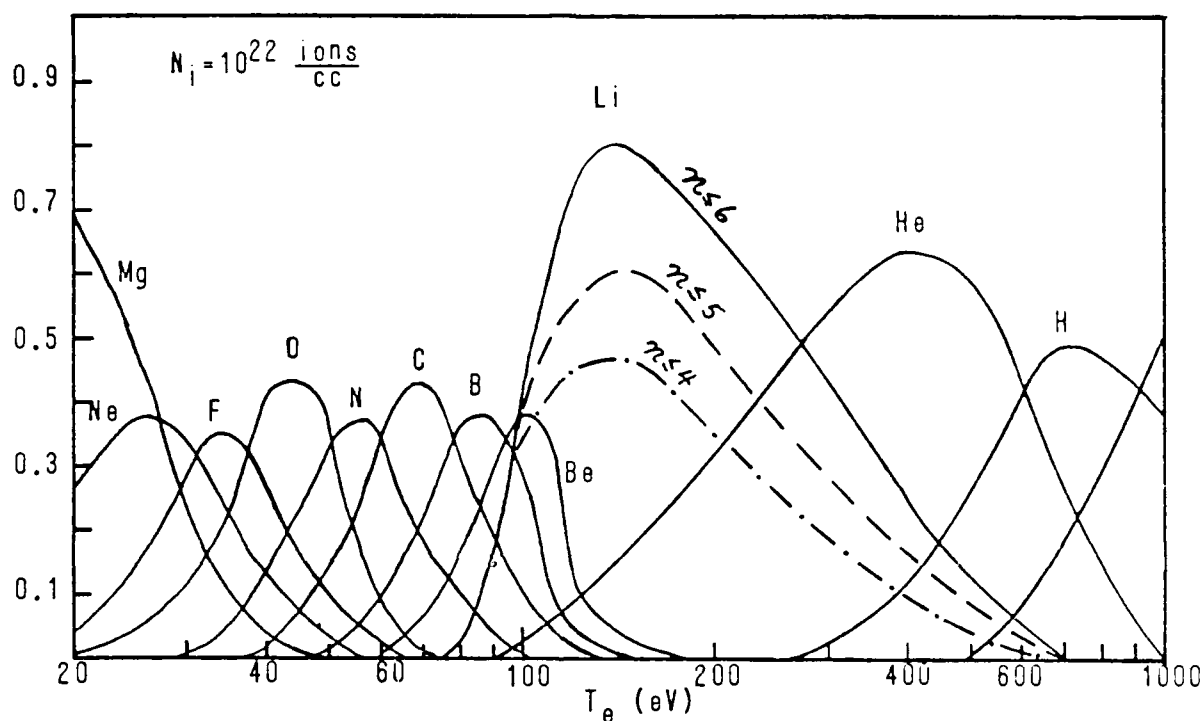


Fig. 1. Fractional ion abundances (including excited states) of an aluminum plasma, optically thin, at $10^{22} \text{ ions/cm}^3$, calculated with the CRE model. The effect of changing the number of excited levels in the lithiumlike ion is shown for the $A_{\lambda} \text{ XI}$ abundance only.

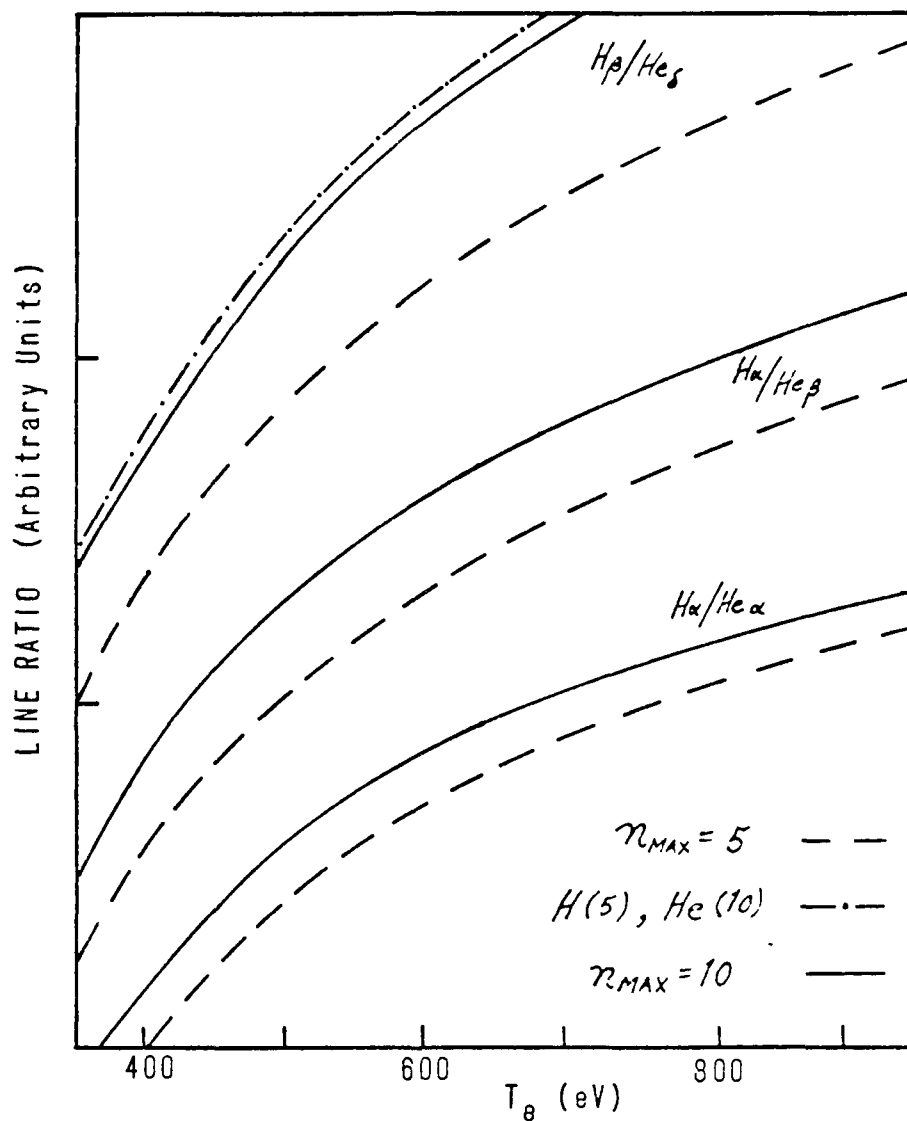


Fig. 2 Hydrogenlike-to-heliumlike line intensity ratios for a 10^{20} ion/cm³ aluminum plasma in cylindrical geometry (diameter = 115 μ m), calculated with the CRE model. Solid curves are for $n \leq 10$ for both ions; dashed curves are for $n \leq 5$ for both ions; alternating dots and dashes are for $n \leq 10$ in Al XII and $n \leq 5$ in Al XIII.

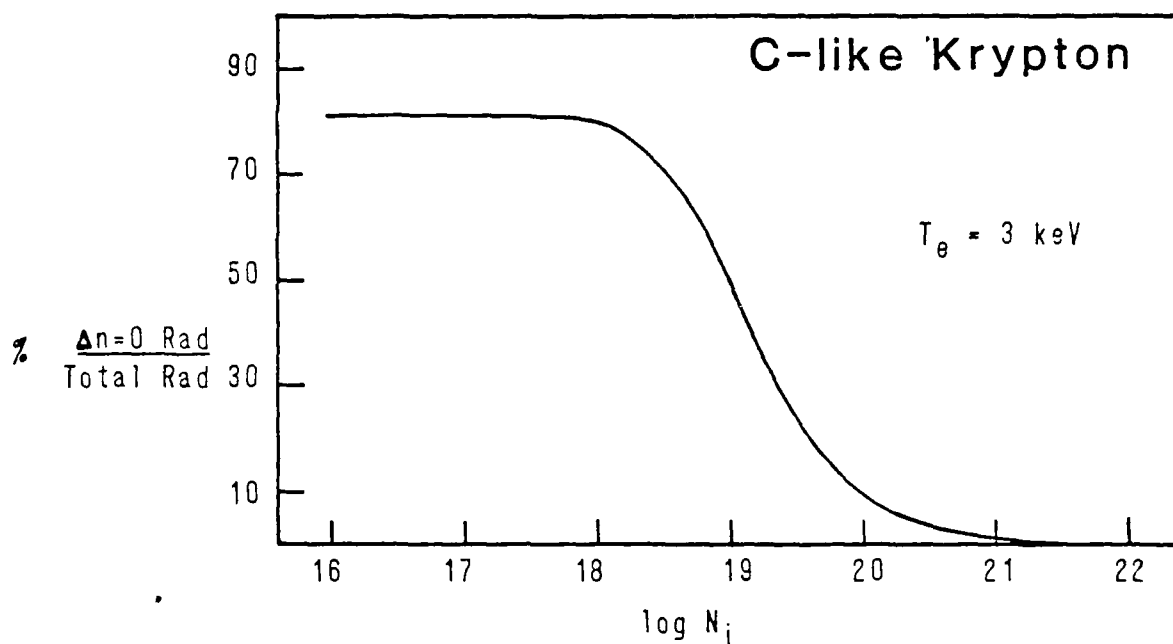


Fig. 3 Radiation due to $\Delta n = 0$ transitions for carbonlike krypton as compared to the total Kr XXXI line emission for various ion densities; electron temperature is constant at 3 keV.

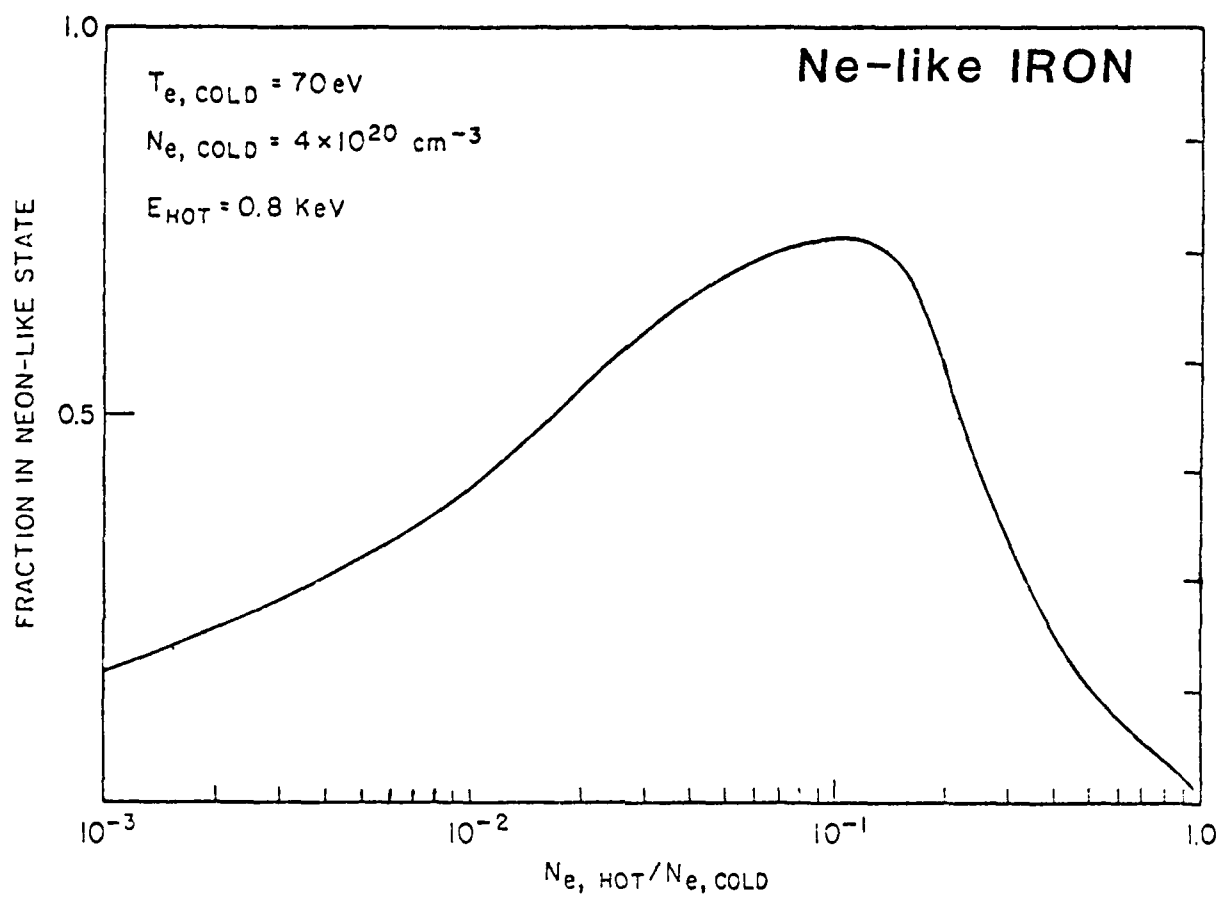


Fig. 4 The fractional ion abundance of neonlike ion as a function of the ratio of hot electron density to cold electron density (T_e (cold) = 70 eV, T_e (hot) = 800 eV, N_e (cold) = $4 \times 10^{20} \text{ cm}^3$).

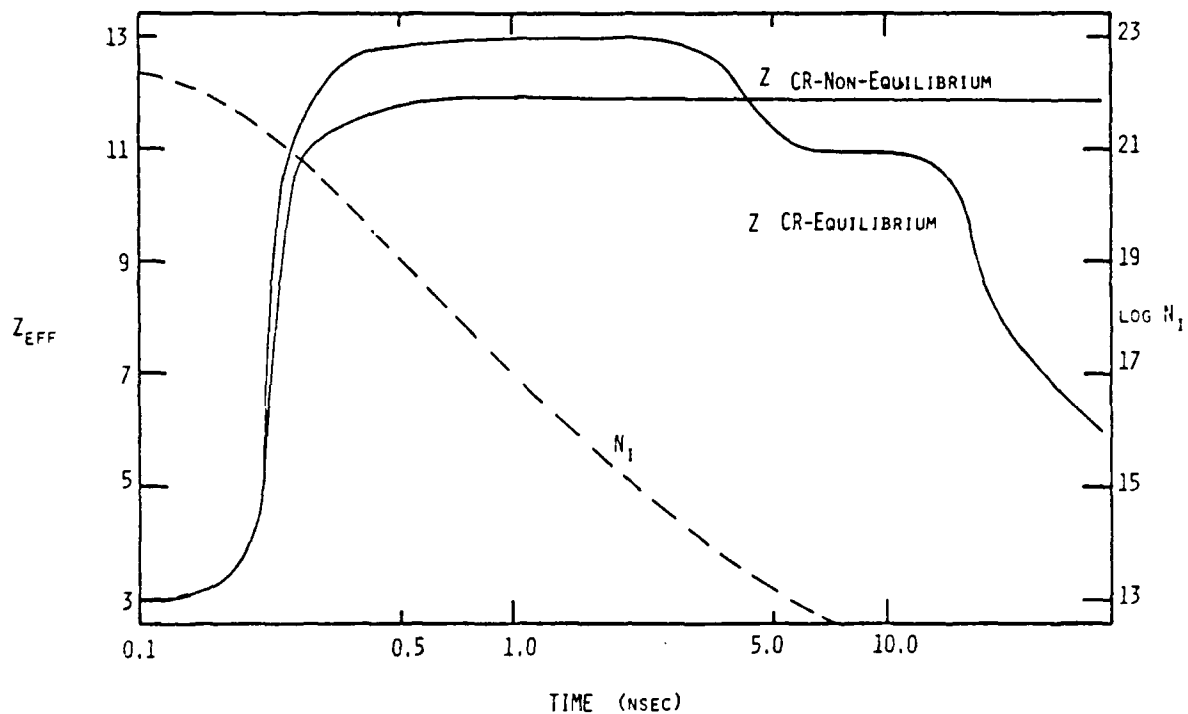


Fig. 5 The Z_{eff} of a zone in a CO_2 laser-heated aluminum foil simulation as a function of time, comparing equilibrium CRE and time-dependent CR model predictions, also shown is the plasma ion density.

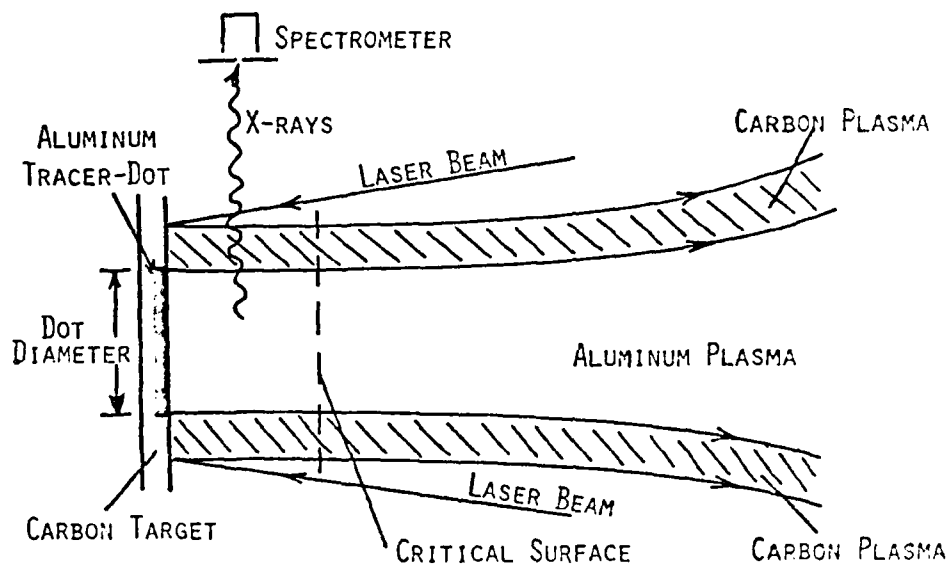
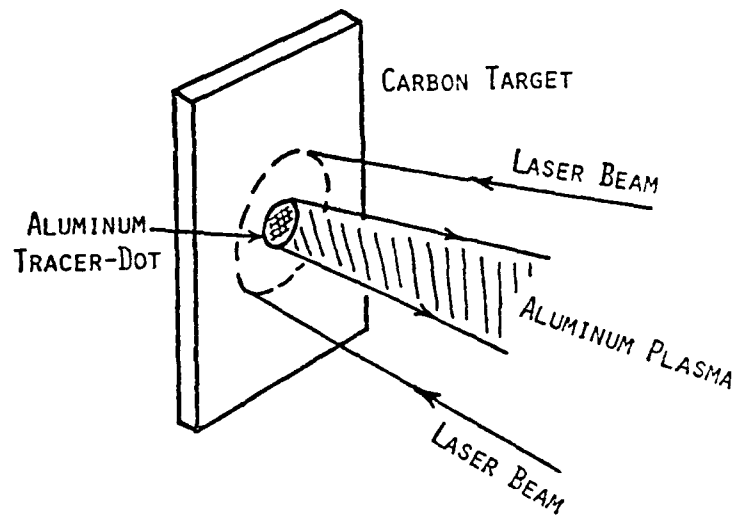


Fig. 6 Schematic of the tracer-dot spectroscopy technique for obtaining laser-plasma T_e and N_I profiles.

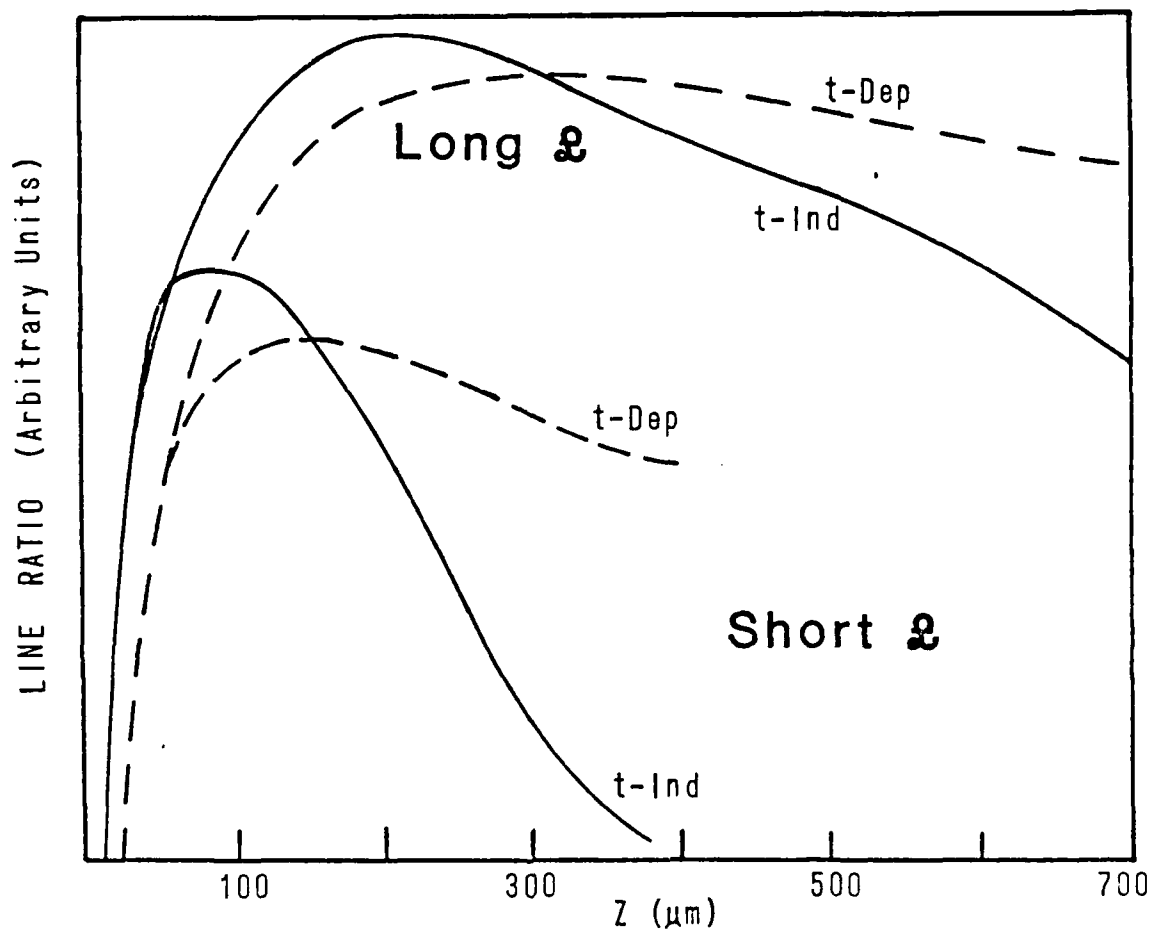


Fig. 7 The H- α /He- α line ratios as a function of distance, z , from a laser-heated target containing an aluminum tracer-dot implant. Ratios of line intensities generated by actual localized equilibrium temperatures and densities (solid lines) and ratios reflecting actual intensities (affected by flow velocity) that would be experimentally measured (dashed lines) are shown. Both a long and short density scalelength case are given.

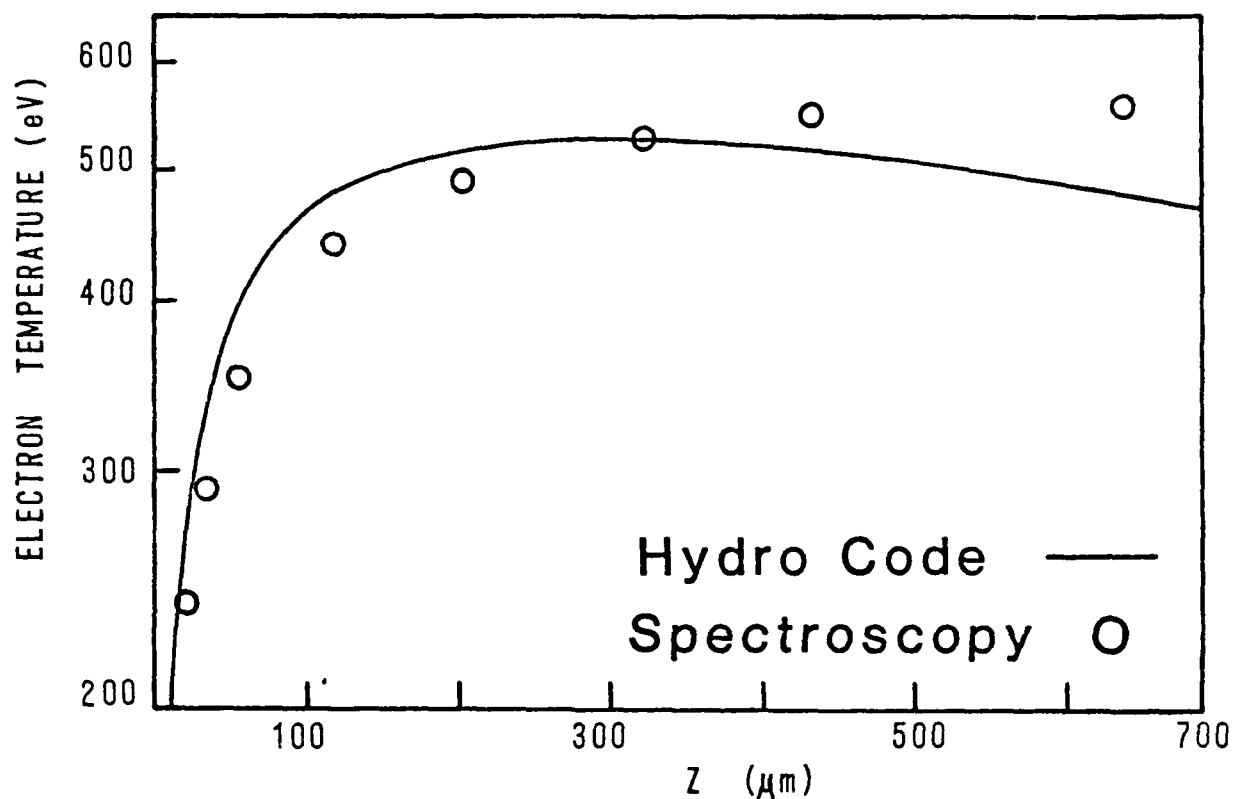


Fig. 8 The electron temperature in a long scalelength laser-plasma as predicted by tracer-dot spectroscopy of a 115 μm -diameter aluminum implant. Also shown are those calculated by the FAST2D hydrodynamic code.

Dense plasma effects on *K*-shell dielectronic satellite lines

D. Duston, J. E. Rogerson, J. Davis, and M. Blaha*

Plasma Radiation Branch, Plasma Physics Division, U.S. Naval Research Laboratory, Washington, D.C. 20375

(Received 1 June 1983)

The dielectronic satellite lines from the $n=2$ doubly excited levels of lithiumlike and heliumlike ions have been studied theoretically in dense-plasma environments. A comprehensive level structure including ground, singly excited, and doubly excited levels was included in a collisional-radiative equilibrium model to calculate level populations and the satellite intensities self-consistently for carbon, aluminum, and argon plasmas. The effects of inner-shell excitation rates (calculated via the distorted-wave approximation with configuration mixing) and collisional ionization and recombination of the doubly excited levels are included in the model and their effects on the satellite intensities assessed. The well-known heliumlike intercombination-to-resonance line ratio, used in density determinations, is shown to be strongly affected by blended satellite lines at high density, causing significant error in the measured density when their intensities are not accounted for.

I. INTRODUCTION

Dielectronic satellite lines result from the spontaneous radiative decay of doubly excited levels of atoms and ions, usually appearing in the radiation spectrum as less-intense features adjacent to resonance lines of the ion with the next-highest charge state. In particular, a subset of this general family of lines, due to transitions of the type $1s2l-2l'2l'$ and $1s^22l-1s2l'2l'$, have received much attention due to their value as plasma diagnostic indicators. These lines are often prominent features in the *K*-shell spectra of high-temperature plasmas and lie slightly to the long-wavelength side of the hydrogenlike Lyman- α and heliumlike resonance lines. Much effort in plasma spectroscopy has been devoted to their detection, classification, measurement, and diagnosis.

The first laboratory observation of these lines was by Edlén and Tyren,¹ but more recently, a number of laboratory observations have been reported on.²⁻⁷ The importance of these satellite lines in astrophysical plasmas was first pointed out by Gabriel and Jordan,⁴ who presented a detailed classification of the lithiumlike satellites in that study, while the line intensities and population mechanisms were described in more detail and calculations improved in later papers.⁹⁻¹¹ Observations of both heliumlike and lithiumlike satellites in solar spectra were reported by a number of workers,¹²⁻¹⁶ while further laboratory studies were done with vacuum sparks¹⁷ and laser-produced plasmas.¹⁸⁻²⁰ The effects of plasma microfields on autoionization rates and profiles of heliumlike satellite lines was first described by Davis and Jacobs,²¹ while high-density collisional effects were first pointed out by Weisheit²² and later developed into a density diagnostic for laser-produced plasmas by workers in the Soviet Union.²³⁻²⁷ Seely, Lunney, and co-workers²⁸⁻³¹ extended the technique to compressed laser-fusion microballoon tar-

gets, while Duston and Davis³² showed that opacity effects could alter density determinations in inertially confined plasmas. Meanwhile, lithiumlike satellites were the subject of continued studies: The effects of non-Maxwellian electron distributions on satellite intensities were investigated by Gabriel and Philips,³³ density effects were seen in vacuum spark spectra by Kononov and co-workers,³⁴ Bely-Dubau *et al.*³⁵⁻³⁹ extended calculations to $1s^2nl-1s2l'nl$ -type configurations with $n \geq 3$, Bitter *et al.*,³⁹⁻⁴¹ the TFR group⁴² and Källne *et al.*⁴³⁻⁴⁵ observed detailed satellite structure in tokamaks, Datla *et al.*⁴⁶ determined electron temperature in a neon-filled θ pinch, and Jacobs and Blaha⁴⁷ calculated the effects of collisions between doubly excited levels on the satellite intensities. Armour *et al.*⁴⁸ and Boiko *et al.*⁴⁹ have reported on comprehensive satellite line observation and classification in beam-foil excited spectra and laser plasmas, respectively.

The purpose of this study is to continue the work begun by Jacobs and Blaha⁴⁷ of describing satellite line behavior in dense plasmas by including electron collisional effects explicitly. However, we extend the complexity of their model by solving for the doubly-excited-state population densities and satellite line intensities self-consistently with singly-excited-state densities and resonance and intercombination line intensities. The details of the model, described in Sec. II, include ionization dynamics, level structure, and rate coefficient calculations. The behavior of the heliumlike and lithiumlike satellite lines as a function of plasma density and temperature is studied in Sec. III, including discussions of several diagnostic line intensity ratios. In order to allow comparisons of the satellite lines as a function of atomic number Z , the calculations are performed for high-density carbon, aluminum, and argon plasmas. Because of the magnitude of this subject, we have limited the scope of this paper to include only optically thin plasmas. The effects of photon self-absorption on the satellite line intensities will be investigated in a future paper.

II. THEORETICAL MODEL

The method used to investigate the behavior of the dielectronic satellite lines is based on a completely self-consistent collisional-radiative equilibrium (CRE)⁵⁰ calculation. Rate equations of the form

$$\frac{dN_i}{dt} = \sum_j W_{ji} N_j - \sum_j W_{ij} N_i \quad (1)$$

are solved for each atomic energy level included in the model for an equilibrium plasma [i.e., the left-hand side of Eq. (1) is set equal to zero], with N_i as the population density for level i and W_{ij} representing the total transition rate from level i to level j . The rate coefficients, W_{ij} , are, in general, functions of the plasma density, temperature, and local photon field, and are discussed in detail below. The equations are solved independent of a fluid description of the plasma motion; thus, the density, temperature, and plasma size are the independent variables. Once the set of population densities has been calculated, the individual line and continuum intensities can be determined and a theoretical radiation spectrum calculated.

A. Energy levels

In order to accurately assess the effect of varying Z on the satellite intensities, the identical level structure was used for all three materials studied. All ground states were included in addition to the $n=2-4$ levels of the hydrogenlike ion, the $1s2s^1S$, $1s2p^3P$, $1s2s^1S$, $1s2p^1P$, $n=3$ triplet, $n=3$ singlet, $n=4$, $n=5$, $2s^2^1S$, $2s2p^3P$, $2p^2^3P$, $2p^2^1D$, $2s2p^1P$, and $2p^2^1S$ levels of the heliumlike ion and the $1s^22p$, $1s^23s$, $1s^23p$, $1s^23d$, $n=4$, $n=5$, $1s2s^2S$, $1s2s(^1P)2p^2P$, $1s2s(^3P)2p^2P$, $1s2p^2^2D$, $1s2p^2^2P$, and $1s2p^2^2S$ levels of the lithiumlike ion. At the densities of interest in this study, ion-ion collisions^{51,52} should force individual j components of a single nl level into statistical equilibrium with one another, hence, only nl levels (or, in cases of high- n , only n levels) are treated in the model for the purposes of collisional couplings. In order to treat individual satellite line components from j levels, however, the radiative couplings between doubly and singly excited levels are calculated as individual j components. While the individual radiative decay rates are still averaged over j to obtain the nl -level transition rate, this scheme allows us to accurately represent the individual satellite line intensities. The energies of the levels included in our atomic model were calculated using the relativistic Hartree-Fock atomic structure code provided by Cowan.⁵³

B. Collisional couplings

The rate coefficients employed in this calculation were obtained by a number of methods. All levels of ion Z were coupled to the ground state of ion $Z+1$ by collisional ionization (exchange classical impact parameter method⁵⁴) photoionization (hydrogenic approximation⁵⁵ with Karzas-Latter Gaunt factors⁵⁶), and collisional and radiative recombination (the detailed balance of the above rate coefficients). Adjacent ions were coupled by dielectronic recombination, with rate coefficients provided by

Jacobs and Davis.⁵⁷ All dipole-allowed and some important forbidden radiative transitions were coupled by spontaneous radiative decay. The oscillator strengths and Einstein A coefficients were also calculated using Cowan's structure code, as were the autoionization rates for the doubly excited levels. The autoionization and radiation rates calculated for this study have been compared with those calculated by Vainshtein and Safranov.⁵⁸ In fact, due to the widespread use this comprehensive set of dielectronic satellite data has had, we not only compared the actual data, but, in addition, used their data for preliminary satellite line intensity studies while the new data set was being generated for the present calculations. Comparison of the two sets of values for wavelengths of the satellites and the spontaneous decay rates showed very little difference, typically less than 0.1% and 10%, respectively, for all three of the materials investigated. The values generated by Cowan's structure code for autoionization, however, differed by typically 50–100% for most transitions, but varied by as much as a factor of 3 in some cases. The largest differences occurred in carbon, the smallest in argon. However, more importantly, we were interested in what effects these differences would have on the diagnostics. It was found that, in most cases, little or no change occurred in the satellite line intensities when one set of data was replaced by the other. The largest differences were on the order of 10–20%, but these discrepancies were manifested in only 3 of the 12 satellite line blends studied; all others experienced less than 10% changes. Thus, differences in a plasma temperature or density determination could be expected to be of the same order using the two sets of data. Since the bound-state and continuum wave functions calculated using Cowan's model represent a distinct improvement over the Coulomb-Born wave functions used by Vainshtein and Safranov [the approximate nature of their autoionization rates is, in fact, acknowledged and stated by the authors], we have chosen to use the more recently calculated data in our study. The reader is cautioned, however, that the differences quoted here result from comparisons performed in a dense-plasma environment; the discrepancies may well be amplified at lower densities where the plasma approaches a more coronal state and autoionization plays a more instrumental role in determining doubly excited level populations.

The ground states of the hydrogenlike and heliumlike ions were coupled to their appropriate doubly excited levels by electron capture; the rate coefficients for this process were obtained by detailed balance of the autoionization rates (the opposite process). The doubly excited levels were coupled to the $n=2$ levels of the next-highest ion by collisional ionization and recombination using the same methods stated earlier. Although these processes are not thought to be important until very high densities, we sought to quantify their effect and, therefore, included them in the model. Singly excited levels were coupled to ground states and also to each other via electron impact excitation [the Coulomb-Born distorted-wave (DW)⁵⁹ code of Blaha was used]. However, for coupling the $1s^2$, $1s2s$, and $1s2p$ levels of the heliumlike ion, the more accurate rates by Pradhan *et al.*,⁶⁰ which include the effects of au-

ionizing resonances, were used. Finally, doubly excited levels of a given ion were coupled to each other and to singly excited levels by electron impact excitation and deexcitation. The calculation of these coefficients is treated in detail in Sec. II C.

C. Inner-shell and cross-coupling transitions

In addition to electron capture and collisional recombination, the doubly excited levels can be populated by inner-shell electron impact excitation of an $n=1$ electron of the lithiumlike and heliumlike ions. For some states, this process is the dominant populating mechanism. The rate coefficients for these transitions were calculated in the following way. After the energy levels had been determined, electron impact cross sections were generated between the various LS terms using the DW code. In these calculations, the relativistic Hartree-Fock radial wave functions generated by the atomic structure code were used to describe the bound electrons while the continuum electronic states were represented by distorted wave functions which take into account the non-Coulombic electrostatic interaction. Since the plasma electrons will have energies of the order of the threshold excitation energies of these inner-shell transitions for the parameters of interest in this study, electron exchange effects were included in the cross-section calculations.

Since the threshold transition energies between doubly excited levels are typically 2 orders of magnitude smaller than electron energies at the plasma temperatures of interest here, exchange effects were not included in the calculation of the cross-coupling cross sections between doubly excited levels. However, it was necessary to calculate the cross sections at these very high electron energies. In general, it is not practical to do the summation over all the angular momenta required to evaluate the collision strengths Ω at these high energies. Therefore, the collision strength was usually calculated fully up to some large value of electron energy E (typically 20 times threshold) and extrapolated to higher values of E . For dipole transitions the Bethe approximation⁶¹ was used, while it was assumed that Ω varied as E^{-2} for transitions involving a change of spin. For quadrupole transitions, Ω should approach a constant value as E becomes very large, however, this limit is approached computationally with considerable effort and expense due to the large number of angular momentum terms required for convergence. Hence, nondipole, non-spin-change transitions were plotted to examine high- E behavior and were extrapolated accordingly.

Configuration and term mixing of the various energy levels and transitions were included in the collision strength calculations using the methods described by Jacobs and Blaha.⁴⁷ The mixing coefficients were taken from Cowan's structure code. Rate coefficients were then calculated by thermally averaging the collision strengths over a Maxwellian distribution.

Shown in Fig. 1 are the inner-shell collisional excitation rate coefficients for lithiumlike AlXI versus electron temperature, while those for heliumlike AlXII are shown in Fig. 2. As was expected, the AlXI results reproduced very

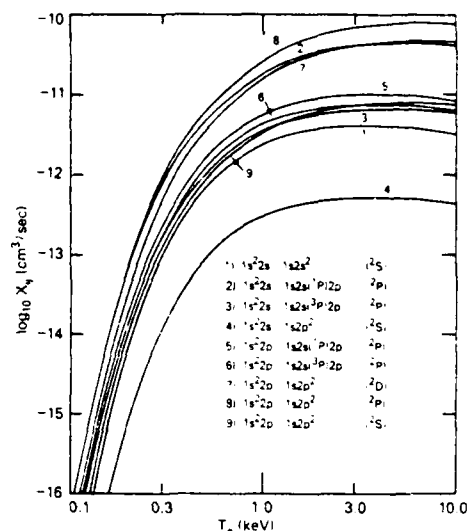


FIG. 1. Inner-shell electron impact excitation rate coefficients for singly to doubly excited levels of the lithiumlike AlXI ion vs electron temperature.

well the calculations of Jacobs and Blaha. The difference between the present calculation and theirs is that they used the bound-state wave functions of Clementi and Roetti.⁶² However, these wave functions were found to be virtually identical to the Hartree-Fock wave functions generated by Cowan's structure code. The lithiumlike ion cross-coupling excitation rate coefficients for AlXI are shown in Fig. 3; the key to the transitions is in Table I. As was stated earlier, the plasma temperatures of interest

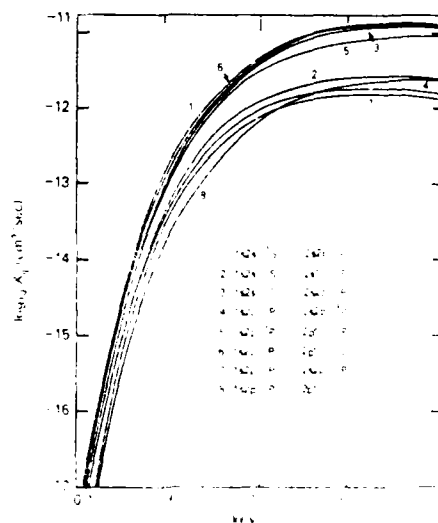


FIG. 2. Inner-shell electron impact excitation rate coefficients for singly to doubly excited levels of the heliumlike AlXII ion vs electron temperature.

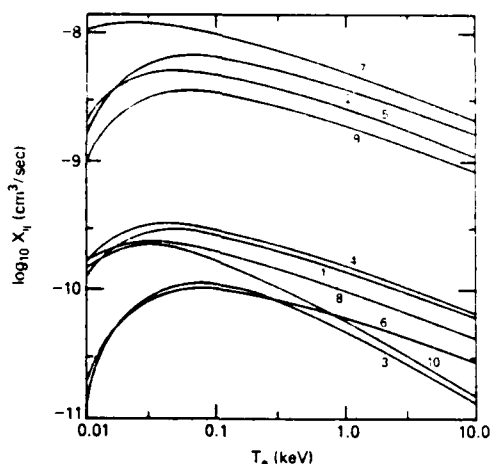


FIG. 3. Cross-coupling electron impact excitation rate coefficients between doubly excited levels of the lithiumlike Al XI ion vs electron temperature.

here (typically above 200 eV for aluminum, where Al XI is expected to be abundant) are well above threshold energies for these transitions; this can be seen clearly in Fig. 3.

The collision strengths for the heliumlike ion cross-coupling transitions versus electron energy (in units of $E/\Delta E$, where ΔE is the threshold energy) are shown in Fig. 4 for carbon and Fig. 5 for argon; the key to the transitions is in Table II. Also shown as dashed curves in Figs. 4 and 5 are the calculations of Goett, Sampson, and Clark,⁶³ and good agreement between their results and the present calculation is evident for most transitions shown. Their results for Ω were generated using hydrogenic atomic wave functions for the bound electrons and Coulomb functions for the free electrons, with Z^2 scaling and in intermediate coupling.⁶⁴ In particular, the $2s^2(^1S)$ and $2p^2(^1S)$ levels are strongly coupled in the Ar XVII system, and the mixing must be included in the calculation of Ω . The effects of mixing as a function of Z can clearly be seen by comparing, for example, the $2p^2(^3P)-2s2p(^1P)$ collision strengths in Figs. 4 and 5; the behavior of Ω vs

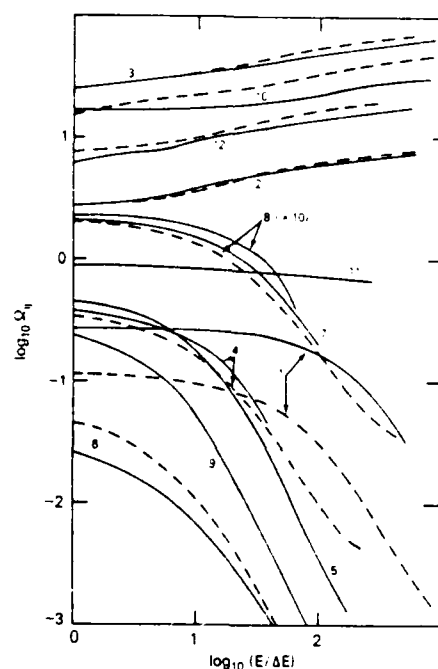


FIG. 4. Cross-coupling electron impact collision strengths between doubly excited levels of the heliumlike C V ion vs incident electron energy (in threshold energy units)

TABLE I. Transitions among the lithiumlike doubly excited states corresponding to the electron impact excitation rate coefficients shown in Fig. 3.

Key	Transition
1	$1s2s^2S-1s2s(^1P)2p^2P$
2	$1s2s^2S-1s2s(^1P)2p^2P$
3	$1s2s^2S-1s2p^2D$
4	$1s2s(^1P)2p^2P-1s2p^2D$
5	$1s2s(^1P)2p^2P-1s2p^2P$
6	$1s2s(^1P)2p^2P-1s2p^2S$
7	$1s2s(^1P)2p^2P-1s2p^2D$
8	$1s2s(^1P)2p^2P-1s2p^2P$
9	$1s2s(^1P)2p^2P-1s2p^2S$
10	$1s2p^2D-1s2p^2S$

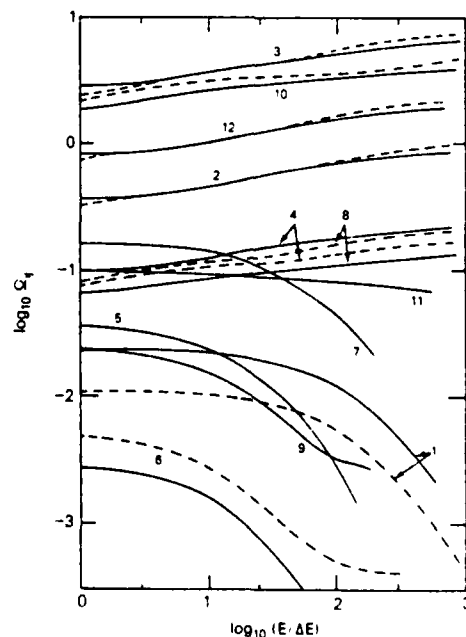


FIG. 5. Cross-coupling electron impact collision strengths between doubly excited levels of the heliumlike Ar XVII ion vs incident electron energy (in threshold energy units)

TABLE II. Transitions among the heliumlike doubly excited levels corresponding to the electron impact collision strengths shown in Figs. 4 and 5.

Key	Transition
1	$2s^2\ ^1S-2s\ 2p\ ^1P$
2	$2s^2\ ^1S-2s\ 2p\ ^3P$
3	$2s\ 2p\ ^1P-2p^2\ ^1P$
4	$2s\ 2p\ ^1P-2p^2\ ^1D$
5	$2s\ 2p\ ^1P-2s\ 2p\ ^1P$
6	$2s\ 2p\ ^1P-2p^2\ ^1S$
7	$2p^2\ ^1P-2p^2\ ^1D$
8	$2p^2\ ^1P-2s\ 2p\ ^1P$
9	$2p^2\ ^1P-2p^2\ ^1S$
10	$2p^2\ ^1D-2s\ 2p\ ^1P$
11	$2p^2\ ^1D-2p^2\ ^1S$
12	$2s\ 2p\ ^1P-2p^2\ ^1S$

$E/\Delta E$ is totally different for argon and carbon. No comparison of transitions between similar electron configurations ($2l2l'-2l2l'$) is shown since the Coulomb-Born method of Goett *et al.* did not treat this type of transition.

D. Dielectronic satellite lines

As discussed earlier, the doubly excited levels for lithiumlike and heliumlike ions give rise to a large number of satellite lines via dipole-allowed radiative transitions to singly excited levels. These lines are represented schematically in Fig. 6 (lithiumlike lines) and Fig. 7 (heliumlike lines). For classifying the lithiumlike satellites, we use the well-known letter designation, first introduced by Gabriel.¹⁰ For the heliumlike satellites, we use a simple numbering scheme to define the lines. A complete listing of the satellite line transitions, designations, theoretical wavelengths, and radiative decay and autoionization rates used in this study is given in Table III for carbon, aluminum, and argon.

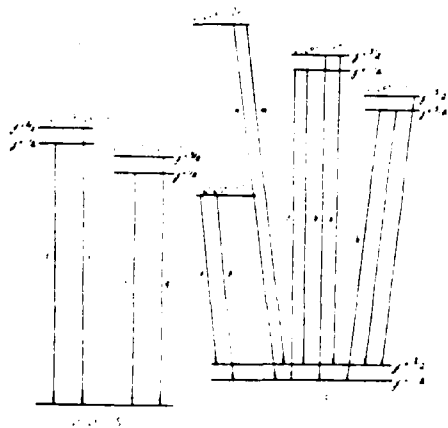


FIG. 6. Schematic of the excited level system of the lithiumlike ion which gives rise to the $n=2$ dielectronic satellite lines adjacent to the heliumlike resonance line.

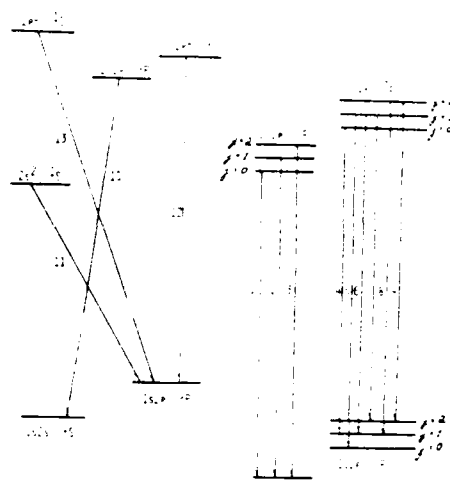


FIG. 7. Schematic of the excited level system of the heliumlike ion which gives rise to the $n=2$ dielectronic satellite lines adjacent to the hydrogenlike resonance line.

num, and argon. In order to allow visualization of typical satellite line spectra, theoretical carbon, aluminum, and argon K -shell spectra in the region of the hydrogenlike and heliumlike resonance lines are shown in Fig. 8. The resonance lines have been truncated to show the detailed structure of the satellite lines. Worth noting is the relative shift in several of the lines with increased Z , such that lines from different electron configurations overlap or become blended as a result of various line or source broadening mechanisms. Note also, the proximity of several of the satellites (m, n, s, t) to the $1s^2-1s\ 2p\ ^3P$ intercombination (IC) line, such that they can appear as almost a single blended line (particularly at high plasma densities, where lines are collisionally broadened). It will be shown later that this can have significant impact on density diagnostics in laser-produced and inertially confined plasmas.

III. RESULTS

The main emphasis in this section will be on the behavior of the $n=2$ dielectronic satellites as a function of plasma density and temperature. As stated earlier, all investigations presented here assume an optically thin plasma, calculated by ignoring the effects of opacity in our CRE model (more detailed discussion of the theoretical ionization-radiation model can be found elsewhere^{65,66}). A detailed study of opacity effects on satellite lines will be presented in another paper to follow.

A. Ion population distributions

Prior to discussion of the satellite line intensities, it may prove useful to present the ion population abundances in the parameter range of interest to this work. This will allow later reference to the relative populations of the ions when explaining the effects of individual collisional pro-

TABLE III. List of transitions, satellite line key, wavelengths, radiative decay rates, and autoionization rates for the satellite lines included in this study. (Numbers in parentheses denote power of 10.)

Transition	Key	Carbon			Aluminum			Argon		
		λ (Å)	A (sec ⁻¹)	Γ (sec ⁻¹)	λ (Å)	A (sec ⁻¹)	Γ (sec ⁻¹)	λ (Å)	A (sec ⁻¹)	Γ (sec ⁻¹)
$1s^2 2s^2 S_{1/2} - 1s 2s (1P) 2p^2 P_{1/2}$	r	41.394	8.46(11)	6.00(12)	7.8496	2.56(13)	7.72(12)	3.9839	8.88(13)	1.28(13)
$1s^2 2s^2 S_{1/2} - 1s 2s (1P) 2p^2 P_{3/2}$	q	41.392	8.49(11)	5.81(12)	7.8475	2.61(13)	4.37(12)	3.9816	1.05(14)	2.40(12)
$1s^2 2s^2 S_{1/2} - 1s 2s (1P) 2p^2 P_{1/2}$	t	40.860	9.04(10)	4.80(13)	7.8097	3.68(12)	7.31(13)	3.9692	2.30(13)	7.23(13)
$1s^2 2s^2 S_{1/2} - 1s 2s (1P) 2p^2 P_{3/2}$	s	40.859	8.78(10)	4.81(13)	7.8085	2.28(12)	7.64(13)	3.9681	6.29(12)	8.27(13)
$1s^2 2p^2 P_{1/2} - 1s 2s^2 S_{1/2}$	p	43.684	2.09(10)	7.14(13)	8.0694	9.54(11)	1.04(14)	4.0660	1.98(12)	1.08(14)
$1s^2 2p^2 P_{3/2} - 1s 2s^2 S_{1/2}$	o	43.686	4.16(10)	7.14(13)	8.0732	4.77(11)	1.04(14)	4.0703	3.13(12)	1.08(14)
$1s^2 2p^2 P_{1/2} - 1s 2p^2 D_{1/2}$	k	41.483	3.62(11)	7.12(13)	7.8683	1.37(13)	1.15(14)	3.9892	6.33(13)	1.16(14)
$1s^2 2p^2 P_{3/2} - 1s 2p^2 D_{3/2}$	l	41.484	5.46(10)	7.12(13)	7.8719	3.96(11)	1.15(14)	3.9932	5.29(13)	1.16(14)
$1s^2 2p^2 P_{1/2} - 1s 2p^2 D_{3/2}$	j	41.485	4.15(11)	7.12(13)	7.8715	1.34(13)	1.17(14)	3.9923	3.51(11)	1.25(14)
$1s^2 2p^2 P_{3/2} - 1s 2p^2 D_{3/2}$	a	41.425	1.16(12)	3.30(10)	7.8573	3.71(13)	2.10(12)	3.9854	1.48(14)	1.00(13)
$1s^2 2p^2 P_{1/2} - 1s 2p^2 P_{1/2}$	b	41.424	2.13(11)	3.30(10)	7.8538	4.61(13)	2.10(12)	3.9814	9.54(12)	1.00(13)
$1s^2 2p^2 P_{3/2} - 1s 2p^2 P_{1/2}$	c	41.428	4.56(11)		7.8609	1.32(13)	1.80(10)	3.9897	4.60(13)	1.56(11)
$1s^2 2p^2 P_{1/2} - 1s 2p^2 P_{1/2}$	d	41.426	9.17(11)		7.8574	2.90(13)	1.80(10)	3.9856	1.19(14)	1.56(11)
$1s^2 2p^2 P_{1/2} - 1s 2p^2 S_{1/2}$	n	40.736	1.41(11)	9.77(12)	7.7987	3.47(12)	1.81(13)	3.9631	8.63(12)	2.04(13)
$1s^2 2p^2 P_{3/2} - 1s 2p^2 S_{1/2}$	m	40.738	2.88(11)	9.77(12)	7.8022	9.65(12)	1.81(13)	3.9671	4.45(13)	2.04(13)
$1s 2s^2 S_1 - 2s 2p^3 P_0$	1	34.525	7.41(11)	9.12(12)	7.2487	1.73(12)	1.19(13)	3.7652	6.41(13)	1.16(13)
$1s 2s^2 S_1 - 2s 2p^3 P_1$	2	34.523	7.41(11)	9.12(12)	7.2521	1.72(12)	1.20(13)	3.7637	6.58(13)	1.24(13)
$1s 2s^2 S_1 - 2s 2p^3 P_2$	3	34.520	7.41(11)	9.12(12)	7.2537	1.72(12)	1.19(13)	3.7661	6.44(13)	1.16(13)
$1s 2p^3 P_1 - 2p^2 P_0$	4	34.594	1.42(12)	1.00(9)	7.2605	3.39(13)	1.57(11)	3.7668	1.25(14)	9.09(11)
$1s 2p^3 P_0 - 2p^2 P_1$	5	34.591	4.77(11)		7.2575	1.14(13)		3.7636	4.25(13)	
$1s 2p^3 P_1 - 2p^2 P_1$	6	34.592	3.58(11)		7.2587	8.49(12)		3.7649	3.14(13)	
$1s 2p^3 P_2 - 2p^2 P_1$	7	34.594	5.96(11)		7.2618	1.42(13)		3.7682	5.29(13)	
$1s 2p^3 P_1 - 2p^2 P_2$	8	34.589	3.58(11)	1.10(10)	7.2558	8.58(12)	2.08(12)	3.7621	3.33(13)	1.64(13)
$1s 2p^3 P_2 - 2p^2 P_2$	9	34.591	1.07(12)	1.10(10)	7.2588	2.53(13)	2.08(12)	3.7655	8.98(13)	1.64(13)
$1s 2s^2 S_0 - 2s 2p^3 P_1$	10	34.283	7.50(11)	9.61(13)	7.2284	1.72(13)	1.51(14)	3.7536	6.39(13)	1.53(14)
$1s 2p^3 P_1 - 2s^2 S_0$	11	35.442	3.34(11)	1.65(14)	7.3635	7.66(12)	2.59(14)	3.8088	2.41(13)	2.59(14)
$1s^2 p^3 P_1 - 2p^2 D_2$	12	34.649	1.32(12)	1.62(14)	7.2710	3.24(13)	2.66(14)	3.7699	1.18(14)	2.59(14)
$1s 2p^3 P_1 - 2p^2 S_0$	13	33.973	1.21(12)	7.20(12)	7.1949	2.77(13)	1.26(13)	3.7422	1.06(14)	1.71(13)

cesses on the various satellite intensities. Shown in Fig. 9 are the total (ground plus singly excited states) ion population distributions versus electron temperature for carbon, aluminum, and argon. Only the populations for the lithiumlike, heliumlike, hydrogenlike, and fully-stripped ions are shown, since these are the only ions strongly affecting the satellite lines. The ion density was fixed at 10^{20} ions/cm³ for all these materials; at this density, most of the ionic population still resides in the ground state, with the exception, of course, of the $1s^2 2p$ level of the lithiumlike ion.

B. Satellite intensities versus N_i and T_e

In order to more clearly (and conveniently) present the satellite line dependence on electron temperature (T_e) and total ion density (N_i), the satellite line intensities will be presented normalized to their associated resonance line intensity, i.e., all heliumlike satellite intensities are divided by the $1s^2-1s2p^3P$ (RES) intensity and all hydrogenlike satellites are divided by the $1s-2p$ (Lyman- α) intensity. In Fig. 10, the heliumlike satellite intensities are presented as a function of T_e for an aluminum plasma at 10^{20} ions/cm³. The individual j components have been grouped with other lines from the same nl^2L level since

this is how they normally appear in a high-density-plasma spectrum. The individual j components, however, can often be resolved, at lower densities, e.g., in tokamak or astrophysical plasmas. As the nuclear Z is increased and the LS representation becomes less applicable, j components begin to shift in wavelength, and the groupings shown in Fig. 10 are not convenient in terms of measurable spectral quantities. In argon, for example, we see from Fig. 8 that the groupings (j,l), (r,a,d), (s,t,m), (q,b), (k,c), (o,p), and (n) are more appropriate for experimental purposes. The consistent trend displayed by all the satellites in Fig. 10 of falling off with increasing T_e is due to different factors which depend on the dominant collisional process populating the doubly excited level. The lines (a,b,c,d), (q,r), and (n,m) emanate from doubly excited levels which are populated primarily by inner-shell excitation from lithiumlike levels. As the ratio of AlXII to AlXIII population drops with T_e , so do these satellite intensities. The (j,k,l), (o,p), and (s,t) satellites, on the other hand, come from levels populated by electron capture from the $1s^2$ level.¹ The capture rate coefficient peaks at lower temperature than does the $1s^2-1s2p$ excitation rate coefficient (due to the difference in transition energies), and thus, these satellites also fall off with increasing T_e . From Fig. 10 it is clearly apparent why these line ratios

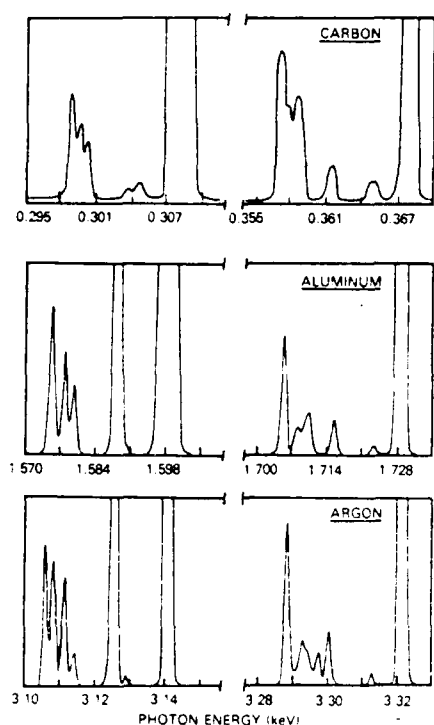


FIG. 8. Theoretical spectra showing the hydrogenlike and heliumlike satellite lines for carbon, aluminum, and argon for typical plasma conditions.

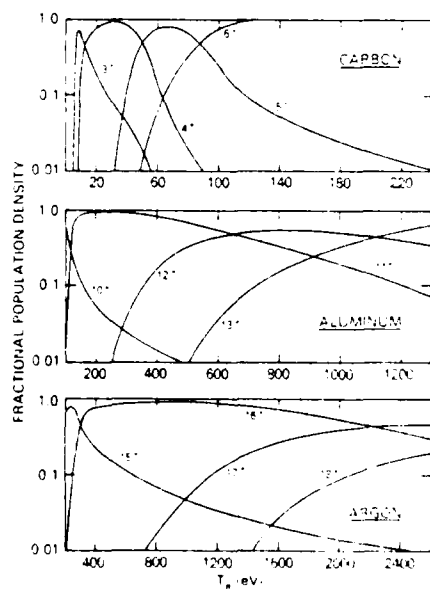


FIG. 9. Ionization abundance curves vs electron temperature for carbon, aluminum, and argon. Plasma density has been fixed at 10^{20} ions/cm³.

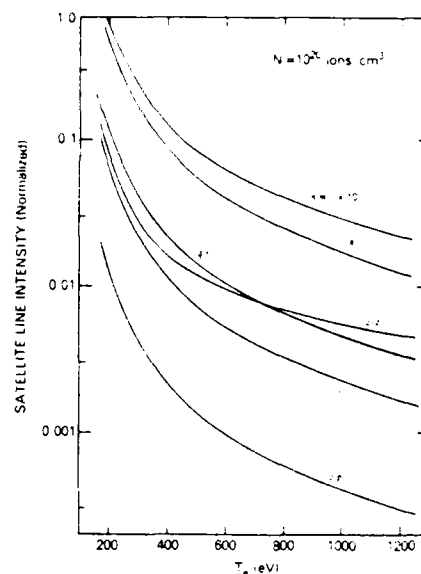


FIG. 10. Heliumlike satellite line intensities, normalized to the resonance line, vs temperature for an aluminum plasma at 10^{20} ions/cm³.

(satellite to RES) are excellent indicators of temperature in the plasma. A good temperature diagnostic, however, is one which is insensitive to density over some range of this parameter.

In Fig. 11, the density behavior of the heliumlike satellite lines is shown for an aluminum plasma at 800 eV. At lower densities, the doubly excited states populated mainly by electron capture give rise to satellites which are somewhat independent of density, while the n, m, l, a, b, c, d , and q, r satellites, for which inner-shell excitation is important, show a distinct drop as the density approaches 10^{20} ions/cm³. It will be shown later that the inner-shell processes become less important in determining satellite

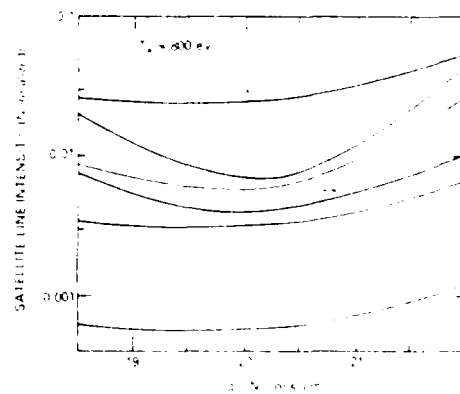


FIG. 11. Heliumlike satellite line intensities, normalized to the resonance line, vs ion density for an aluminum plasma at 800 eV.

intensities as the plasma density increases. All of the satellites display a rise in intensity relative to the resonance line as the density increases from 10^{20} ions/cm³. This is due to the fact that the doubly excited levels are approaching a state of local thermodynamic equilibrium⁶ (LTE) with the $1s^2$ ground state, and the intensities exhibit mild increases from their coronal values.

For the hydrogenlike satellite lines, shown in Fig. 12, a temperature behavior similar to that of the heliumlike satellites is seen. The values for the satellite to Lyman- α ratios shown are for an aluminum plasma at a density of 10^{20} ions/cm³. The line emanating from the $2p^2^1D$ level is the strongest emitter and can be a valuable temperature diagnostic in dense plasmas. As in the figures for the heliumlike satellites, we group the individual lines according to their $n(l^5L)$ upper levels, since an LS representation is still appropriate for Al XII. For argon, however, this is not the case (refer to Fig. 8), as j components from different nL levels are blended in the spectrum. The LS grouping of the $1s2p^3P-2p^2^3P$ and $1s2s^3S-2s2p^3P$ transitions is more easily discernible in the spectrum as the $1s2s^3S-2s2p^3P$ transition, with the six components of the $1s2p^3P-2p^2^3P$ transition and the two remaining components of the $1s2s^3S-2s2p^3P$ transitions ($^3S_1-^3S_1-^3P_0$) grouped as a single spectral feature.

The density dependence of the aluminum hydrogenlike satellites is shown in Fig. 13 for an electron temperature of 800 eV. These satellite intensities are drifting upward toward LTE values as was seen in Fig. 11 for the heliumlike satellites but the onset of the departure from coronal values takes place at slightly higher densities. The satellite due to the $1s2p^3P-2p^2^3P$ transition shows very unusual behavior with density; not coincidentally, the

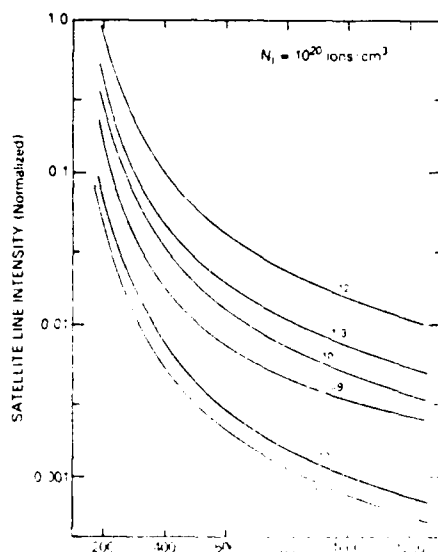


FIG. 12. Hydrogenlike satellite line intensities, normalized to the Lyman- α line vs temperature for an aluminum plasma at 10^{20} ions/cm³ (for key, see Fig. 7).

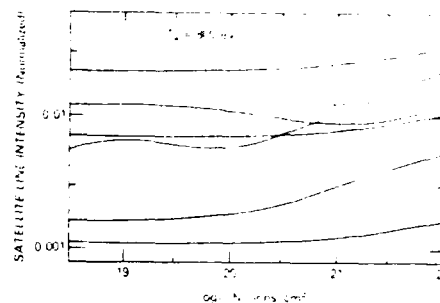


FIG. 13. Hydrogenlike satellite line intensities, normalized to the Lyman- α line vs ion density for an aluminum plasma at 800 eV (for key, see Fig. 7).

$2p^2^3P$ level is populated predominantly by inner-shell excitation as opposed to electron capture, and the unusual trend of this curve will be discussed later in the section on inner-shell effects (Sec. III D).

C. Z scaling of satellite intensities

An analysis of carbon and argon satellite emission, similar to that for aluminum as shown in Figs. 10–13, was also completed. However, after inspecting the behavior of the emission with T_e and N_i , no new or unusually striking behavior was found, and it was decided not to include those plots in this study. Instead, we defer to a plot of the satellite emission as a function of Z , shown in Fig. 14 for plasmas at a density of 10^{20}

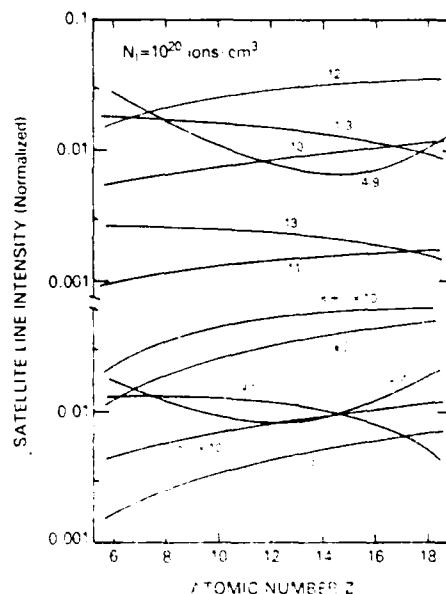


FIG. 14. Hydrogenlike and heliumlike satellite, normalized line intensities as a function of Z at an ion density of 10^{20} ions/cm³. Temperature is that at which the one- and two-electron ions have equal populations (see Fig. 9).

ions/cm³. In comparing the satellite emission from different materials, a choice of appropriate electron temperature for each material had to be made. For the comparison in Fig. 14, we used the temperature at which the heliumlike and hydrogenlike ion population densities were equal at a plasma density of 10²⁰ ions/cm³; from Fig. 9, this can be seen to be 50 eV for carbon, 650 eV for aluminum, and 2200 eV for argon. Once again, the satellite intensities in Fig. 14 are normalized to their respective resonance line intensity.

An explanation as to the detailed behavior of each line with Z is quite complex, since competing collisional and radiative mechanisms in both the singly and doubly excited states are strongly intermingled effects controlling the line intensities. At 10²⁰ ions/cm³, for example, many of the aluminum and argon satellite intensities are still close to their coronal values, while for carbon, they have already begun to tend toward the LTE values at this density. This is particularly noticeable in the (a,b,c,d) and $1s2p^3P-2p^2P$ intensities, which exhibit a drop from C to Al and a subsequent rise from Al to Ar. As seen in Figs. 11 and 13, these two satellites are very density sensitive; for $Z=6$, the effect of collisional coupling to nearby doubly excited levels has begun to populate the $1s2p^2P$ and $2p^2P$ levels at 10²⁰ ions/cm³ and their intensities have risen above coronal values, only to drop with increasing Z , as the coronal regime is reentered. Having only three data points to plot, it's not clear whether these ratios continue to rise or flatten out in the vicinity of $Z=18$; another set of values, say at iron ($Z=26$), would answer the question.

The general trend in the intensity ratios from Al to Ar can be estimated using a simple coronal scheme including only one autoionizing level, the next-highest ground state, and one excited level to that ground state (labeled by d , g , and x). Solving the simple three-level system yields the equations

$$\frac{I_s}{I_R} = \frac{N_d A_d}{N_x A_x} = \frac{N_g C A_d / (A_d + \Gamma)}{N_g X} = \frac{C A_d}{X(A_d + \Gamma)}, \quad (2)$$

where I_s and I_R are the satellite and resonance line intensities, N_d and N_x are the doubly and singly excited level intensities, A is radiative decay, Γ is autoionization, C is electron capture, and X is the impact excitation rate between g and x . The quantity C is proportional to Γ , so the expression becomes

$$\frac{I_s}{I_R} = \frac{1}{X} \left(\frac{\Gamma A_d}{\Gamma + A_d} \right). \quad (3)$$

For most of the satellite transitions, the term in the large parentheses increases with Z and the normalized intensities also exhibit an increase with Z . In some cases, however, the trend is decreasing (q,r) or only slightly increasing ($s-3,13$), and the slight increase of $X(N_e)$ with Z (at the temperatures used in Fig. 14) causes the satellite intensities to drop.

D. Impact excitation and ionization effects

One important aspect of the detailed collisional model employed here is that it allows us to investigate the role of the various collisional processes in determining the satellite intensities. At high plasma density, Jacobs and Blaha⁴⁷ showed that the angular-momentum-changing collisions between doubly excited levels have a strong effect on the intensities. Bhalla *et al.*¹¹ also showed the importance of inner-shell excitation on certain heliumlike satellite lines while Lunney and Seely³¹ showed that inner-shell excitation of hydrogenlike satellites can affect the triplet-to-singlet density-sensitive line ratio. In this study, we show the direct effects of omitting certain collisional processes on the intensities of individual satellites of both systems, including the neglect of collisional ionization and recombination to $n=2$ levels as well as inner-shell effects. In Fig. 15, we have plotted the (normalized) satellite line intensities versus density for several satellite lines in an 800-eV aluminum plasma. The solid curves are those corresponding to the complete collisional model and mimic those shown earlier in Figs. 11 and 13. The dashed curves are the result of setting the electron impact ionization and collisional recombination rate coefficients to zero in the calculation. Although only four satellite intensities are shown in the figure, the effect was identical for all lines from a given ion: Including the collisional couplings to $n=2$ levels of the next-highest charge state brings the relative satellite intensities down at high plasma densities.

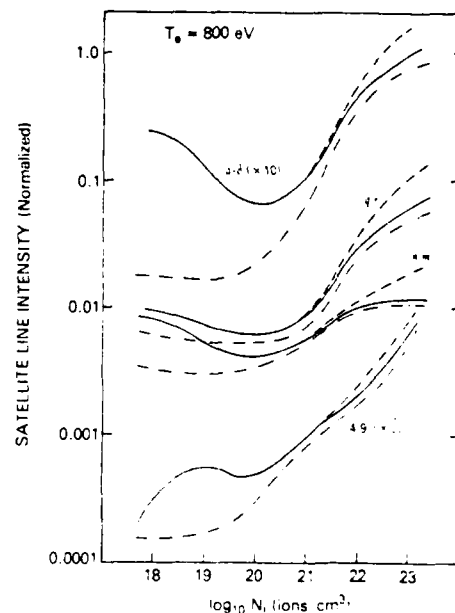


FIG. 15. Selected (normalized) satellite line intensities for an aluminum plasma at 800 eV. Comparison shows the complete collisional model (solid), neglecting collisional ionization and recombination (dashed), and neglecting inner-shell impact excitation and deexcitation (dashed-dotted).

For aluminum the onset of this effect is between 10^{21} and 10^{22} ions/cm³, although it occurs at lower densities for lower-*Z* materials as was encountered with the carbon satellites. It also occurs at a lower density for the heliumlike satellites than for the hydrogenlike satellites, as seen in the figure. In general, the density threshold for these collisional effects to manifest themselves in the line ratios is higher than the range over which the satellite diagnostics are usually applied. However, caution must be taken when dealing with superdense plasmas such as laser-imploded microballoon targets, since these densities have been attained.

The next effect of interest was the impact of inner-shell electron collisions on the satellite intensities. For this study, the inner-shell excitation and deexcitation rate coefficients were set to zero in the model. The results are shown as dashed-dotted curves in Fig. 15. Only four satellites are shown since the remaining satellite intensities suffered less than a 10% perturbation due to the neglect of the innershell rates over the density range shown. The degree to which the innershell processes are important can be measured by the difference between these curves and those of the complete model (solid lines). The (q,r) satellite curves indicate that inner-shell processes are probably comparable to electron capture in populating the $1s2s(^1P)2p$ level while inner-shell excitation is dominant for the $1s2p^2S(n,m)$, $1s2p^2P(a,b,c,d)$, and $2p^2P(4-9)$ levels. The universal trend that is evident in the figure is that an essential populating mechanism for certain levels is missing when inner-shell excitation is neglected in a collisional model and the corresponding satellite lines are much reduced in intensity. Note, however, that inner-shell processes play a much-diminished role in the ionization balance as the plasma density is increased. The explanation for this is as follows: At low densities, the doubly excited levels are collisionally uncoupled from each other and levels which have small electron capture rates depend on inner-shell excitation to populate them. As the density increases, however, the cross-coupling rates come into play, and the levels which depend strongly on the inner-shell processes are now populated by electron collisions from the autoionizing states. This alternate creation mechanism reduces the role of inner-shell excitation at these higher densities, and the curve which doesn't include inner-shell effects approaches the solid curve.

The fact that these satellites have small autoionization rates (and, hence, small electron capture rates, compared to the inner-shell excitation rates) is what makes them excellent diagnostic indicators of density. For example, let us examine the behavior of the (a,b,c,d) satellite lines in Fig. 15, which display an unusual double-valued nature. At 10^{18} ions/cm³, inner-shell excitation via the $1s^22p^2P-1s2p^2P$ transition populates the upper level, and the satellite lines are ten times more intense than if this process was neglected. At about 3×10^{17} ions/cm³, the lithiumlike $n=2$ state densities depart from their coronal values and begin to drop with density as ionization processes shift population to higher ions. As the $1s^22p$ level depletes, the $1s2p^2P$ level follows and the satellite intensity drops. As the density increases further, the collisional coupling between doubly excited states becomes

significant (at about 10^{20} ions/cm³) and the $1s2p^2P$ state is repopulated; hence, the (a,b,c,d) satellite intensity increases. A more detailed discussion of these satellites in relation to density diagnostics follows in Sec. III E.

Two final points should be emphasized regarding inner-shell processes and these satellite lines. Inner-shell excitation was found to be important in populating only a few of the levels in an equilibrium plasma. In a transiently ionizing plasma, however, where the ionization temperature significantly lags behind the electron temperature, electron capture may be dominated by inner-shell impact excitation for all the doubly excited levels, due to the reduced ground-state population available for the dielectronic recombination process.²⁰ Also, collisional deexcitation from doubly to singly excited levels does not seem to play a major role in the determination of the satellite line intensities over the useful diagnostic temperature range until electron densities of about 10^{24} cm⁻³ are attained. For example, at $N_e = 10^{23}$ cm⁻³ and $T_e = 800$ eV, the neglect of inner-shell deexcitation in an aluminum plasma resulted in only a 3.5% error in the calculated $(1s2s^3S-2s2p^3P+1s2p^3P-2p^2P)/(1s2p^1P-2p^2D)$ line ratio.

E. Density diagnostics

As stated earlier, several of the satellite lines emanating from levels which are not strongly autoionizing are density sensitive. In addition, the density sensitivity of certain satellites at high-density can color other diagnostics, in particular the well-known intercombination-to-resonance line ratio $[1s^2-1s2p^3P/(1s^2-1s2p^1P)]$.²⁸ This ratio is regularly exploited for density determinations in laboratory plasmas, despite the fact that several heliumlike satellite lines are usually blended unresolvably with the IC line. From Fig. 8 one can see, for example, that the (m,n) satellites overlap the carbon IC line, the (m,n) and (s,t) satellites overlap the aluminum IC line, and the (m) and (s,t) satellites overlap the argon IC line. Although these satellites are not intense at lower densities, their density dependence can influence this ratio as N_i increases. Ilyukhin *et al.*¹⁷ realized this fact and attempted to correct for the effect by scaling the blended satellite intensities with the resolvable (j,k) lines. As an example of this effect, the IC-to-RES ratio is shown in Fig. 16 for an 800-eV aluminum and a 1600-eV argon plasma. The dashed curve is the IC-to-RES intensity ratio alone, while the solid curve includes the (s,t,m,n) satellites for aluminum and the (s,t,m) satellites for argon. The largest contribution is from the (m) satellite, while the (s,t) and (n) are each about half the intensity of the (m) line. As the figure shows, serious errors in the ion (electron) density determination can result from ignoring the satellite contribution to the total line intensity in the vicinity of the IC line. It will be shown in a following paper that self-absorption in an optically thick plasma further enhances the differences seen in Fig. 16.

Another density-sensitive line among the heliumlike satellites is the (a,b,c,d) blend as first pointed out by Jacobs and Blaha.⁴ The (normalized) intensity of this feature is shown versus ion density in Fig. 17, for a 60-eV

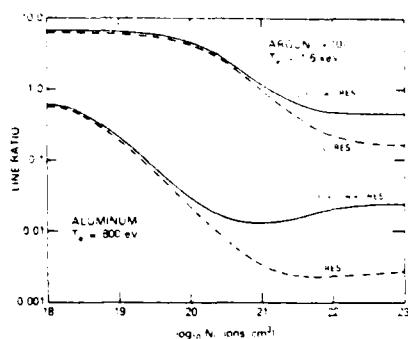


FIG. 16. IC-to-RES line intensity ratio vs ion density for an 800-eV aluminum plasma and a 1600-eV argon plasma (dashed). Also shown is the IC + s,t,m,n -to-RES ratio for aluminum and the IC + s,t,m -to-RES ratio for argon (solid).

carbon, 800-eV aluminum, and 1600-eV argon plasma [for argon, the resolvable feature is the (a,d,r) blend]. Over the 10^{18} – 10^{23} ion/cm³ range, the aluminum and argon line ratios are double-valued, as was discussed in Sec. III D. Care must be taken, therefore, to ascertain on which side of the minimum the density lies when making density determinations via this diagnostic. For carbon, however these lines may be the most valuable diagnostic among the heliumlike lines, since the IC line is usually too weak to be detected in most carbon spectra. This intensity ratio may also be of special importance in laser-fusion experiments which use argon as a seed gas for diagnostic purposes. Since these heliumlike satellites occur at lower plasma temperatures than do the hydrogenlike satellites, they may be more intense in the dense, imploded core where temperatures are lower than in the corona.

Finally, the density-sensitive 3P hydrogenlike satellites have received much attention from previous workers^{22–32} in recent years, particularly because of their usefulness in laser-target compression experiments.¹⁰ In Fig. 18, the $(1s2s\ ^3S - 2s2p\ ^3P) + (1s2p\ ^3P - 2p^2\ ^3P)/(1s2p\ ^1P - 2p^2\ ^1D)$ line intensity ratio versus ion density is shown for carbon (60 eV), aluminum (800 eV), and argon (1600 eV). Also shown are the results of neglecting collisional ionization and recombination to the $n=2$ hydrogenic level (dashed

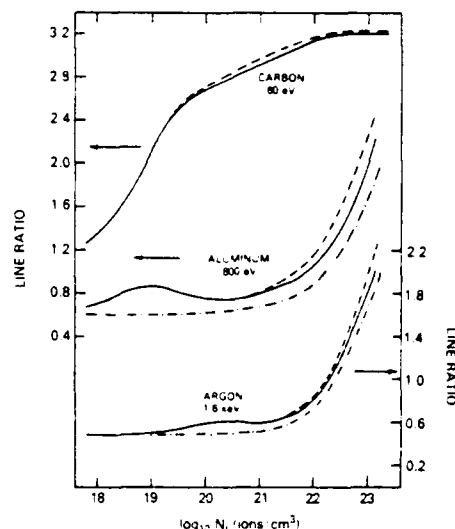


FIG. 18. Total "triplet" to "singlet-D" hydrogenlike satellite line intensity ratio vs ion density for the same temperatures as in Fig. 17. Comparison shows the complete collisional model (solid), neglecting collisional ionization and recombination (dashed), and neglecting inner-shell impact excitation and deexcitation (dashed-dotted).

curve) and neglecting inner-shell impact excitation and deexcitation to the $1s2s$ and $1s2p$ levels (dashed-dotted curves). The dashed-dotted curve for carbon is not shown since the results varied by less than a few percent from the complete model. As seen from the various curves, omitting either of the collisional processes results in no more than a factor of 2–3 error in the density determination in the region where the ratio is a sensitive diagnostic. The noticeable bump in the aluminum and argon ratios is the effect of inner-shell excitation for the $1s2p\ ^3P - 2p^2\ ^3P$ transition. It should be noted once again, that these are results from an equilibrium model, in which the atomic processes occur on a rapid enough time scale that the ionization balance reflects the local plasma electron temperature. The study of satellite lines in a transient plasma will be the subject of a later investigation.

IV. DISCUSSION

To summarize, a new model has been described for characterizing the emission from the $n=2$ dielectronic satellite lines to the heliumlike and hydrogenlike resonance lines in dense plasmas. In this model, the doubly excited level populations are solved for *self-consistently* with a number of singly excited and ground levels for a plasma in collisional-radiative equilibrium. In addition great care has been taken to calculate rate coefficients for all the relevant collisionally induced and spontaneous processes to high accuracy using sophisticated atomic structure and scattering models.

The behavior of the satellite lines has been studied in the "optically thin plasma" approximation and their vari-

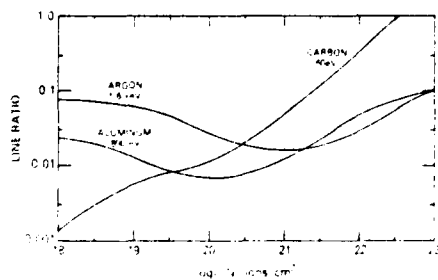


FIG. 17. a,b,c,d satellite-to-resonance line intensity ratio vs ion density for a 60-eV carbon, 800-eV aluminum, and a 1600-eV argon plasma (the argon ratio is the $a-d,r$ -to-RES lines).

ation with temperature and density described. The effects of neglecting inner-shell processes and collisional ionization were shown to cause large errors in theoretically calculated intensities in some density regimes and to have a negligible effect in others. Density determinations using the heliumlike intercombination-to-resonance line ratio were found to be strongly impacted by unresolvable satellites at higher densities. The effects were shown to commence at densities of about $10^{21} \text{ e}^-/\text{cm}^3$, corresponding to the critical density for 1.06- μm laser light, and to become more important as the density increased, causing as much as 2 orders of magnitude error in the measured plasma density. The (a-d) satellite lines are also shown to be a valuable density diagnostic at temperatures lower than those where the density-sensitive hydrogenlike satellites can be detectable. This diagnostic is of special importance for low-Z plasmas where the intercombination line is often too weak to be detected. Finally, we investigated the ratio of the triplet satellite lines to the 1D satellite adjacent to the Lyman- α line, and found that inner-shell and/or ionizing collisions can affect the density determination by factors of 2 to 3 in the useful density and temperature range of the diagnostic.

In conclusion, there are two additional points which should be mentioned. The first regards a recent paper⁷⁰ dealing with dielectronic capture followed by ladderlike excitation and ionization in dense plasmas. The conclusion arrived at in this paper is that the effective collisional ionization rate is significantly enhanced when one includes a large number (in this case, up to principal quantum number 20) of the higher doubly excited levels; thus, the actual ionization state in a dense plasma can be

larger than one would calculate without inclusion of these levels. That this investigation arrives at such a result is not too surprising since excitation rates often exceed ionization rates by more than an order of magnitude. In fact, the same conclusion was reached in an earlier study²⁵ regarding ionization via excitation of *singly excited* levels in attaining LTE conditions. However, no mention is made in their paper of continuum lowering (where pressure ionization may force the outer electrons of many of these doubly excited states into the continuum). The point here is that, in a plasma at high electron densities, it may be difficult to assess the ladderlike processes without self-consistently including the effects of ionization lowering and level shifts, widths, and merging (and, hence, Stark broadening) in the model.

Finally, in this study we have neglected the plasma microfield effects on the autoionization-dielectronic capture processes. In addition, no attempt was made to take account of the effects of strongly overlapping lines⁷¹⁻⁷³ or of the true Fano-Beutler profile⁷⁴ in the calculations. Both of these effects, as well as photon self-absorption and nonequilibrium plasma effects, are presently under investigation and will be reported on later.

ACKNOWLEDGMENTS

We would like to thank R. D. Cowan for his assistance in calculating the atomic data and P. C. Kepple and H. R. Griem for helpful discussions and useful suggestions regarding the manuscript. This work was supported in part by the Defense Nuclear Agency and the Office of Naval Research.

*Also at Laboratory for Plasma and Fusion Energy Studies, University of Maryland, College Park, MD 20742.

¹B. Edlén and F. Tyren, *Nature* **143**, 940 (1939).

²B. Edlén, *Physica (Utrecht)* **13**, 545 (1947).

³G. A. Sawyer, F. C. Jahoda, F. L. Ribe, and T. F. Stratton, *J. Quant. Spectrosc. Radiat. Transfer* **2**, 467 (1962).

⁴N. V. Roth and R. C. Elton, Naval Research Laboratory Memorandum Report No. 6638 (unpublished).

⁵U. Feldman and L. Cohen, *Astrophys. J. Lett.* **158**, L169 (1969).

⁶S. Goldsmith, *J. Phys. B* **2**, 1075 (1969).

⁷N. J. Peacock, R. J. Spear, and M. G. Hobby, *J. Phys. B* **2**, 798 (1969).

⁸A. H. Gabriel and C. Jordan, *Nature* **221**, 947 (1969).

⁹A. H. Gabriel and T. M. Paget, *J. Phys. B* **5**, 673 (1972).

¹⁰A. H. Gabriel, *Mon. Not. R. Astron. Soc.* **160**, 99 (1972).

¹¹C. P. Bhalla, A. H. Gabriel, and L. P. Presnyakov, *Mon. Not. R. Astron. Soc.* **172**, 359 (1975).

¹²A. B. Walker and H. R. Rugge, *Astrophys. J.* **164**, 181 (1971).

¹³W. M. Neupert, *Solar Phys.* **18**, 474 (1971).

¹⁴G. A. Doschek, *Space Sci. Rev.* **13**, 765 (1972).

¹⁵J. H. Parkinson, *Nature* **236**, 68 (1972).

¹⁶Yu. I. Grineva *et al.*, *Solar Phys.* **22**, 441 (1973).

¹⁷J. L. Schwob and B. S. Fraenkel, *Space Sci. Rev.* **13**, 589 (1972).

¹⁸N. J. Peacock, M. G. Hobby and M. Galanti, *J. Phys. B* **6**, L298 (1973).

¹⁹U. Feldman, G. A. Doschek, D. J. Nagel, W. E. Behring, and R. D. Cowan, *Astrophys. J.* **182**, 417 (1974).

²⁰U. Feldman, G. A. Doschek, D. J. Nagel, R. D. Cowan, and R. R. Whitlock, *Astrophys. J.* **192**, 213 (1974).

²¹J. Davis and V. L. Jacobs, *Phys. Rev. A* **12**, 2017 (1975).

²²J. C. Weisheit, *J. Phys. B* **8**, 2556 (1975).

²³V. I. Bayanov *et al.*, *Zh. Eksp. Teor. Fiz. Pis'ma Red.* **24**, 352 (1976) [*JETP Lett.* **24**, 319 (1976)].

²⁴A. V. Vinogradov, I. Yu. Skobelev, and E. A. Yukov, *Zh. Eksp. Teor. Fiz.* **72**, 1762 (1977) [*Sov. Phys. JETP* **45**, 925 (1977)].

²⁵I. Yu. Skobelev, A. V. Vinogradov and E. A. Yukov, *Phys. Scr.* **18**, 78 (1978).

²⁶A. V. Vinogradov and I. Yu. Skobelev, *Zh. Eksp. Teor. Fiz. Pis'ma Red.* **27**, 97 (1978) [*JETP Lett.* **27**, 88 (1978)].

²⁷A. V. Vinogradov, I. Yu. Skobelev, and E. A. Yukov, *Usp. Fiz. Nauk* **129**, 177 (1979) [*Sov. Phys. Usp.* **22**, 771 (1979)].

²⁸J. F. Seely, *Phys. Rev. Lett.* **42**, 1606 (1979).

²⁹J. F. Seely, R. H. Dixon, and R. C. Elton, *Phys. Rev. A* **23**, 1437 (1981).

³⁰J. G. Lunney and J. F. Seely, *Phys. Rev. Lett.* **46**, 342 (1981).

³¹J. G. Lunney and J. F. Seely, *J. Phys. B* **15**, L121 (1982).

³²D. Duston and J. Davis, *Phys. Rev. A* **21**, 932 (1980).

³³A. H. Gabriel and K. J. Phillips, *Mon. Not. R. Astron. Soc.* **189**, 319 (1979).

³⁴E. Ya. Kononov *et al.*, *Zh. Eksp. Teor. Fiz. Pis'ma Red.* **21**, 720 (1980) [*JETP Lett.* **31**, 679 (1980)].

- ³⁵F. Bely-Dubau, A. H. Gabriel and S. Volonte, *Mon. Not. R. Astron. Soc.* **186**, 405 (1979).
- ³⁶F. Bely-Dubau, A. H. Gabriel, and S. Volonte, *Mon. Not. R. Astron. Soc.* **189**, 801 (1979).
- ³⁷F. Bely-Dubau, J. Dubau, P. Faucher, and L. Steenman-Clark, *J. Phys. B* **14**, 3313 (1981).
- ³⁸F. Bely-Dubau, J. Dubau, P. Faucher, and A. H. Gabriel, *Mon. Not. R. Astron. Soc.* **198**, 239 (1982).
- ³⁹F. Bely-Dubau *et al.*, *Phys. Rev. A* **26**, 3459 (1982).
- ⁴⁰M. Bitter *et al.*, *Phys. Rev. Lett.* **43**, 129 (1979).
- ⁴¹M. Bitter *et al.*, *Phys. Rev. Lett.* **47**, 921 (1981).
- ⁴²TFR Group, J. Dubau, and M. Loulergue, *J. Phys. B* **15**, 1007 (1981).
- ⁴³E. Källne, J. Källne, and J. E. Rice, *Phys. Rev. Lett.* **49**, 330 (1982).
- ⁴⁴E. Källne, J. Källne, and A. K. Pradhan, *Phys. Rev. A* **27**, 1476 (1983).
- ⁴⁵E. Källne, J. Källne, and R. D. Cowan, *Phys. Rev. A* **27**, 2682 (1983).
- ⁴⁶R. U. Datla, L. A. Jones, and D. B. Thomson, Los Alamos National Laboratory Report No. LA-8324-MS (unpublished).
- ⁴⁷V. L. Jacobs and M. Blaha, *Phys. Rev. A* **21**, 525 (1980).
- ⁴⁸I. A. Armour, B. C. Fawcett, J. D. Silver, and E. Träbert, *J. Phys. B* **13**, 2701 (1980).
- ⁴⁹V. A. Boiko, A. Ya. Faenov, and S. A. Pikuz, *J. Quant. Spectrosc. Radiat. Transfer* **19**, 11 (1978).
- ⁵⁰D. R. Bates, A. E. Kingston, and R. W. P. McWhirter, *Proc. R. Soc. London, Ser. A* **267**, 297 (1962).
- ⁵¹H. W. Drawin, *Z. Phys.* **225**, 483 (1969).
- ⁵²D. Richards, *J. Phys. B* **6**, 823 (1973).
- ⁵³R. D. Cowan, *Phys. Rev.* **163**, 54 (1967); *J. Opt. Soc. Am.* **58**, 808 (1968).
- ⁵⁴A. Burgess, in *Proceedings of the Symposium on Atomic Collision Processes in Plasmas*, Culham, England, 1964 (unpublished).
- ⁵⁵V. L. Jacobs, J. Davis, P. C. Kepple, and M. Blaha, *Astrophys. J.* **211**, 605 (1977).
- ⁵⁶W. J. Karzas and B. Latter, *Astrophys. J., Suppl. Ser.* **6**, 167 (1961).
- ⁵⁷V. L. Jacobs and J. Davis, *Phys. Rev. A* **18**, 697 (1978).
- ⁵⁸L. A. Vainshtein and U. I. Safranov, *At. Data Nucl. Data Tables* **21**, 49 (1978).
- ⁵⁹J. Davis, P. C. Kepple, and M. Blaha, *J. Quant. Spectrosc. Radiat. Transfer* **16**, 1043 (1977).
- ⁶⁰A. K. Pradhan, D. W. Norcross, and D. G. Hummer, *Phys. Rev. A* **23**, 619 (1981); *Astrophys. J.* **246**, 1031 (1981).
- ⁶¹M. J. Seaton, *Adv. At. Mol. Phys.* **11**, 83 (1975).
- ⁶²E. Clementi and C. Roetti, *At. Data Nucl. Data Tables* **14**, 177 (1974).
- ⁶³S. J. Goett, D. H. Sampson, and R. E. H. Clark, *At. Data Nucl. Data Tables* **28**, 279 (1983).
- ⁶⁴D. H. Sampson and R. E. H. Clark, *Astrophys. J., Suppl. Ser.* **44**, 169 (1980).
- ⁶⁵D. Duston and J. Davis, *Phys. Rev. A* **21**, 1664 (1980); **24**, 1505 (1981); *J. Quant. Spectrosc. Radiat. Transfer* **27**, 267 (1982).
- ⁶⁶D. Duston, R. W. Clark, J. Davis, and J. P. Apruzese, *Phys. Rev. A* **27**, 1441 (1983).
- ⁶⁷H. R. Griem, *Plasma Spectroscopy* (McGraw-Hill, New York, 1964).
- ⁶⁸A. V. Vinogradov, I. Yu. Skobelev, and E. A. Yukov, *Kvant. Elektron. (Moscow)* **2**, 1165 (1975) [*Sov. J. Quantum Electron.* **5**, 630 (1975)].
- ⁶⁹A. A. Ilyukhin, A. E. Kramida, G. V. Peregudov, and V. A. Chirkov, *Kvant. Elektron. (Moscow)* **8**, 64 (1981) [*Sov. J. Quantum Electron.* **11**, 34 (1981)].
- ⁷⁰T. Fujimoto and T. Kato, *Phys. Rev. Lett.* **48**, 1022 (1982).
- ⁷¹M. Baranger, *Phys. Rev.* **111**, 481 (1958); **111**, A494 (1958); **112**, A855 (1958).
- ⁷²A. C. Kolb and H. R. Griem, *Phys. Rev.* **111**, 514 (1958).
- ⁷³V. L. Jacobs and J. Davis, Naval Research Laboratory Memorandum Report No. 4365 (unpublished).
- ⁷⁴U. Fano, *Phys. Rev.* **124**, 1866 (1961), and H. Beutler, *Z. Phys.* **93**, 177 (1935).

D. Dielectronic Recombination of Krypton Ions

I. INTRODUCTION

The rate coefficients for radiative and dielectronic recombination are needed to predict the relative abundances of various ions in a high-temperature plasma. These relative abundances may be used to calculate the far-ultraviolet and X-ray emission spectra produced by electron-ion collisions. In the corona model approximation (Griem 1964), which is valid at low-densities, the recombination coefficients are functions only of the local electron temperature and are independent of the electron density. This approximation is expected to be valid for the K-shell ions of a high-Z element over an extensive density range. However, the coefficients for the L- and M-shell ions are expected to be much more sensitive to density effects.

Burgess (1964) first demonstrated that dielectronic recombination is often more important than the usual free-bound radiative process in the temperature region where the ions have their maximum abundance in ionization equilibrium. A simple formula was derived by Burgess (1965) for estimating the dielectronic recombination rates in the corona model approximation. This simple formula requires knowledge of only the energy levels and absorption oscillator strengths of the recombining ion. However, ionization - equilibrium calculations which have been carried out using the Burgess formula (Jordan 1969) do not agree with more detailed calculations (Jacobs et. al. 1977) in which the rates for all radiative decay and autoionization processes from the doubly-excited states are taken into account. This is attributable to the discovery that, for certain ions, autoionization into an excited state of the recombining ion is more probable than autoionization to the ground state.

II. THEORY

Dielectronic recombination may be described as a two-step process. Radiationless capture of a plasma electron into an $n'l$ -state accompanied by the excitation $i \rightarrow j$ of the recombining ion $X^{+(Z)}$ results in the formation of a doubly-excited state

$$X^{+(Z)}(i) + e^- \rightarrow X^{+(Z-1)}(j, nl) . \quad (1)$$

Recombination occurs if, instead of autoionization, the doubly-excited state j, nl undergoes radiative decay to a singly-excited state i, nl which lies below the ionization threshold

$$X^{+(Z-1)}(j, nl) \rightarrow X^{+(Z-1)}(i, nl) + h\nu . \quad (2)$$

The initial state i is assumed to be the ground state in the corona model approximation. In our calculations, the many-electron states i and j will be specified by giving only the principal and angular momentum quantum numbers of the active electron.

Assuming that the electrons have a maxwellian velocity distribution, the dielectronic recombination rate coefficient in the corona model approximation is given by (Shore 1969)

$$\alpha_d(i) = 2^3 a_o^3 \pi^{3/2} (E_H/k_B T_e)^{3/2} \\ \times \sum_j \sum_{nl} \frac{g(j, nl)}{2g(i)} \frac{A_a(j, nl \rightarrow i) A_r(j, nl \rightarrow i, nl)}{A_a(j, nl) + A_r(j, nl)} \\ \times \exp \left\{ \frac{E(i) - E(j, nl)}{k_B T_e} \right\} , \quad (3)$$

where $E(i)$ and $E(j, nl)$ are the initial-state and doubly-excited state energy levels, respectively, and $g(i)$ and $g(j, nl)$ are their statistical weights.

III. CALCULATIONS

For large values of n the autoionization rates $A_a(j, nl \rightarrow i)$ can be obtained from the threshold values of the partial-wave cross section for the electron impact excitation

$$X^{+(Z)}(i) + e^-(k_i, l_i) \rightarrow X^{+(Z)}(j) + e^-(k_j, l_j) , \quad (4)$$

by using the quantum-defeat theory relationship derived by Seaton (1969). The distorted-wave method (Davis et.al. 1976) was used to obtain the excitation cross sections. The stabilizing radiative decay rates $A_r(j, n_l \rightarrow i, n_l)$ were approximated by the spontaneous emission rate $A_r(j \rightarrow i)$ for the recombining ion core. These approximations are expected to be valid for $\Delta n_l = 0$ transitions of the ion core, which occur predominantly by means of large n -values. They are uncertain for Δn_l not equal to 0 transitions, for which small n -values play a more important role, especially with increasing Z . The total decay rates $A_a(j, n_l)$ and $A_r(j, n_l)$ include the rates for all allowed autoionization and radiative decay processes. For some Δn_l not equal to 0 transitions, autoionization into an excited state of the recombining ion can occur and is found to be more probable than autoionization into the ground state. This gives a substantially smaller recombination rate than predicted by the Burgess formula.

The dielectronic recombination rate coefficients for Kr XXVI - XXXVI have been calculated, taking into account the autoionization processes and stabilizing radiative transitions which involve a single-electron electric-dipole transition of the recombining ion core. The transitions included are given in Table I. The asterisk has been used to identify the transitions whose contribution to α_d is reduced by autoionization into an excited state.

The total dielectronic recombination coefficient for each ion is given in Table II for the temperature region of experimental interest. The K-shell ions are expected to have density-independent recombination coefficients, even at densities as high as 10^{22} cm^{-3} . The results for the L- and M-shell ions may not be valid at such high densities because of collisional processes involving the outer n_l -electron. To obtain the total recombination coefficient in the corona model approximation, the direct radiative recombination coefficients must be added to the results in Table II. Estimates based on hydrogenic approximations indicate that for these Kr ions radiative recombination is almost as important as dielectronic recombination. This is to be expected from Z -scaling arguments.

Table 1
Stabilizing Radiative Transitions $j \rightarrow i$

Recombining ion	Single-Electron Transitions $j \rightarrow i$
Kr XXXVI	$2p \rightarrow 1s, 3p \rightarrow 1s$
Kr XXXV	$2p \rightarrow 1s, 3p \rightarrow 1s$
Kr XXXIV	$2p \rightarrow 2s, 3p \rightarrow 2s^*$
Kr XXXIII	$2p \rightarrow 2s, 3p \rightarrow 2s^*$
Kr XXXII	$2p \rightarrow 2s, 3s \rightarrow 2p, 3d \rightarrow 2p^*$
Kr XXXI	$2p \rightarrow 2s, 3s \rightarrow 2p, 3d \rightarrow 2p^*$
Kr XXX	$2p \rightarrow 2s, 3s \rightarrow 2p, 3d \rightarrow 2p^*$
Kr XXIX	$2p \rightarrow 2s, 3s \rightarrow 2p, 3d \rightarrow 2p^*$
Kr XXVIII	$2p \rightarrow 2s, 3s \rightarrow 2p, 3d \rightarrow 2p^*$
Kr XXVII	$3s \rightarrow 2p, 3d \rightarrow 2p^*$
Kr XXVI	$3p \rightarrow 3s, 4p \rightarrow 3s^*$

*Affected by autoionization into an excited state.

Table II
Dielectronic Recombination Rate
Coefficients ($\text{cm}^3\text{sec}^{-1}$)

$\text{Log}_{10}T_e(K_0)$	Kr XXVI	Kr XXVII	Kr XXVIII	Kr XXIV	Kr XXX
6.0	0.97(-10)	0.17(-13)	0.10(-10)	0.24(-10)	0.35(-10)
6.4	0.39(-10)	0.41(-12)	0.72(-11)	0.19(-10)	0.26(-10)
6.8	0.12(-10)	0.93(-12)	0.42(-11)	0.11(-10)	0.14(-10)
7.2	0.32(-11)	0.71(-12)	0.26(-11)	0.68(-11)	0.79(-11)
7.6	0.84(-11)	0.29(-12)	0.11(-11)	0.29(-11)	0.33(-11)
8.0	0.21(-12)	0.89(-12)	0.36(-12)	0.93(-12)	0.10(-11)

$\text{Log}_{10}T_e(K_0)$	Kr XXXI	Kr XXXII	Kr XXXIII	Kr XXXIV	Kr XXXV	Kr XXXVI
6.0	0.50(-10)	0.53(-10)	0.73(-10)	0.25(-10)	0.25(-55)	0.50(-56)
6.4	0.38(-10)	0.34(-10)	0.47(-10)	0.14(-10)	0.51(-28)	0.19(-28)
6.8	0.18(-10)	0.14(-10)	0.18(-10)	0.48(-11)	0.17(-17)	0.77(-18)
7.2	0.81(-11)	0.60(-11)	0.55(-11)	0.16(-11)	0.12(-13)	0.64(-14)
7.6	0.31(-11)	0.22(-11)	0.15(-11)	0.52(-12)	0.20(-12)	0.12(-12)
8.0	0.95(-12)	0.67(-12)	0.41(-12)	0.15(-12)	0.29(-12)	0.19(-12)

References

1. A. Burgess, 1964, Ap. J., 134, 776.
2. A. Burgess, 1965, Ap. J., 141, 1588.
3. J. Davis, P. C. Kepple, and M. Blaha, 1976, J. Quant. Spectrosc. Rad. Transf., 16, 1043.
4. H. R. Griem, 1964 "Plasma Spectroscopy," (New York: McGraw-Hill).
5. V. L. Jacobs, J. Davis, P. C. Kepple, and M. Blaha, 1977, Ap. J., 211, 605.
6. C. Jordan, 1969, M.N.R.A.S., 142, 501.
7. M. J. Seaton, 1969, J. Phys. B, 25.
8. B. W. Shore, 1969 Ap. J., 158, 1205.

E. Coupled Plasma and Radiation Transport Ion Beam Code

I. INTRODUCTION

In order to understand the nature of the dynamic material response of a planar target exposed to a high energy ion beam, particularly in the analysis and assessment of directed energy and/or particle beam lethality and vulnerability experiments, a one-dimensional fully self-consistent energy deposition/stopping power radiation hydrodynamics model has been developed.

In Section II the physical processes included in the model are detailed, along with the numerical formulation employed. Section III presents the basic results of our treatment of the interaction of a 1 MeV proton beam with a planar aluminum target. Section IV compares these results with those obtained when radiation transport is omitted from the calculations. Section V compares our results with a similar laser-target interaction study. Finally, in Section VI, the work is summarized.

II. THEORETICAL MODEL

The interaction of the ion beam with the target is strongly dependent on the local temperature and degree of ionization in the target. In addition, optical pumping and energy transport by photons can influence the plasma temperature and degree of ionization, and can modify the hydrodynamic response of the target. Thus, the deposition of the beam, the hydrodynamic evolution and atomic physics of the target, as well as the transport of radiation, must be calculated self-consistently.

Discussion of the theoretical model can be separated for convenience as follows: (a) hydrodynamics and thermal conduction (b) ionization and atomic physics (c) radiation emission and transport and (d) beam dynamics and energy deposition.

(A) Hydrodynamics and Thermal Conduction

The basic hydrodynamic variables of mass, momentum, and total energy are transported in one dimension using a numerical scheme with a sliding-zone version of flux-corrected transport.¹ A special gridding algorithm is

used which moves zones in a Lagrangian fashion and adjusts the mesh in order to resolve steep gradients in the flow. The hydrodynamic equations solved are

$$\frac{D\rho}{Dt} = \frac{\partial \rho}{\partial t} + \frac{\partial}{\partial x} (\rho u) = 0, \quad (1)$$

$$\frac{D(\rho u)}{Dt} = - \frac{dP}{dx}, \quad (2)$$

$$\begin{aligned} \frac{D\epsilon_T}{Dt} = & - \frac{\partial}{\partial x} (uP) + \dot{\epsilon}_{\text{rad}} + \dot{\epsilon}_{\text{dep}} \\ & + \frac{\partial}{\partial x} \left(- \kappa N^2 \frac{\partial T}{\partial x} \right), \end{aligned} \quad (3)$$

where ρ is mass density, u is velocity, P is pressure, ϵ_T is total energy density, $\dot{\epsilon}_{\text{rad}}$ is the rate of energy loss or gain due to radiation, $\dot{\epsilon}_{\text{dep}}$ is the rate of energy gain due to the beam deposition process, κ is the thermal conductivity, and N is the ion density. The thermal conduction is calculated implicitly, using an iterative Crank-Nicholson scheme.

Since densities did not much exceed solid density in this study, a simple equation of state was assumed with

$$P = \frac{2}{3} (\epsilon_T - \frac{1}{2} \rho u^2 - \epsilon_I), \quad (4)$$

where ϵ_I is the ion potential energy due to ionization and excitation. A single temperature model was employed,

$$kT = \frac{P}{(\rho/m_I) (1+\bar{Z})}, \quad (5)$$

where m_I is ion mass, and T is temperature. The ionization energy, ϵ_I , and effective charge, \bar{Z} , are calculated from the ionization-radiation equations which are explained below. A single temperature assumption is valid in the

cold dense target as well as in the beam deposition region, since thermal equilibration times are short compared with the time scales of the energy input and changes in the hydrodynamic variables.

The local rate of change of energy due to radiation transport $\dot{\epsilon}_{\text{rad}}$, and that due to the beam deposition $\dot{\epsilon}_{\text{dep}}$, will be discussed in the appropriate sections below.

(B) Ionization and Atomic Physics

The ionic populations in the plasma may be characterized by a set of atomic rate equations of the form

$$\frac{df_i}{dt} = \sum_j W_{ji} f_j - \sum_i W_{ij} f_i \quad (6)$$

where f_i is the fractional population of atomic level i , and W_{ji} is the net reaction rate describing the transition from initial state j to final state i . An equation of this type is constructed for each of the atomic levels included in the model.

For sufficiently dense plasmas of the sort we expect to model with the ion-beam code, the effective populating and depopulating rates are extremely fast compared with the hydrodynamic response. An equilibrium assumption can be justified, which involves dropping the explicit time dependence in equation (6). The plasma is then said to be in collisional-radiative equilibrium (CRE)², whereby the plasma ionization state responds instantaneously to changes in hydrodynamic quantities.

The rate coefficients that are used to calculate the populating and depopulating rates, W_{ji} , are calculated using various scattering techniques. The processes included in this calculation and the methods used in calculating the corresponding rate coefficients are summarized below.

(1) Collisional ionization - exchange classical impact-parameter (ECIP) methods³ (the effect of autoionizing resonances on the cross sections has been ignored).

(2) Photoionization - hydrogenic approximation with Karzas-Latter-Gaunt factors.^{4,5}

(3) Dielectronic recombination - the detailed calculations of Jacobs et al.⁶ are used.

(4) Collisional excitation - Coulomb-Born distorted-wave approximation including exchange effects,⁷ or the semiclassical impact-parameter (SCI) technique.⁸

(5) Spontaneous radiative decay - oscillator strengths are taken from several calculations and measurements.⁹

(6) Photoexcitation - oscillator strengths used are those quoted above to determine optical depths (see the next section on radiation transport).

Finally, collisional and radiative recombination, collisional deexcitation, and stimulated emission are all calculated as the detailed balance of the corresponding opposite rate listed above. A simplified level diagram using two ground states and a single excited state is shown in Fig. 1 to show schematically the processes included in the model.

Once the set of rate equations (including the radiation transport) has been solved for the level populations, f_i , the electron density can be calculated,

$$N_e = \sum_i z_i f_i N_I \quad (7)$$

where z_i is the ionic charge of level i and N_I is the total ion density.

The ionization and excitation energy can also be calculated by

$$\epsilon_I = \sum_i \chi_i f_i N_I, \quad (8)$$

where χ_i is the energy of level i , measured from the ground state of the neutral atom.

(C) Radiation Emission and Transport

Radiation emission from a plasma and its opacity are dependent on the local atomic level population densities. Except for optically thin plasmas, however, the level populations depend on the radiation field, since optical pumping via photoionization and photoexcitation can produce significant population redistribution. Thus, the ionization and radiation transport processes are strongly coupled and must be solved self-consistently. In this model, an iterative procedure¹⁰ is used, where level populations are calculated using the radiation field from the previous iteration, then using these populations to calculate a new radiation field and recalculating populations until convergence is reached. Even when the local Thermodynamic Equilibrium (LTE) populations are used, an iterative procedure is required, since the LTE populations are functions of temperature and electron density, which, in turn, depend on the level populations.

Three distinct radiation transport schemes have been developed, and can be used interchangeably in the code: A probabilistic scheme, a multifrequency scheme and a hybrid method. Descriptions of these transport methods have appeared elsewhere; in this brief report, their general properties will be outlined.

The probabilistic model¹¹ forms local angle and frequency averaged escape probabilities for each emission line and for each bound-free process. Free-free radiation is treated with a multifrequency formalism. The radiation transport and emission spectra are calculated from these escape probabilities. The method is cost-effective, can treat comprehensive atomic models and provides good overall energetics, but cannot calculate certain spectral details and breaks down at very high densities where no systematic treatment of Stark profile escape probabilities is available.

The multifrequency model¹² solves the equation of radiation transport at a large number of discrete frequencies, providing resolution of emission lines, recombination edges and absorption edges. It provides accurate radiation transport at high density, and gives spectral details such as self-absorption features. However, a large number of frequencies is required to provide adequate resolution, and it tends to be a relatively costly method.

The hybrid model uses the multifrequency formalism to transport the continuum (bound-free and free-free) radiation, and frequency integrated escape probabilities to transport the lines. Continuum opacities are interpolated from the multifrequency mesh and folded into the line transport calculations. The line opacities are assumed to have negligible impact on the continuum energetics.

In all of the models outlined above, local ionization state-dependent inner-shell opacities are included, since these processes are very important in the cool, dense plasma regions. Inner-shell photoionization cross sections for the neutral element is taken from the fits by Biggs and Lighthill¹³, and the positions of the ionization-dependent absorption edges are taken from the Hartree-Fock calculations of Clementi and Roetti¹⁴.

The local rate of energy change in zone j , due to radiation transport is given by

$$\dot{\epsilon}_j = - \sum_P (F_{Pj} - \sum_k C_{Pkj} F_{Pk}) \quad (9)$$

where F_{Pk} is the rate of energy loss in zone k due to a discrete radiative process (or frequency group) P , and C_{Pkj} is the radiative coupling of zone k to zone j for that process. The couplings are functions of opacity, integrated over process and photon path. In the probabilistic model, a matrix of couplings must be computed for each bound-bound, bound-free and free-free process; for the multifrequency model, they must be computed for each discrete frequency. In this way, the net cooling and heating by radiation emission and absorption among the various zones of the plasma is accurately accounted for.

(D) Beam Dynamics and Energy Deposition

We assume that on the timescale of the target response (several nanoseconds), the beam maintains uniform flow, that is

$$\rho_B u_B = \dot{m} = \frac{J m_B}{e Z_B} \quad (10)$$

where ρ_B and u_B are the local mass density and axial velocity of the beam. The mass flux \dot{m} is assumed constant up to the point the beam is

stopped. J is the beam current per unit area; m_B and Z_B are the mass and charge of a beam ion.

For a relativistic beam with negligible thermal spread, the kinetic energy of a beam ion is related to the local velocity by

$$E_B = \frac{m_B c^2}{\sqrt{(1-u_B^2/c^2)}} - m_B c^2. \quad (11)$$

The energy is also related to the stopping power by

$$E_B = E_0 - \int_{-\infty}^x \left(\frac{dE}{dx}\right)_T dx, \quad (12)$$

where E_0 is the initial energy, and with the total stopping power given by the sum of the ion-free electron, ion-bound electron and ion-plasma ion interactions,

$$\left(\frac{dE}{dx}\right)_T = \left(\frac{dE}{dx}\right)_e + \left(\frac{dE}{dx}\right)_b + \left(\frac{dE}{dx}\right)_i. \quad (13)$$

(1) Interaction with Bound Electrons

The local oscillator model (LOM)¹⁵ representation of the stopping cross section is employed, with the spatial change of energy given by

$$\left(\frac{dE}{dx}\right)_b = (\rho(x)/m_I) S_b(V) \quad (14)$$

with S_b in ergs-cm².

$$S_b(V) = \frac{4\pi Z_B^2 e^4}{mV^2} \int 4\pi r^2 \rho(r) K_0(\tau) dr. \quad (15)$$

where Z_B is the effective charge of the projectile ion, e and m are the electron charge and mass, V is the projectile velocity, $\rho(r)$ is the local bound electron density in the target atom, and $K_0(\tau)$ is a modified zeroth order Bessel function.

$$\tau = h \rho(r)/mV^2, \quad (16)$$

where h is Planck's constant divided by 2π , and $\omega_0(r)$ is the local plasma frequency at radius r within the atom.

There are three assumptions underlying the LOM¹⁶. The first is that a loss function can be defined, dependent only on the local electron density in the target atom. The second is that the longitudinal dielectric response can be represented by $\epsilon(\omega)$ with a single zero at $\omega \sim \omega_0$, subject to the high frequency condition

$$\epsilon(\omega) \sim 1 - \omega_0^2/\omega^2 \quad (17)$$

appropriate to free electrons. The third assumption is that the induced polarization charge is spread out from the ion trajectory to some finite radius of the order of the de Broglie wavelength h/mV . This last assumption is justified by the adiabatic argument that energy will be transferred only to electrons with velocity less than V . A wave packet with momentum of order mV would have a spatial spread of order h/mV .

The electron density $\rho(r)$ is taken from the Thomas-Fermi (TF) model proposed by Zink.¹⁷

In a plasma target, the bound atomic electrons can be screened from the projectile ions by the free electrons. Thus, the LOM must be modified to take this shielding effect into account. For an electron in an isolated atom, the maximum impact parameter is V/ω , where ω is a characteristic frequency of motion¹⁸. Plasma screening limits this parameter to the Debye length D . The expression for τ can be rewritten

$$\tau = (h/mV) (\omega_e(r)/V) . \quad (18)$$

Whenever $V/\omega_0(r) > D$, τ is taken to be

$$\tau = h/mVD \quad (19)$$

Thus, plasma shielding of the bound electrons is taken into account by limiting the argument of the Bessel function.

(2) Interaction With Free Electrons

For heated target materials, the atoms become ionized, and stopping due to free electrons must be considered. The free electron stopping power is calculated from

$$\left(\frac{dE}{dx}\right)_e = \frac{\rho(x)}{m_I} S_f(V), \quad (20)$$

with

$$S_f(V) = \frac{2\pi e^4 Z_B^2 \bar{Z}}{mV^2} F(\xi) \left\{ \ln \left(1 + \frac{D^2}{b^2}\right) + \ln \left(1 + 4\xi^2\right) \right\} \quad (21)$$

where \bar{Z} is the average charge of the target ions, D is the Debye shielding length, and

$$\xi = (m_B v^2 / 2kT)^{1/2}, \quad (22)$$

where kT is the electron temperature, and

$$F(\xi) = \text{erf}(\xi) - 2\xi e^{-\xi^2} / \sqrt{\pi}. \quad (23)$$

The quantity b is the minimum impact parameter for electron-ion scattering and is given by

$$b = \text{MAX} \left\{ \frac{Z_B e^2}{mV^2}, \frac{h}{2mV} \right\}, \quad (24)$$

i.e., the maximum of either the classical or quantum-mechanical impact parameter defined by the uncertainty principle.

The first term in $S_f(V)$ is the short range ion-electron binary-encounter scattering term and is taken from the work of Campbell¹⁹, who adapted it from Brueckner and Brysk²⁰. The second term is the polarization term and is taken from Pines and Bohm²¹. For distances larger than D , the plasma acts as a continuous medium, and distant collisions cause loss of energy by the excitation of plasma oscillations, which appear as an oscillating wake behind the projectile.

(3) Interaction with Plasma Ions

For stopping power due to the plasma ions, an expression taken from Campbell¹⁹ and Mehlhorn²² is used;

$$\left(\frac{dE}{dx}\right)_i = \frac{\rho(x)}{m_I} S_i(V), \quad (25)$$

where

$$S_i(V) = \frac{4\pi e^4 Z_B^2 \bar{Z}^2}{m_I V^2} \ln \Lambda F(\xi) \quad (26)$$

$$\text{where } \xi^2 = m_I V^2 / 2kT_i, \quad (27)$$

$$F(\xi) = \text{erf}(\xi) - \frac{2}{\sqrt{\pi}} \left(1 + \frac{m_I}{m_B}\right) \xi e^{-\xi^2} \quad (28)$$

$$\ln \Lambda = (1/2) \ln (1 + b_{\max}^2 / b_{\min}^2). \quad (29)$$

b_{\max} is set equal to D , and b_{\min} is given by

$$b_{\min} = \text{MAX} \left\{ \frac{Z_B \bar{Z}}{\mu m_p V^2}; \frac{h}{2\mu m_p V} \right\} \quad (30)$$

where m_p is the proton mass, and

$$\mu = \frac{m_B m_I}{m_B + m_I}. \quad (31)$$

(4) Enhanced Stopping Power From Collective Effects

The stopping power of a dense ion beam can differ from the sum of single particle stopping powers. One way in which this can occur is

through phase mixing of the polarization wakes produced in the ambient medium by the beam particles. The magnitude of this particular effect is similar to that given by McCorkle and Iafrate²³ for electron beams,

$$S_b = S_o (1 + 2\pi n_B a^3/3) \quad (32)$$

where S_b is the enhanced stopping power, S_o is the single particle stopping power, n_B is the beam number density and a is the ratio of the beam velocity and local plasma frequency

$$a = v_B / \omega_{pe} \quad (33)$$

For the case considered below, a 1 MeV proton beam with a flux $n_B v_B = 10^{26} \text{ cm}^{-2} \text{ sec}^{-1}$ on a solid density aluminum target, the correction to the stopping power is quite small.

II. RESULTS

The interaction of a monoenergetic 1 MeV proton beam with a planar aluminum slab of 15 μm thickness is treated in this investigation. A slab thickness of 15 μm is chosen because this distance corresponds to the range of a 1 MeV proton in cold, solid density aluminum.²⁴ Hence, the beam is totally stopped within the slab and should deposit all of its energy within the target. The beam is assumed to consist of a square-shaped pulse of 10 nanosecond duration with a flux of 10^{26} protons/cm²-sec. The beam intensity on target is $1.6 \times 10^{13} \text{ W/cm}^2$, which is comparable to the intensities available with current devices. These calculations were made on the CRAY computer at LANL.

In an earlier report,²⁵ the results of a similar calculation, which employed a probabilistic radiation transport formalism as described in Section I, were given. It was postulated that the probabilistic method had over-estimated the bound-free and free-free radiative cooling of the slab, since it becomes difficult to calculate continuum opacities accurately with the probabilistic model when they become very large. Some limited calculations carried out with the more accurate hybrid model, described

above, confirmed these concerns. Thus, the present coupled hydrodynamic-radiation transport calculation was carried out using the hybrid scheme. This is the first time the hybrid method has been employed in a full production calculation. Previously, it was used for post-processing profiles generated with the probabilistic or multifrequency methods, and for checking the accuracy of probabilistic treatments.

The cost of a full multifrequency production calculation would be prohibitive. The aluminum atomic model used in this study contains about 140 lines; properly resolving them with perhaps ten frequencies per line would require 1400 frequencies in addition to those required for treatment of the continuum. However, a probabilistic treatment of line radiation transport remains viable in the present case. Although this treatment will not provide details of the emitted line profiles, it will accurately describe radiation energetics.

Hence, the hybrid scheme, while sacrificing spectral detail, permits a cost effective self-consistent hydrodynamic-radiation transport calculation to be performed for the ion beam-target interaction study.

Figure 2 shows density profiles at various times within the evolution of the interaction. A striking feature is the spreading of the target plasma and the corresponding density decrease with time. From an initial width of 15 cm and a density of 2.7 grams/cm³, the target has become about 0.3 cm wide with densities of the order of 10⁻² grams/cm³ at 9.8 nsec just before the proton beam is turned off. The density gradient smooths out, and the plasma becomes more uniform with time.

Figure 3 shows corresponding profiles of temperature. At these densities and temperatures, the major contribution to beam stopping comes from the free electrons. Indeed, at the times shown in Figs. 2 and 3, the beam is entirely stopped in the low density, high temperature side of the plasma. The back side of the target is heated primarily through radiation transport, which is substantially larger than the effect of thermal conduction.

Figure 4 shows profiles of density and temperature at 14.8 nsec, 4.8 nsec after the proton beam has been shut off. The plasma is now about 0.52 cm wide and is becoming more uniform. While the temperature of most of the

plasma has fallen considerably since beam cutoff, the back surface temperature has only dropped a few eV. The density is becoming uniform.

Figure 5 shows the energy history of the plasma through 14.8 nsec. Note that the total energy deposited becomes constant at 10 nsec when the beam shuts off. At early times, the energy in the plasma is approximately equal to the deposited energy; at 5 nsec, the radiated energy amounts to about 20% of the deposited energy; beyond this point, the fraction of the deposited energy retained by the plasma decreases. By 10 nsec, more than 40% of the deposited energy has been radiated away, and by 14.8 nsec, more than half the deposited energy has been radiated away. Figure 5 also shows the energy partitioning in the plasma. Up until 10 nsec, all of the components are growing, but beyond this point, the ionization and thermal energies decrease as the plasma cools. The kinetic energy continues to grow as the plasma expands. By 12 nsec, the radiated energy surpasses the energy retained within the plasma. At times greater than 12 nsec, the plasma shows a net loss in energy due to radiative cooling.

Calculated emission spectra from the front and rear surfaces of the plasma at 1.76 nsec are shown in Figs. 6 and 7. At this early time, radiative cooling is not a significant factor as may be seen from Fig. 5. There is much more energy in the front spectrum, where the temperature is higher. Due to the large optical depths at photon energies between 0.01 keV and 1.0 keV, radiation from the hotter, less dense regions does not reach the back side; most of the rear side emission arises from the plasma near the rear surface.

Figures 8 and 9 show calculated emission spectra from the front and rear sides of the plasma at 9.8 nsec. Again, there is more radiated power coming out of the hotter, less dense front surface than the cooler, more dense rear surface. Free bound emission from the L edges is high at the front (beam) edge, but due to large optical depths in the 0.3 keV region, this emission is greatly attenuated at the rear side. Around 1.0 keV, the optical depths become of order unity, and the emission rises, then falls again due to K-edge absorption. Emissions from several L-shell lines can be seen in both spectra, as can K line emissions in the 1.5 keV to 2.0 keV range. There are more K lines appearing on the front side.

Figures 10 and 11 show front and back emission spectra at 14.8 nsec. These spectra are more similar than the front and rear spectra at 9.8 nsec due to the fact that the plasma is more uniform at this time. From 0.01 keV up to about 0.25 keV, the spectra are nearly identical; above this frequency, the rear spectrum is greatly reduced with respect to the front spectrum. This is due to the increased density near the rear surface and the large optical depths at frequencies from about 0.25 keV to 1.0 keV; i.e., for frequencies about 0.1 keV and up to about 0.25 keV, emissions from the front and rear surfaces have significant contributions from deep within the plasma, but for frequencies greater than 0.25 keV, nearly all the emission from both sides originates near the surface due to the large optical depths. At these frequencies, the front surface radiates more energy. Due to the cooler temperatures, K-shell lines are missing from these spectra.

IV. COMPARISON WITH CALCULATION WITHOUT RADIATION TRANSPORT

One might question the need for a fully self-consistent hydro-dynamic-radiation transport calculation. Would it not suffice to perform a hydrodynamic calculation, and post-process the resulting temperature-density profiles to obtain the radiation? Alternatively, could not a simple radiation transport model suffice in a calculation of this sort? Certainly there are problems where one of these alternatives would be adequate. However, for the current beam-target interaction problem, accurate radiation transport is essential. To demonstrate this, an identical simulation with fully self-consistent ionization physics, but without radiative cooling or transport was carried out.

Comparisons of density and temperature profiles at various times for both sets of calculations are given in the following figures.

Figure 12 shows comparison profiles at 6 nsec. On the beam side of the plasma, the "purely hydrodynamic plasma" (PHP) calculation yields much higher temperatures and correspondingly lower densities. This clearly demonstrates the effects of radiative cooling on the hydrodynamic response. The PHP is wider at this time due to the absence of radiative cooling.

Figure 13 shows similar comparisons at 10 nsec. Similar comments regarding temperature and density can be made here. In this situation, the

back surface of the plasma with radiation included has expanded further than the PHP case as opposed to the situation in Fig. 12. This is chiefly due to the effects of radiative heating on the rear surface.

Figure 14 presents comparison profiles at 15 nsec, 5 nsec after the beam has been shut off. Similar observations regarding temperature and density can be made; the PHP still produces the wider plasma. A striking feature of Fig. 15 is the relative uniformity of the profiles for the radiation case as compared to the PHP case. The PHP case still retains steep gradients near the rear surface, while the radiation-hydro plasma is approaching an isothermal condition with fairly uniform density.

Figure 15 gives the energy history of the plasma along with the energy partitioning for the PHP case. The plasma energy is equal to the deposited energy at all times. The thermal energy is much higher than in Fig. 5 for the radiation-hydro case; this indicates that radiation cooling occurs at the expense of the plasma thermal energy. This is also indicated by the much higher temperatures in the PHP curves in Figs. 12-14. The ionization energies are not very different in the two calculations. The PHP case has higher kinetic energy at later times; this accounts for the greater widths of the hydrodynamic plasma.

These comparisons of the PHP and hydro-radiation transport cases clearly establish the importance of radiation transport effects in hot plasmas. Any realistic treatment of hot plasmas must include self-consistent radiation effects.

V. COMPARISON WITH LASER-TARGET INTERACTION

It is of interest to make some qualitative comparisons with a simulation of a laser-aluminum target interaction at roughly the same incident energy intensity. Duston, et. al.²⁶ studied the interaction of a 1.06 micron laser beam at an intensity of 10^{13} W/cm² and a long pulse length (3 nsec full width at half maximum) with an 8 μ m thick aluminum foil. Fig. 16 is taken from that study.

In the laser case, after the initial blow off plasma is formed, the beam does not penetrate into the target beyond the critical density

surface, whereas the ion beam penetrates deep into the target, at least at early times. In both cases, the dense part of the plasma at later times is heated predominantly by radiation transport rather than thermal conduction. The laser case shows much lower densities and higher temperatures on the front side of the plasma, whereas on the backside the laser case shows much higher density and lower temperatures. Also, by comparing Figs. 2 and 16, it can be seen that the laser beam calculation produces much sharper density and temperature gradients. These results substantiate the view that proton beams are more efficient than laser beams for heating up the interior and backside of targets; this is due to deeper penetration into the target by the ion beams.

VI. SUMMARY

A fully self consistent, one-dimensional treatment of the interaction of a one-MeV proton beam with an aluminum slab has been presented. A fully self-consistent hydrodynamic-ionization-radiation transport model was used. The atomic populations as functions of density and temperature were obtained from a collisional-radiative-equilibrium assumption. Radiation transport was calculated using a hybrid scheme.

Profiles of the plasma density, temperature, and average charge resulting from these calculations have been presented. Comparisons with calculations omitting radiation transport show that radiation can significantly affect plasma evolution, leading to substantially different temperature and density profiles, and must be included in any self-consistent treatment of ion beam-target interactions.

Qualitative comparisons of the ion beam-slab interaction with a treatment²⁶ of a laser-beam slab interaction shows that the laser produces higher temperatures and lower densities on the front (beam) side of the plasma, while the proton beam is more efficient at heating up the back side due to deeper penetration into the target.

Since these treatments of the beam-target interaction are one-dimensional, energy flow normal to the direction of the beam has been neglected; in addition, self-field effects have not been considered. These

effects could reduce the range significantly, and alter the magnitude and shapes of the plasma profiles given here. A two-dimensional hydrodynamic code is under development and it is planned to use this model in the beam-target interaction study when it becomes available.

Even with these limitations, however, the above results should be useful in particle beam lethality and vulnerable studies.

AD-A142 825

ADVANCED CONCEPTS THEORY ANNUAL REPORT 1983(U) NAVAL
RESEARCH LAB WASHINGTON DC J P APRUZESE ET AL.
18 MAY 84 NRL-MR-5330 SBI-AD-E000 573

2/2

UNCLASSIFIED

F/G 7/4

NL

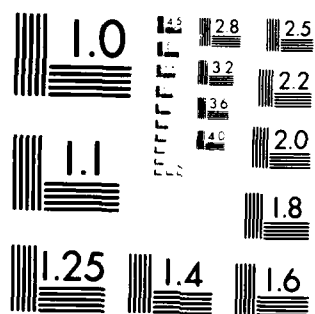
END

DATE

FILED

8-84

DTIC



MICROCOPY RESOLUTION TEST CHART
NATIONAL BUREAU OF STANDARDS-1963-A

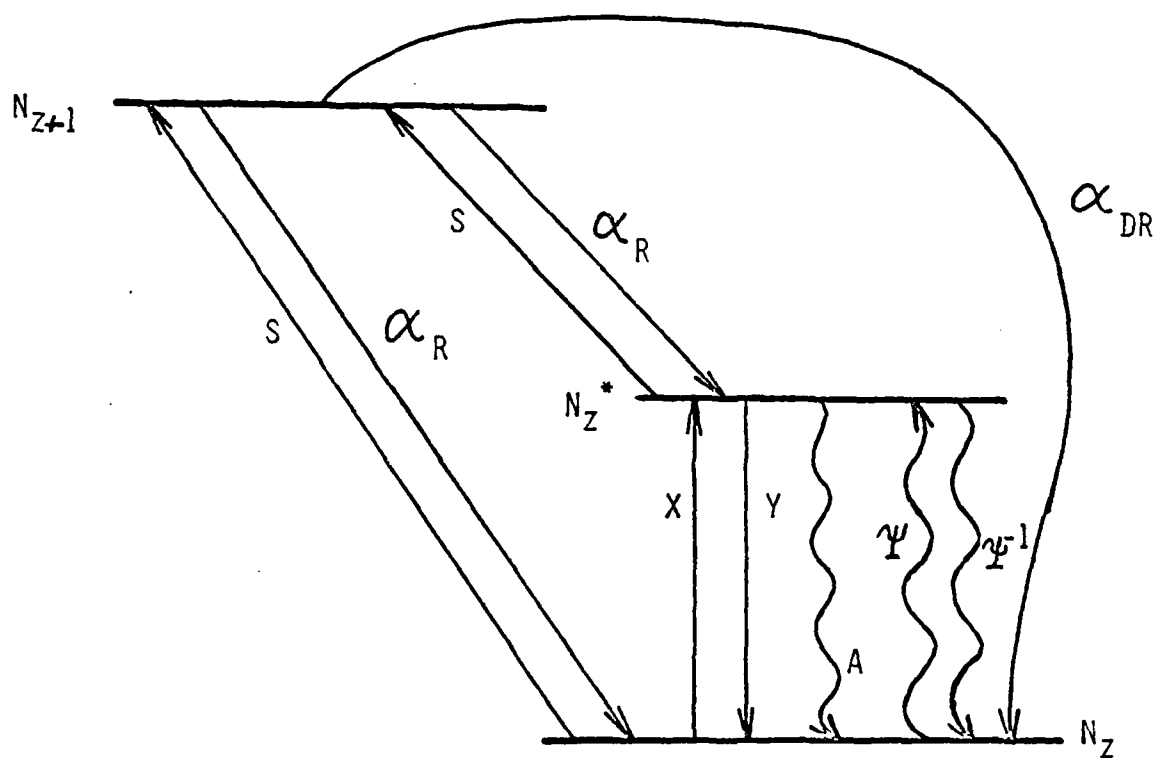


Fig. 1. Simple three-level diagram used to depict the atomic processes included in this ionization model. S is collisional and photoionization, α_R is radiative recombination and three-body recombination, α_{DR} is dielectronic recombination, X is electron collisional excitation, Y is collisional deexcitation, A is spontaneous decay, and ψ and ψ^{-1} are stimulated absorption and emission.

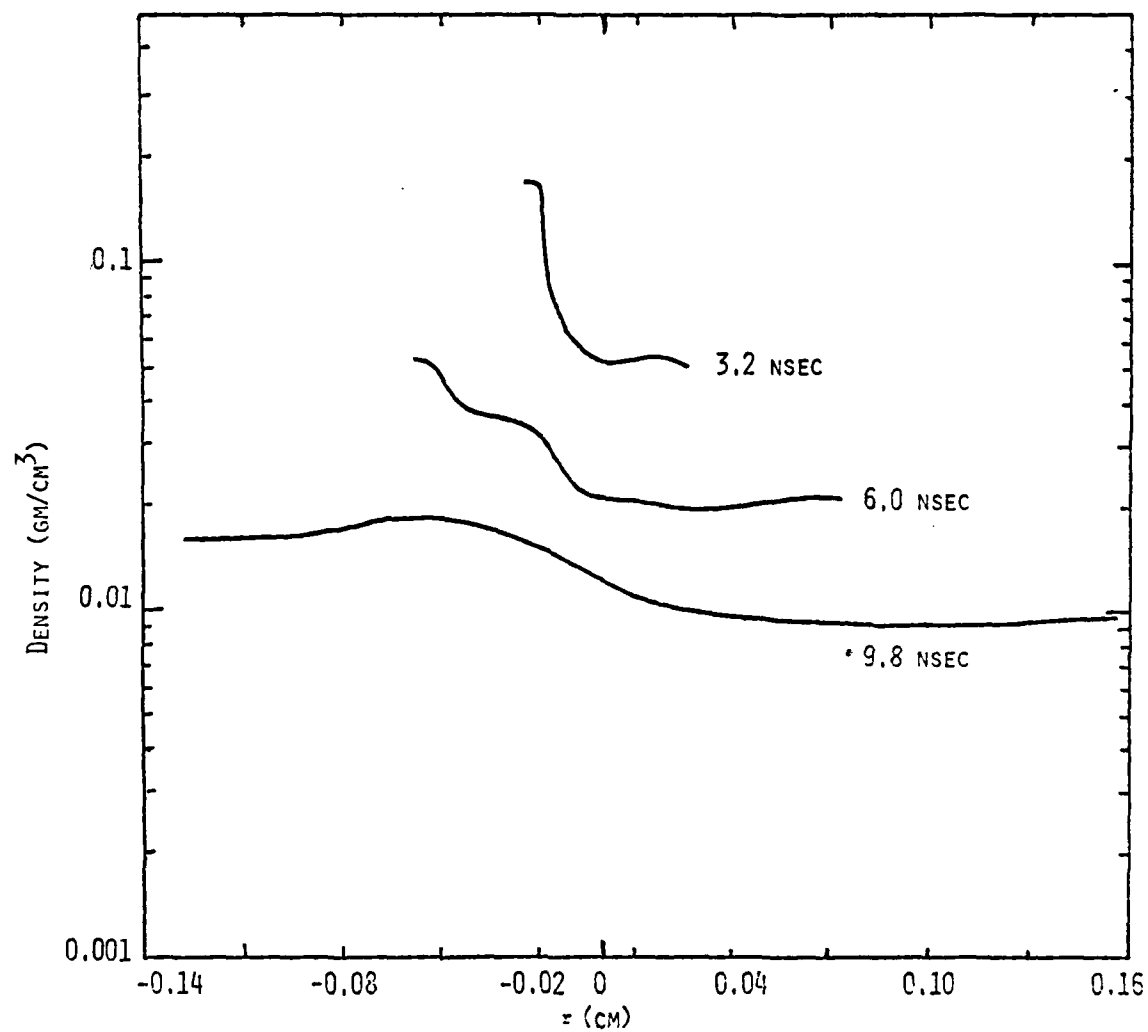


Fig. 2. Density profiles at 3.2 nsec, 6.0 nsec, and 9.8 nsec.

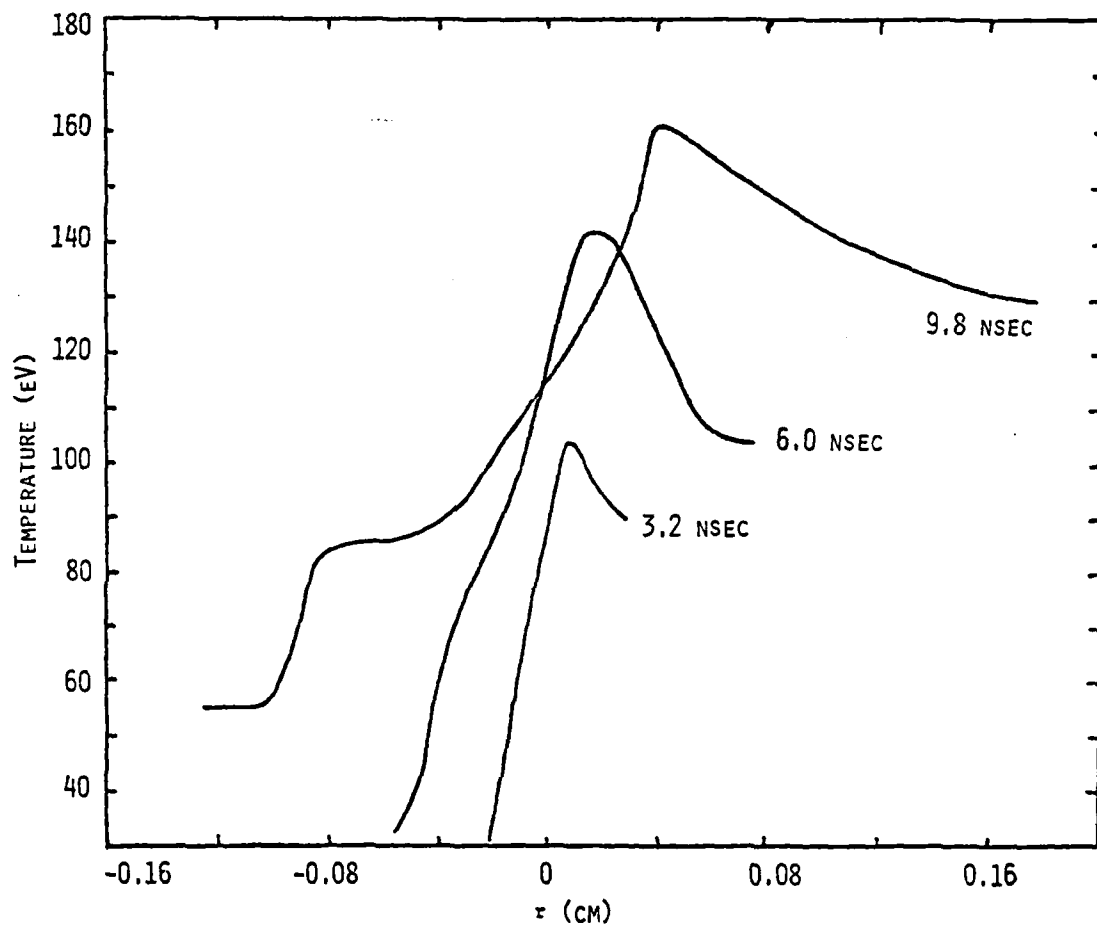


Fig. 3. Temperature profiles at 3.2 nsec, 6.0 nsec, and 9.8 nsec.

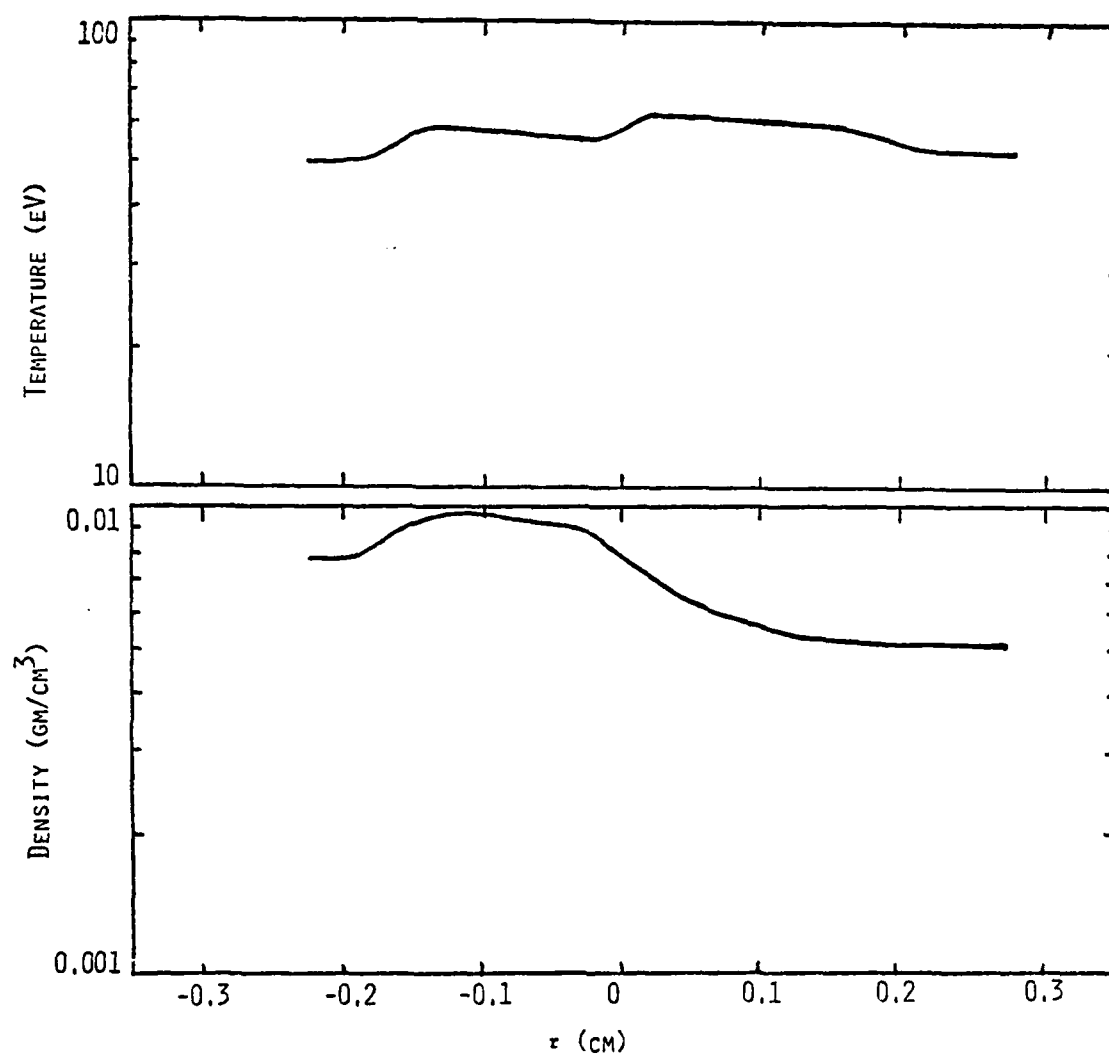


Fig. 4. Density and temperature profiles at 14.8 nsec.

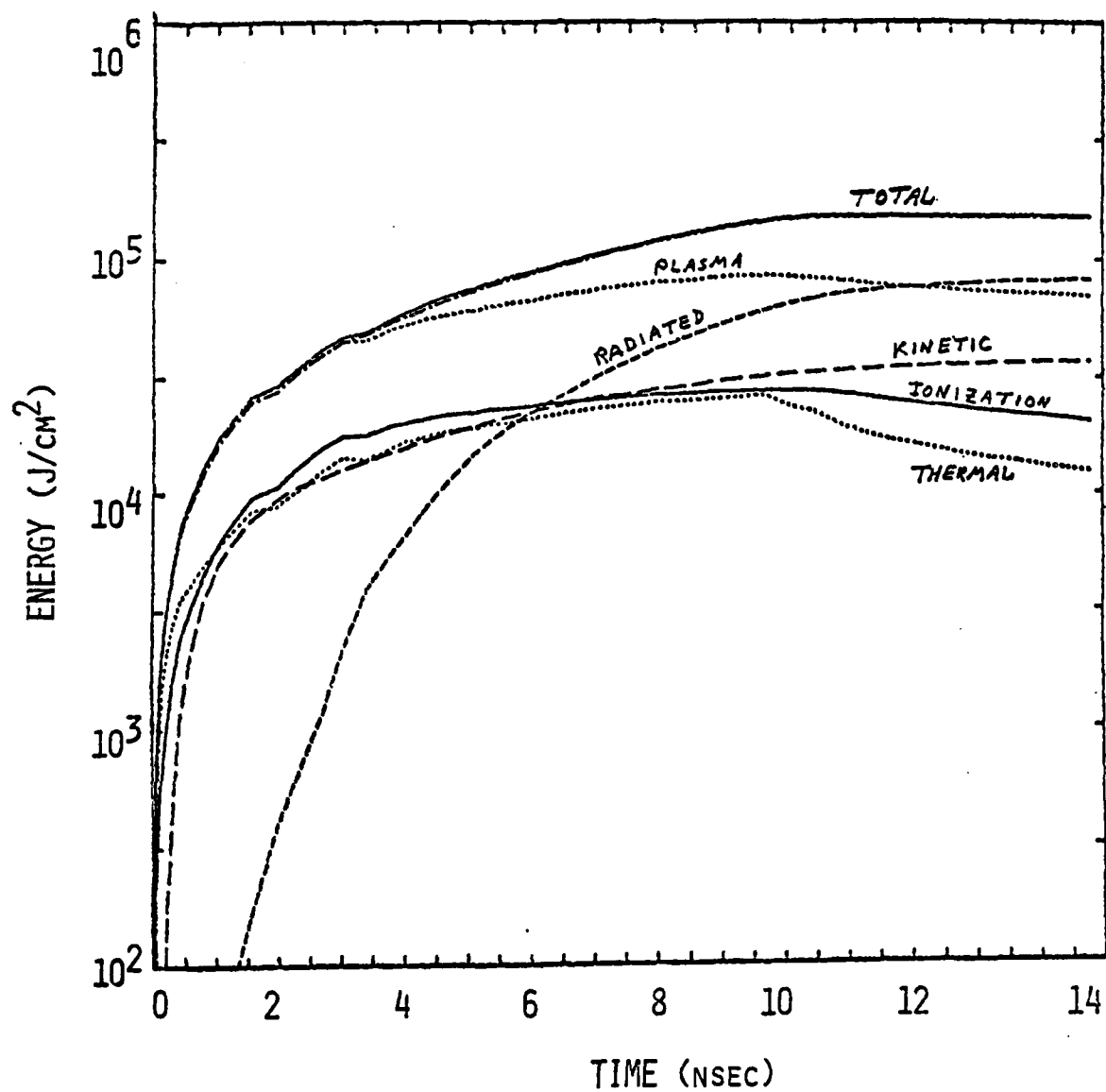


Fig. 5. Energy history of the beam-target interaction when radiation transport is included.

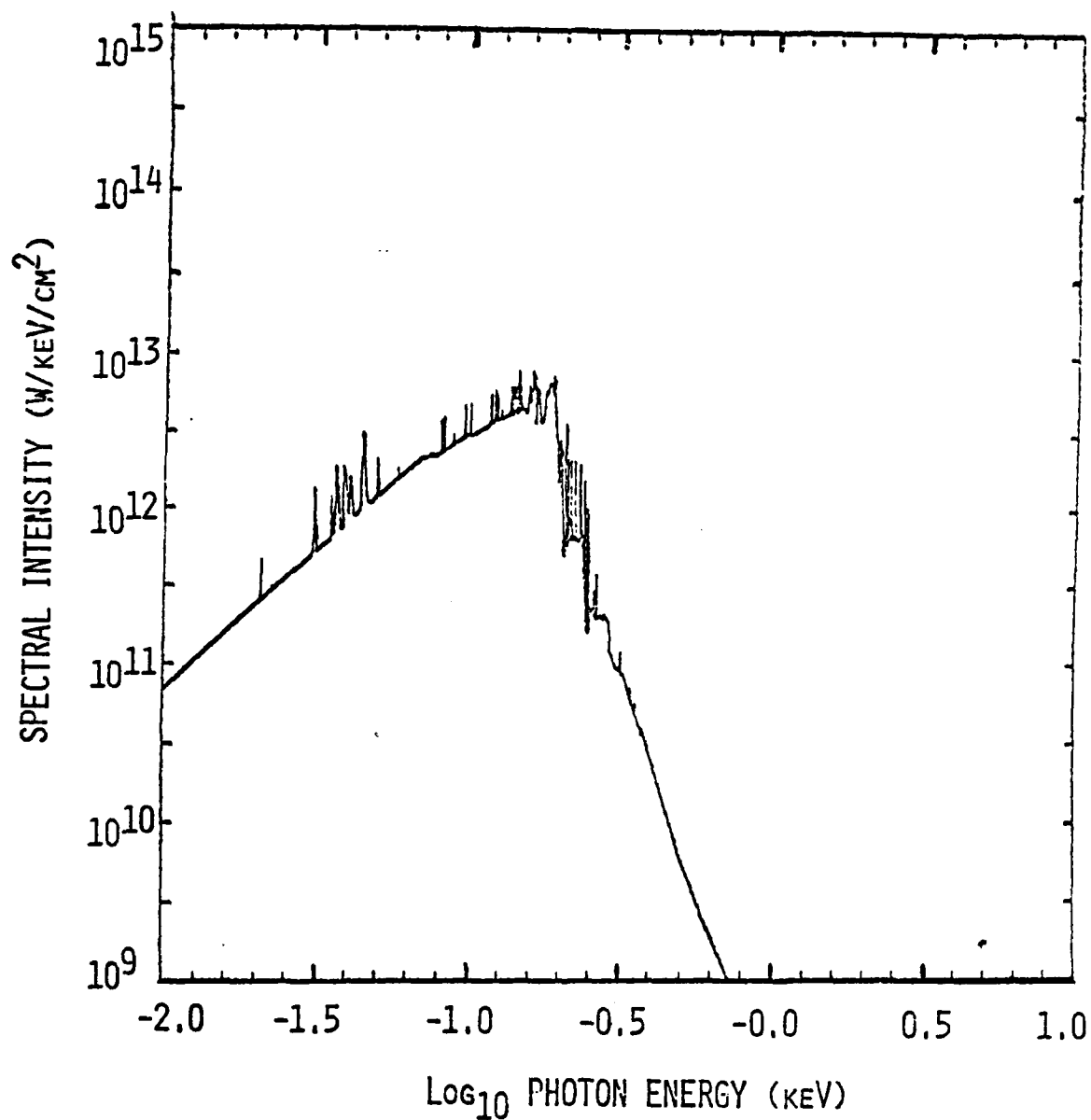


Fig. 6. Front side spectrum at 1.78 nsec.

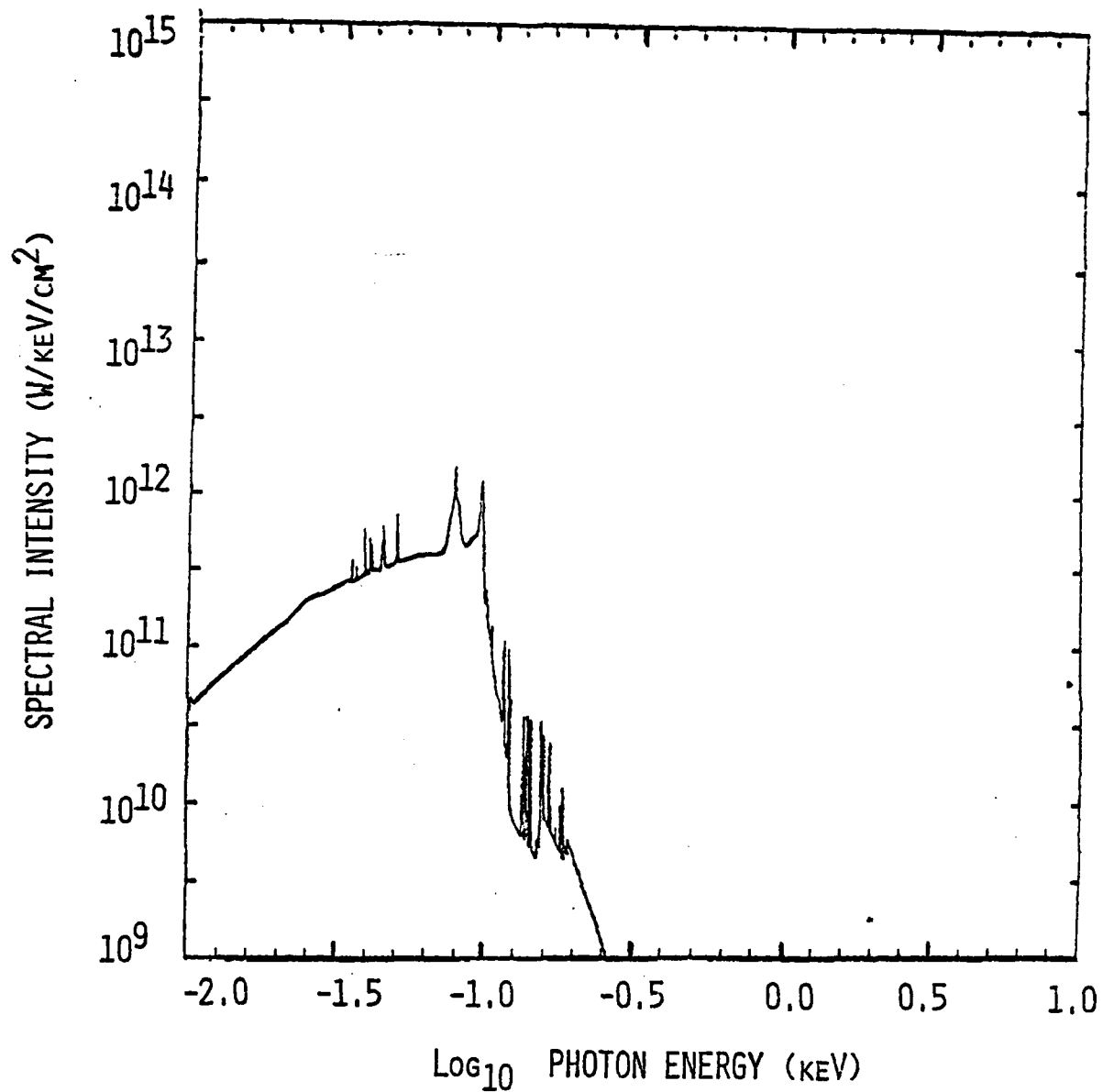


Fig. 7. Rear side spectrum at 1.78 nsec.

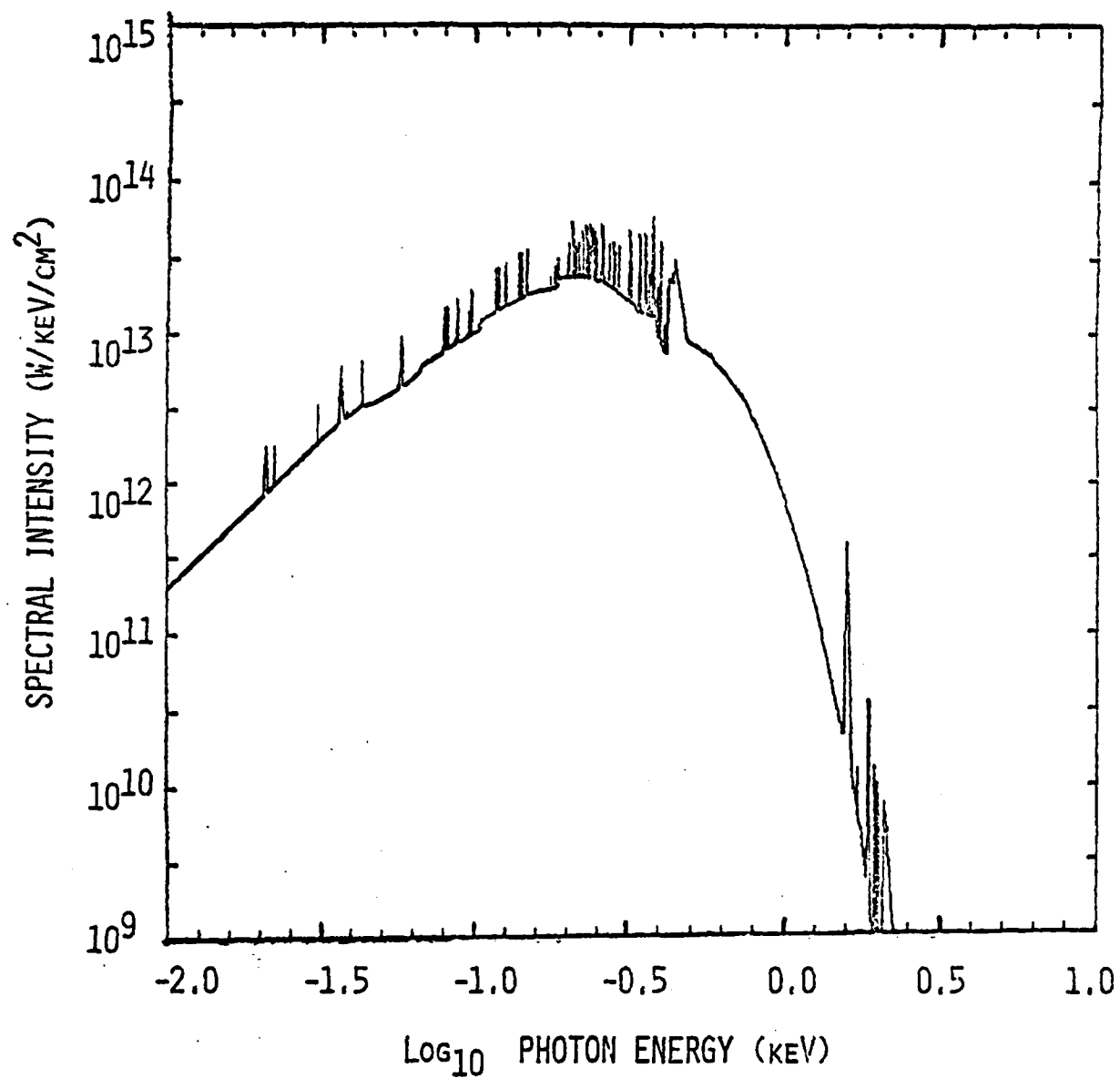


Fig. 8. Front side spectrum at 9.8 nsec.

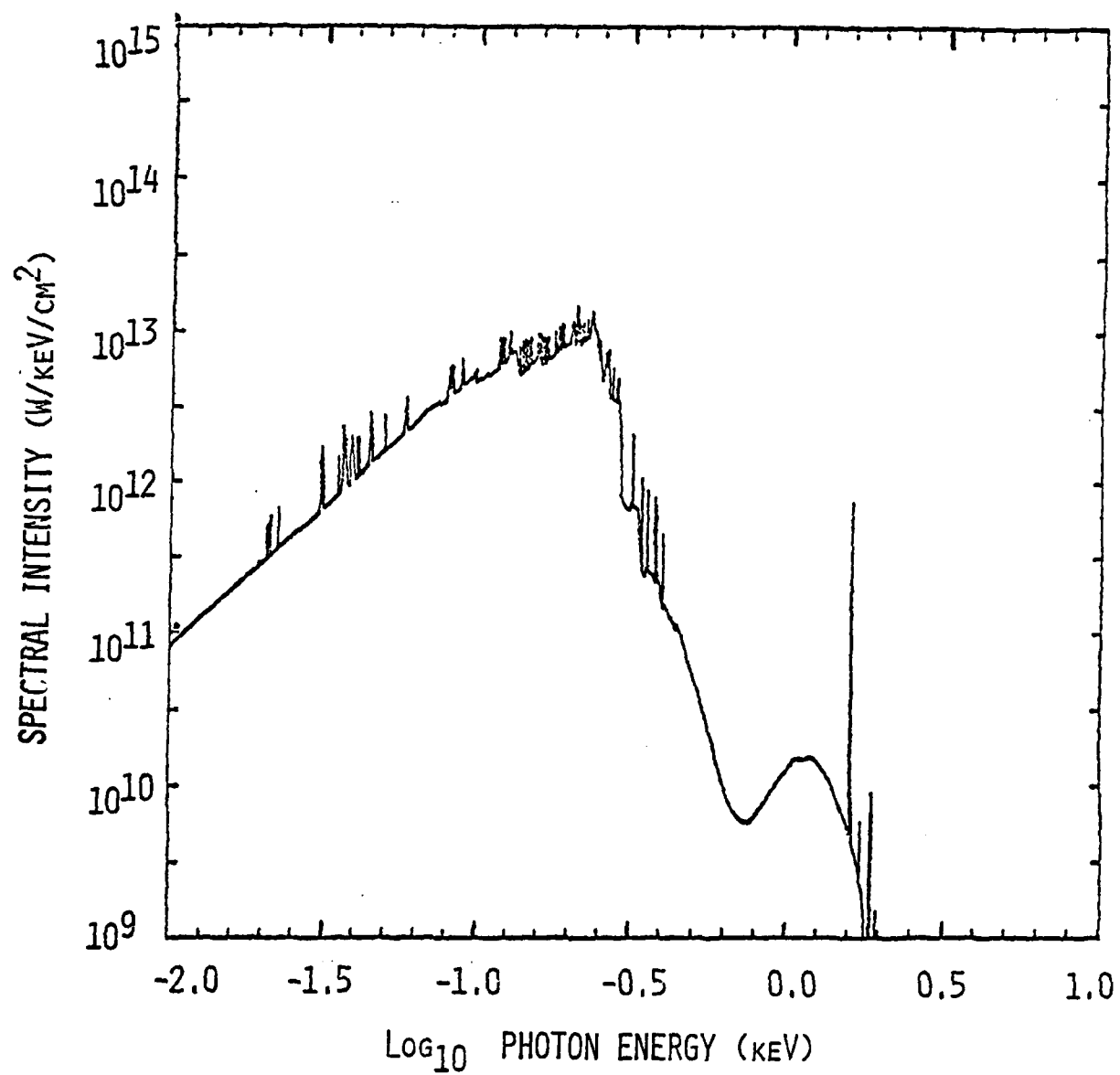


Fig. 9. Rear side spectrum at 9.8 nsec.

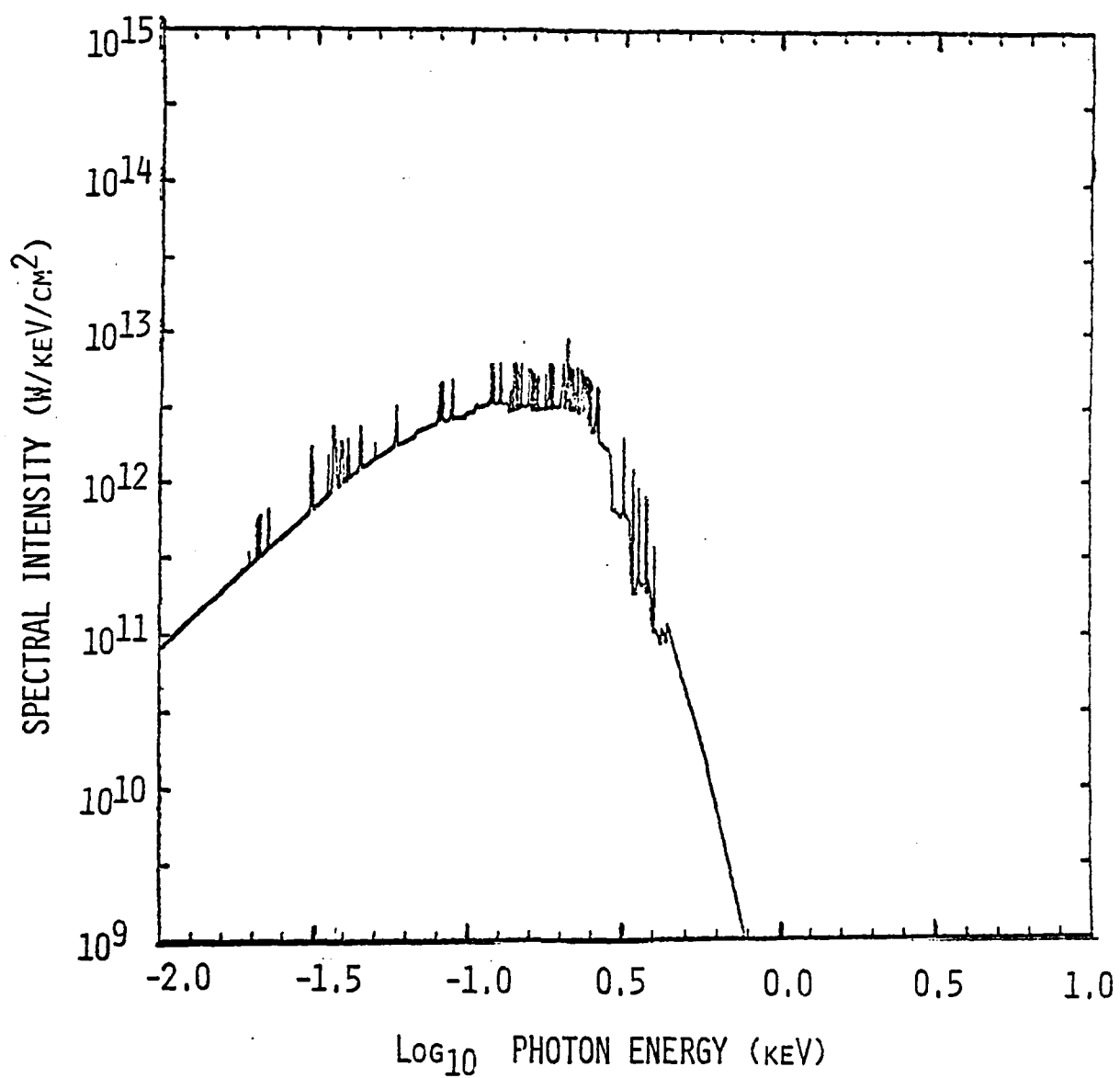


Fig. 10. Front side spectrum at 14.8 nsec.

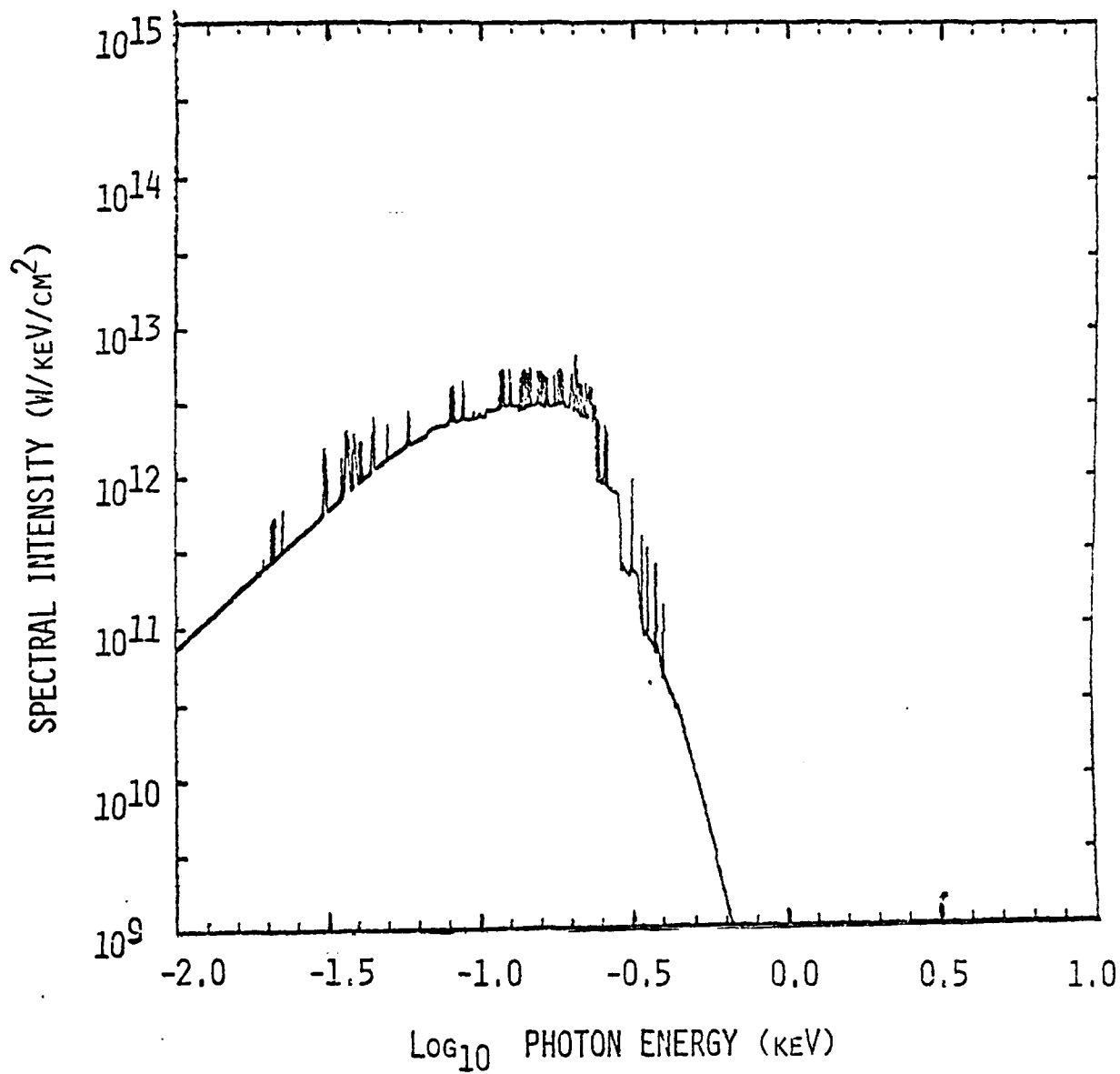


Fig. 11. Rear side spectrum at 14.8 nsec.

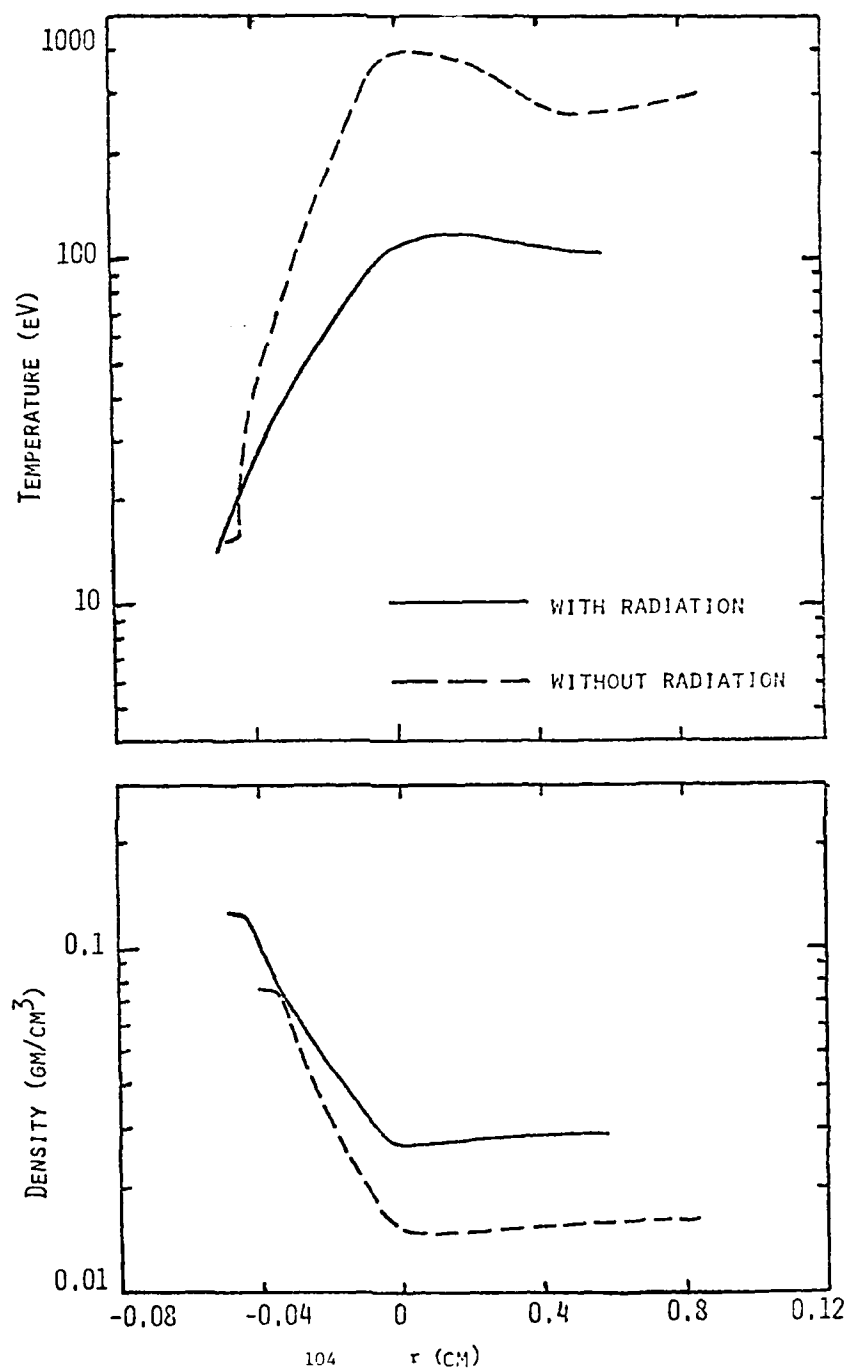


Fig. 12. Comparison of density and temperature profiles at 6.0 nsec with and without radiation transport.

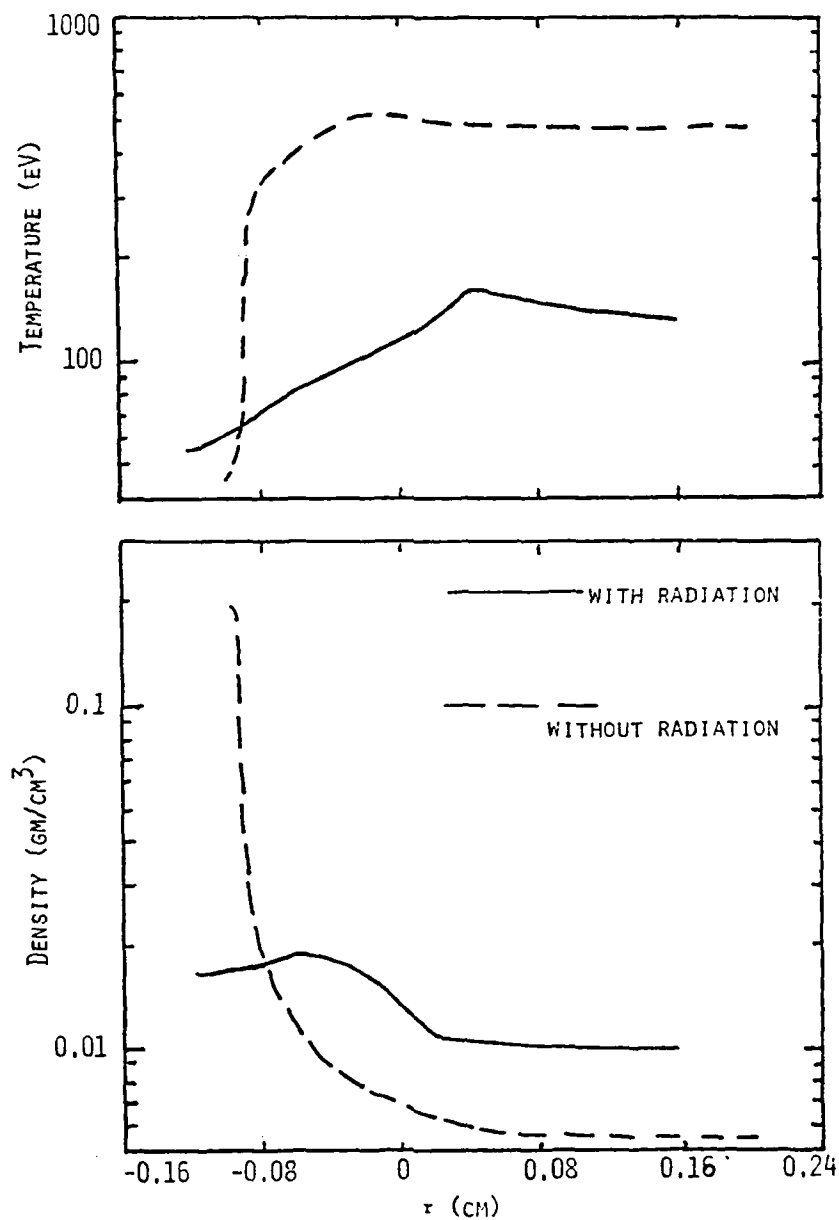


Fig. 13. Comparison of temperature and density profiles at 10 nsec with and without radiation transport.

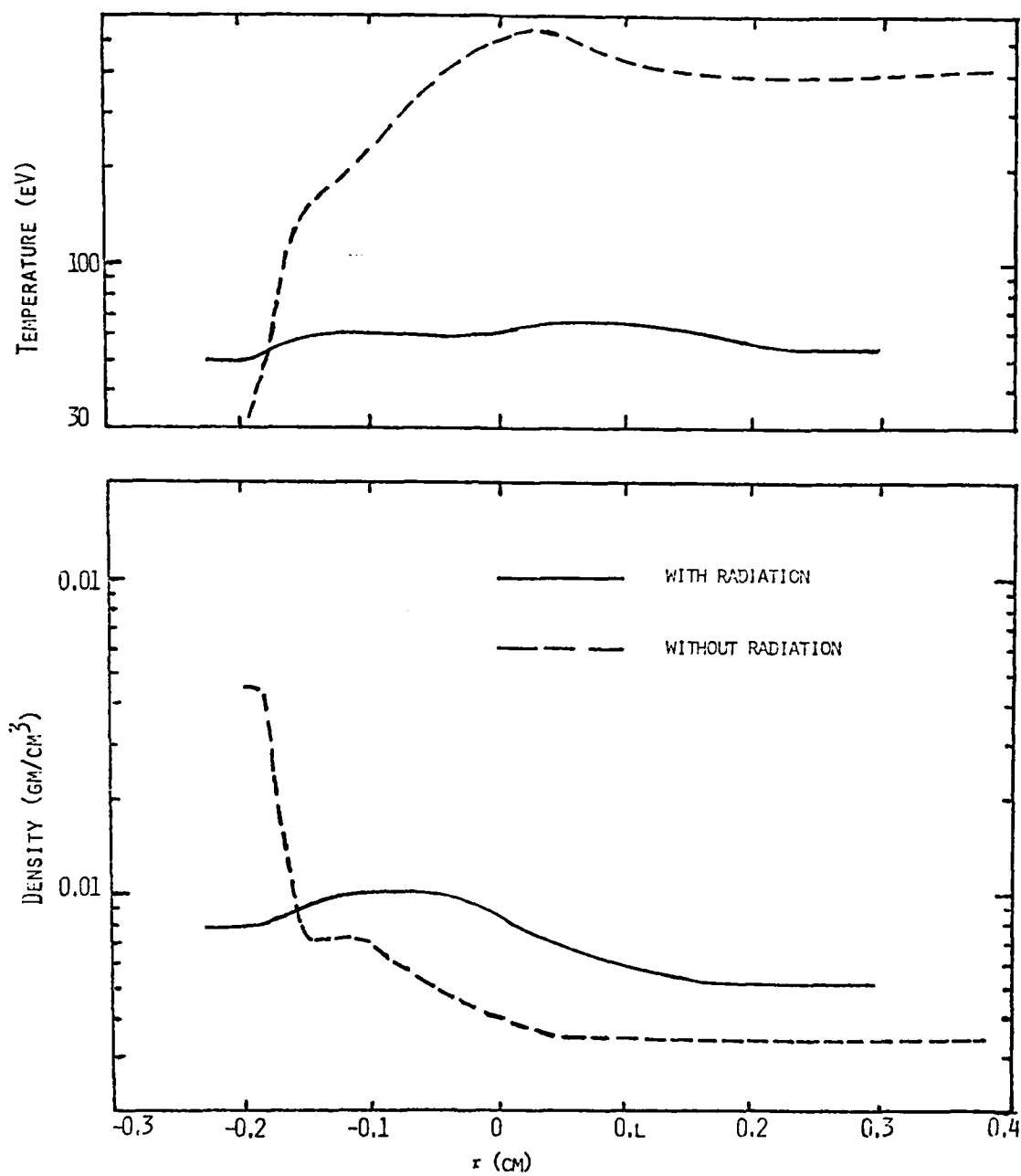


Fig. 14. Comparison of temperature and density profiles at 15 nsec with and without radiation transport.

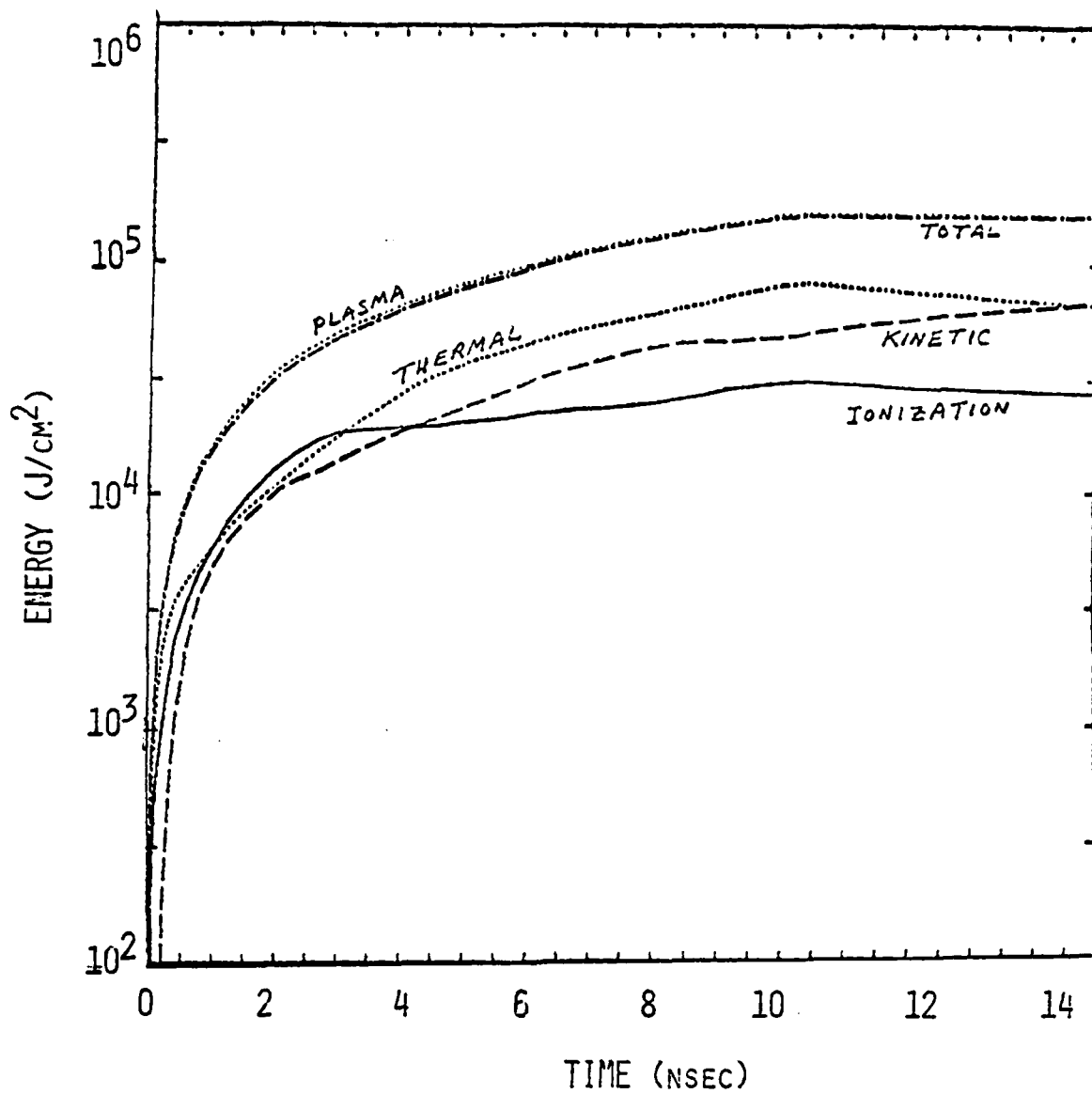


Fig. 15. Energy history of the beam-target interaction when radiation transport is omitted.

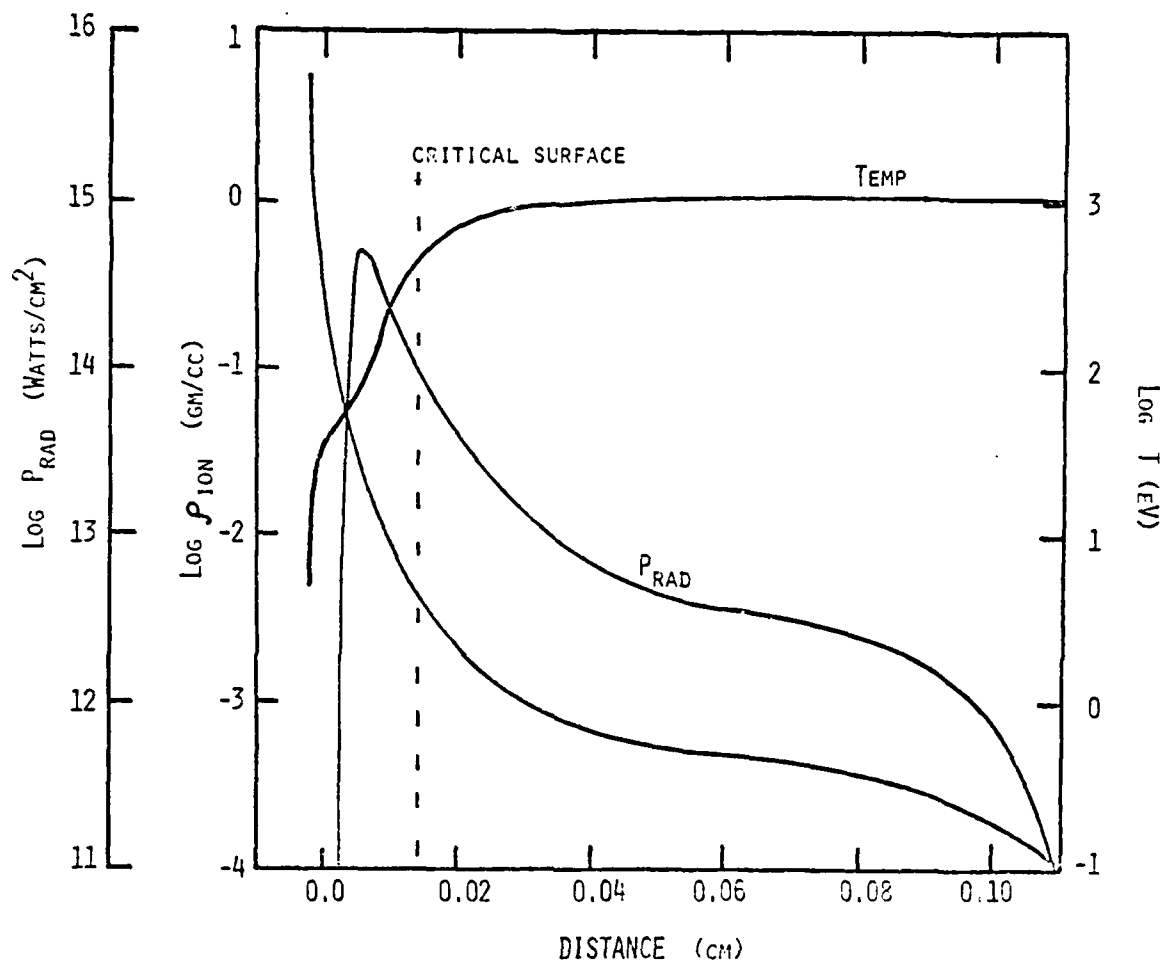


Fig. 16. Temperature, density, and radiative cooling profiles at about 5 nsec in the laser heated foil case (Ref. 26).

References

1. J. P. Boris and D. Book, J. Comp. Phys 11, 38 (1969).
2. D. R. Bates, A. E. Kingston and R. W. P. McWhirter, Proc. R. Soc. A267, 297 (1962).
3. A. Burgess, H. P. Summers, D. M. Cochrane and R. W. P. McWhirter, Mon. Not. R. Astron. Soc. 179, 275 (1977).
4. V. L. Jacobs, J. Davis, P. C. Kepple and M. Blaha, ASTROPHYS. J. 211, 605 (1977).
5. W. J. Karzas and B. Latter, ASTROPHYS. J. Suppl. Ser. 6, 167 (1961).
6. V. L. Jacobs and J. Davis, Phys. Rev. A 18, 697 (1978).
7. J. Davis, P. C. Kepple, and M. Blaha, J. Quant. Spectrosc. Rad. Transfer 16, 1043 (1977).
8. E. Oran and J. Davis, J. Appl. Phys. 45, 2480 (1974).
9. D. Duston and J. Davis, Phys. Rev. A23, 2602 (1981).
10. J. P. Apruzese, J. Davis, D. Duston, and R. W. Clark, Phys. Rev. A. 29, 246 (1984).
11. J. P. Apruzese, J. Davis, D. Duston, and K. G. Whitney, J. Quant Spectrosc. Rad. Transfer 23, 475 (1980); J. P. Apruzese, J. Quant Spectrosc. Rad. Transfer 25, 419 (1981).
12. J. P. Apruzese, P. C. Kepple, K. G. Whitney, J. Davis, and D. Duston, Phys. Rev. A24, 1001 (1981).
13. F. Biggs and R. Lighthill, Sandia Laboratories Report No. SC-RR-710507 (1971).
14. E. Clementi and C. Roetti, At. Data and Nucl. Data Tables 14, 177 (1974).
15. J. E. Rogerson, NRL Memo Report 4485 (1981).
16. R. K. Nesbet and J. F. Ziegler, Appl. Phys. Lett. 31 810 (1977).
17. J. W. Zink, Phys. Rev. 176 279 (1968).
18. J. D. Jackson, Classical Electrodynamics, John Wiley and Sons Inc. (1962) p. 643.
19. P. M. Campbell, "Fast Ion Energy Loss in Dense Plasmas", (1980) (Private communication).
20. K. A. Brueckner and H. Brysk, KMSF Document KMSF - U7 (1971).
21. D. Pines and D. Bohn, Phys. Rev. 85, 338 (1952).
22. T. A. Mehlhorn, Sandia Laboratories Report No. Sand 80-0038 (1980).

23. R. A. McCorkle and G. J. Iafrate, Phys. Rev. Lett. 39, 1263 (1977).
24. L. C. Northcliffe and R. F. Schilling, Nuclear Data Tables A7, 233 (1970).
25. DNA Quarterly Report, (from Plasma Radiation Branch) April-June 1983.
26. D. Duston, R. W. Clark, J. Davis, and J. P. Apruzese, Phys. Rev. A27, 1441 (1982).

F. Enhanced Radiation Sources

I. INTRODUCTION

Exploring schemes and configurations for enhanced plasma radiation will require a more complete understanding of the nature of radiation matter interactions. Since we are interested in producing x-rays for simulation purposes, it is irrelevant whether the x-rays are incoherent or coherent. Naturally, because of the power requirements and the lack of a working x-ray laser, combined with the relative ease of producing incoherent x-ray radiation all of DNA's sponsored research efforts in this area have potential application. However, it appears that it may be possible to develop a coherent x-ray source using current gas puff technology. It is in this atmosphere that we have investigated a scheme that could be implemented experimentally using pulse power technology. Since our initial goal is to understand the physics issues and determine the plasma conditions favorable to produce a coherent x-ray source, we have simplified things by assuming a laser driven system. In future investigations the laser will be replaced by a PRS.

For many years now, there have been a variety of proposed schemes suggesting ways to create a population inversion and subsequent gain in the x-ray region¹⁻⁷. One such scheme involves the radiated flux from one plasma pumping on another plasma to create conditions which result in coherent radiation in the soft x-ray region⁴⁻⁷. There are several cases where the coincidence between the pumping and absorbing lines is close enough to merit strong consideration as a possible lasing combination. Two such schemes utilizing a Si XIII - Al XII system and a Na X - Ne IX system are modeled in detail in reference 1 (hereafter, referred to as ADW). The Na - Ne scheme is particularly interesting because the lines match to better than one part in 10^4 at a wavelength of 11 μ .

The proper conditions in the Na - Ne system is created by "tuning" the hydrodynamics and thermal properties of the two component plasma⁷. This tuning acts both to create a tenuous neon blowoff and to provide an energy source to heat the sodium. The sodium subsequently acts as a backlighting flashlamp for the neon.

For instance, absorption of a laser operating at low intensity can ablate the neon at a low temperature, typically about 100 eV. Second, energy can be deposited into the sodium backlighter and locally heat this region. This energy deposition can occur on the opposite side relative to the neon cooling to prevent over heating the neon or it may occur off to the side of the expanding neon plasma plume. The optimum configuration has not yet been determined. The rapid rise in temperature induced by this deposition will then conduct through the sodium and create the proper conditions for photo-pumping the cooler neon. Of course, within a finite time scale this thermal wave propagates through the neon and effectively burns out any inverted population. The plasma system then remains in an isothermal condition.

Several constraints in this problem are brought about by considering the plasma properties which are needed to achieve gain in a resonant photo-pumped medium¹. First the line absorption coefficients are linear in ion density. Therefore, for a fixed optical depth, the width d of the ablated neon can be scaled as $d = A/N_1$ where A is a constant and N_1 is the ion density. The maximum optical depth before significant reduction in population inversion occurs has been determined by Hagelstein² to be approximately 5. The approximation given in ADW is that this requires an ablated blowoff with a scale length not greater than 10 μm for ion densities on the order of 10^{20} cm^{-3} . This scale length can increase to greater than 0.1 cm for ion number densities on the order of 10^{18} cm^{-3} . For the inverted levels discussed in ADW, the gain coefficient for the Ne IX $2p^1P - 3d^1D$ and $2p^1P - 4d^1D$ transitions peak near an ion density of 10^{20} cm^{-3} . The gain subsequently drops off dramatically to less than unity at 10^{18} cm^{-3} . However, the gain for the $3d^1D - 4f^1F$ transition peaks near 10^{19} cm^{-3} and is still greater than 10 at 10^{18} cm^{-3} .

A second constraint is placed on the temperatures of the two plasmas. The temperature of the lasing neon must be kept low enough to prevent burnout of the Ne IX population. At a density of 10^{20} cm^{-3} the maximum fractional population of Ne IX occurs at approximately 65 eV in the presence of the pump radiation. On the other hand, the pumping plasma (in this case Na) is most favorable when it is an optically thick plasma with a kinetic temperature of about 300 eV. In short, one would like a hot dense pumping plasma irradiating a cooler, optically thin lasing plasma¹.

As indicated above, the density requirements for the 3-2 and 4-2 transitions differ from the requirements of the 4-3 transition. Therefore, we can separate the following discussion into two parts. First, we will examine the 3-2 and 4-2 scaling requirements. We consider cryogenic neon with density 1.2 gm/cm^3 on the outside of a sodium sample. This neon layer is subsequently ablated off the sodium to dynamically set up the proper plasma conditions for the photo-pumped system. In order to prevent photon trapping and meet the conditions given above, a layer of $2.79 \times 10^{-2} \text{ } \mu\text{m}$ of Ne is needed. This assumes a uniform blowoff density of 10^{20} cm^{-3} with a width of $10 \text{ } \mu\text{m}$. If we assume that the Ne plasma is initially produced by laser absorption, then the ablation velocity will be on the order of 10^7 cm/sec . At these velocities expansion out to $10 \text{ } \mu\text{m}$ occurs on a time scale of roughly 100 psec. Both the pumping material and the lasing material must reach the proper conditions for gain in this time frame. The strong dependence of the gain coefficient¹ on density results in the existence of a window of approximately 10 nsec before the 3-2 and 4-2 transitions yield a gain coefficient less than unity.

On the other hand, the 4-3 transition has a gain coefficient of 1.0 at approximately 10^{16} cm^{-3} and hence, the expansion time can be up to 1 μsec . At peak gain (i.e., 10^{19} cm^{-3}) this allows 1 nsec for the blowoff to develop. Again this assumes a uniform expansion velocity of 10^7 cm/sec .

We now consider the propagation of the thermal wave from the area of energy absorption in the sodium through the neon plasma. The electron heat flux is given by

$$q = -\kappa \nabla T \quad (1)$$

The conductivity κ can be written in the form

$$\kappa = C n_e k \lambda_c v_e \quad (2)$$

where C is a constant of order unity, n_e is the electron density, k is Boltzmann's constant, λ_c is the electron-ion collision mean free path, and v_e is the electron thermal speed. Equation (1) can be rewritten in the form

$$\vec{q} = C n_e k T_e \left(\frac{\lambda_c}{L_T} \right) v_e (-\vec{e}_T) \quad (3)$$

where L_T is the temperature gradient length and \vec{e}_T is given by $\vec{\nabla}T/|\vec{\nabla}T|$. If $L_T < \lambda_c$, the heat flux will be carried in the direction $-\vec{e}_T$ at a rate which is greater than the electron thermal speed. This is an unphysical result and indeed, the derivation of the conductivity given by Eq. (2) is predicated on the assumption that $\lambda_c < L_T$. This problem of steep gradients has been studied extensively in the laser fusion literature⁸⁻¹¹. The approach which has been used most often in connection with this difficulty has been to limit the flux \vec{q} whenever $\lambda_c > f L_T$ to

$$\vec{q} = n_e k T_e f v_e (-\vec{e}_T) \quad (4)$$

where f , the so-called "flux limiter", is less than one⁸⁻¹². Therefore, we can base our estimate of the propagation speed of the thermal wave on some limited value of v_e . The ratio of the flux limited value of the thermal wave speed to the sound speed c_s will be given by

$$\frac{f v_e}{c_s} = 148 \frac{f}{Z^{1/2}} \quad (5)$$

where we have used the atomic weight for neon and an adiabatic index of 5/3. Recent theoretical and experimental results have put the value of f close to 0. for laser power levels which are appropriate for our conditions¹³⁻¹⁵. Assuming Ne IX (i.e., $Z = 8$), Eq. (4) gives $f v_e = 5.2 c_s$ and the thermal wave be expected to overtake the expanding plasma up to Mach numbers of roughly 5.

Max, McKee, and Mead¹² have studied in detail the properties of steady state flow beyond the critical surface in plasmas created by laser absorption and the dependence of this flow on the flux limiter in spherical geometry. While this analysis is not appropriate for the conditions which occur during the early phase of rapid energy deposition, it is helpful in gaining insight into the physics during the later absorption and blowoff stages. The parameters discussed above fall into the "semi-saturated" regime. That is, the heat flux will be classical up to the point $M = 1.76$ where M is the Mach number¹². This point will occur at 1.38 critical surface radii¹². Beyond that point heat flow will be flux limited and the

Mach number will increase slowly thereafter. Hence, we can expect that the thermal front should overtake the expanding plasma. Based on these results, we can make an estimate of the propagation time for the thermal wave to penetrate the Ne plasma. If we assume an ion density of 10^{19} cm^{-3} and choose an optical depth of 5, then the total distance to be traversed in the neon plasma is approximately $100 \text{ } \mu\text{m}$. If the value given above for fv_e is chosen with $c_s = 1.5 \times 10^7 \text{ cm/sec}$, the thermal wave will propagate halfway into the neon in 70 psec . This puts a rough limit on the time span over which effective gain will be achieved.

In order to assess the validity of this scheme in a more detailed fashion, we are using a 1-D Lagrangian hydrodynamics code to model the Na-Ne plasma combination. This code treats the electron and ion temperatures separately. Equation of state models are used for both the ions and the electrons. Of course, because of the low densities, the plasma in the subcritical region can be expected to behave nearly as a perfect gas. We have assumed a uniform planar slab of sodium coated with a thin layer of neon. The Ne layer contains enough particles so that for a uniform expansion of width $10 \text{ } \mu\text{m}$ the ion density will be 10^{20} cm^{-3} . At solid or liquid densities this gives a submicron layer of uniform thickness. The initial zone sizes are varied in the transition region so that the zonal masses are nearly equal at the Na-Ne interface. Velocities and positions are defined on zone boundaries. Density, temperature, and laser absorption are computed at zone centers. The electron temperature is flux limited according to Eq. (4).

In a preliminary fashion, we have been able to make an estimate of the gain produced by this configuration at each of these wavelengths using the line center gain coefficient curve for the Ne IX $3d^1D - 4f^1F$ transition given in ADW and making the simplifying assumption of a 65 eV plasma temperature in the neon. This also assumes that the flux at line center for the $11 \text{ } \text{\AA}$ pump is $6.6 \times 10^3 \text{ ergs}/(\text{cm}^2\text{-sec-Hz})$ as inferred from a microballoon implosion at Rochester¹³. We consider the case where energy is deposited locally in the sodium by a high powered laser after ablating the neon with a low energy prepulse. The sodium target is considered to be several microns thick. There is no absorption in the neon of this high powered pulse. This, might represent laser absorption from the side or it might crudely represent laser absorption occurring in the rear side of the

sodium (i.e., the side away from the neon). At the present time, we are conducting a more detailed analysis where the high power laser is absorbed non-locally (i.e., inverse bremsstrahlung) in the rear side of a thin sodium slab. Results from this study will be given in a future report. An average density can be computed by taking the Ne plasma length at the time when the 200 eV thermal front propagates out of the system for 10^{13} w/cm² deposition into the sodium.

We have performed post processed CRE (Collisional Radiative Equilibrium)¹⁴ calculations of the sodium pump intensity which would be incident upon the neon lasing material for a representative snapshot density and temperature profile. This has allowed us to compare with the Na pumping line intensity reported in ADW of $6.6 \times 10^3 \frac{\text{ergs}}{\text{cm}^2 \text{-sec-Hz}}$ at line center obtained from the Rochester implosion experiment¹⁸. The two profiles are shown in Figure 1. Self absorption is evident at line center but not in the Rochester profile which showed no self absorption within the experimental resolution¹ of 1.5 eV. Except for the self absorption, this line profile closely resembles the microballoon implosion profile of the Rochester experiment.

The results of ADW (where the neon is assumed fully bathed in pump radiation) showed that the Rochester profile produced a peak gain coefficient of nearly 200 cm^{-1} . Proportionality arguments would then yield a gain coefficient of roughly 2.5 cm^{-1} , for the case shown where the neon is illuminated on only one side by the sodium.

We must stress, that extensive modeling of the pulse, deposition configuration, and sodium target thickness will most likely produce different line center intensities incident on the neon plasma than the crude results reported here. Of crucial importance will be the correct modeling of the energy deposition into the sodium backlighter and the subsequent interaction with the neon plasma. Using the best gain coefficient projected from post processing the Na pump, it appears that gain may be measurable in an experiment of this type. It may, however, be more advantageous to employ a cylindrical or spherical configuration in order to provide compressional heating of the pump to the requisite temperature at high density.

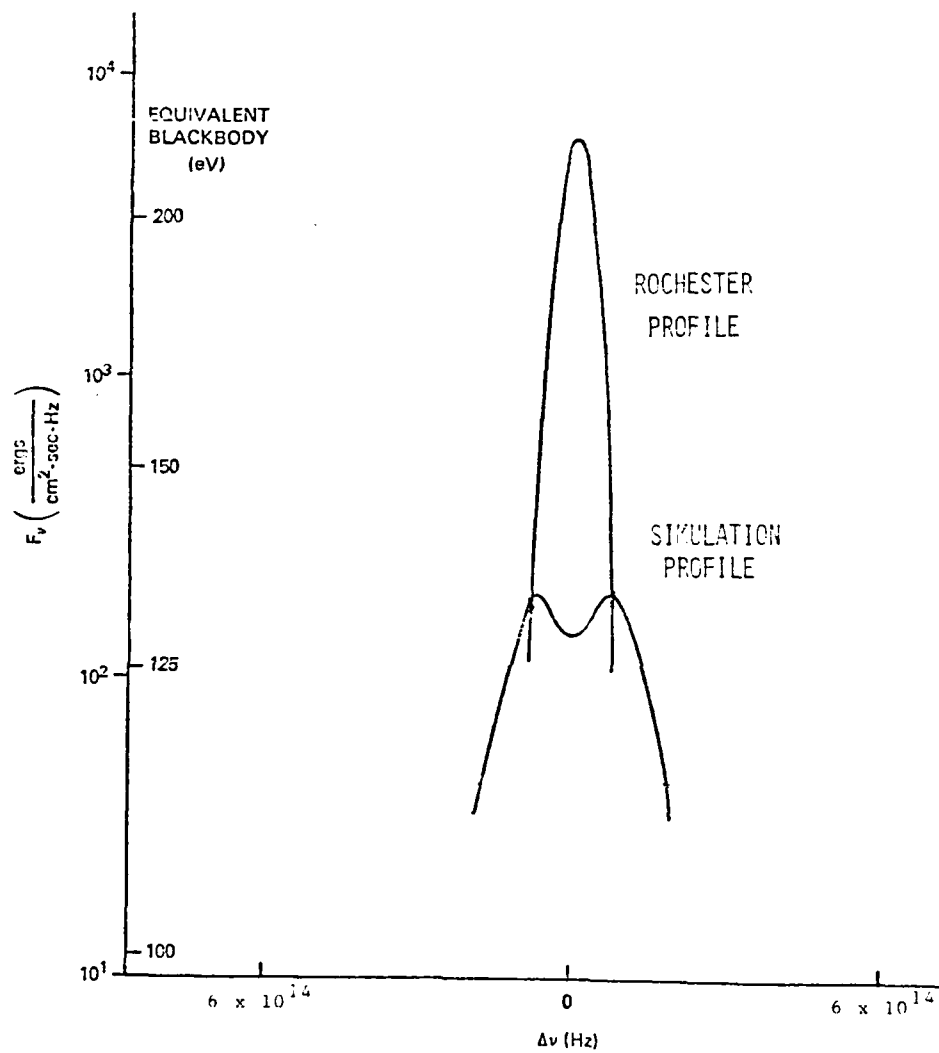


Figure 1

References

1. J.P. Apruzese, J. Davis, and K.G. Whitney, J. Appl. Phys. 53, 4020 (1982).
2. P.L. Hagelstein, Lawrence Livermore National Laboratory Report UCRL-53100 (1981).
3. R. W. Waynant and R. C. Elton, Proc. IEEE 64, 1059(1976).
4. A. V. Vinogradov, I. I. Sobel'man, and E. A. Yukov, Sov. J. Quant. Electron. 5, 59(1975).
5. B. A. Norton and N. J. Peacock, J. Phys. B 8, 189(1975).
6. J. P. Apruzese, and J. Davis, and K. G. Whitney, J. Phys. B. 11, L643(1978).
7. R. Elton, private communication (1983).
8. C.E. Max and C.F. McKee, Phys. Rev. Lett. 39,1336 (1977).
9. R.L. Morse and C.W. Nielson, Phys. Fluids 16,909 (1973).
10. R.C. Malone, R.L. McCrory, and R.L. Morse, Phys. Rev. Lett. 34,721 (1975).
11. W.M. Manheimer and H.H. Klein, Phys. Fluids 18,1299 (1975).
12. C.E. Max, C.F. McKee, and W.C. Mead, Phys. Fluids 23,1620 (1980).
13. B. Yaakobi, D. Steel, E. Thorsos, A. Hauer, and B. Perry, Phys. Rev. Lett. 39, 1526(1977).
14. J. P. Apruzese, P. C. Kepple, K. G. Whitney, J. Davis, and D. Duston, Phys. Rev. A 24, 1001(1981).

DISTRIBUTION LIST

Assistant to the Secretary of Defense Atomic Energy Washington, D.C. 20301 ATTN: Executive Assistant	1 Copy
Director Defense Advanced Research Projects Agency 1400 Wilson Blvd. Arlington, Virginia 22209 ATTN: J. Mangano Lt. Col. R. Gullickson	1 copy each
Defense Technical Information Center Cameron Station 5010 Duke Street Alexandria, Va 22314	2 copies
Director Defense Intelligence Agency Washington, D.C. 20301 ATTN: DT-IB R. Rubenstein	1 Copy
Director Defense Nuclear Agency Washington, D.C. 20305 ATTN: DDST ATTN: TITL ATTN: RAEV ATTN: STVI	1 copy 4 copies 1 copy 1 copy
Commander Field Command Defense Nuclear Agency Kirtland AFB, New Mexico 87115 ATTN: FCPR	1 Copy
Chief Field Command Livermore Division Department of Defense P.O. Box 808 Livermore, CA 94550 ATTN: FCPRL	1 Copy

Director
Joint Strat TGT Planning Staff
Offutt AFB
Omaha, Nebraska 68113
ATTN: JSAS

1 Copy

Undersecretary of Defense
for RSCH and ENGRG
Department of Defense
Washington, D.C. 20301
ATTN: Strategic and Space Systems (OS)

1 Copy

Deputy Chief of Staff for RSCH DEV and ACQ
Department of the Army
Washington, D.C. 20301
ATTN: DAMA-CSS-N

1 Copy

Commander
Harry Diamond Laboratories
Department of the Army
2800 Powder Mill Road
Adelphi, MD 20783
ATTN: DELHD-N-NP
ATTN: DELHD-R J. Rosado
ATTN: DELHD-TA-L (Tech. Lib.)

1 copy each

U.S. Army Missile Command
Redstone Scientific Information Center
Attn: DRSMI-RPRD (Documents)
Redstone Arsenal, Alabama 35809

3 Copies

Commander
U.S. Army Missile Command
Redstone Arsenal, Alabama 35898
ATTN: DRCPM-PE-EA

1 copy

Commander
U.S. Army Nuclear and Chemical Agency
7500 Backlick Road
Building 2073
Springfield, VA 22150
ATTN: Library

1 copy

Commander
U.S. Army Test and Evaluation Command
Aberdeen Proving Ground, MD 21005
ATTN: DRSTE-EL

1 Copy

Commanding Officer Naval Intelligence Support Center 4301 Suitland Road, Bldg. 5 Washington, D.C. 20390 ATTN: NISC-45	1 Copy
Commander Naval Weapons Center China Lake, CA 93555 ATTN: Code 233 (Tech. Lib.)	1 Copy
Officer in Charge White Oak Laboratory Naval Surface Weapons Center Silver Spring, MD 20910 ATTN: Code R40 ATTN: Code F31	1 copy each
Air Force Weapons Laboratory Kirtland AFB, New Mexico 87117 ATTN: SUL ATTN: CA ATTN: APL ATTN: Lt. Col. Generosa	1 copy each
Deputy Chief of Staff Research, Development and Accounting Department of the Air Force Washington, D.C. 20330 ATTN: AFRDQSM	1 Copy
Space and Missile Systems Organization/IN Air Force Systems Command P. O. Box 92960 Worldway Postal Center Los Angeles, CA 90009 ATTN: IND D. Muskin (Intelligence)	1 Copy
HQ BMO/MM Norton AFB, CA 92409 ATTN: Col. J. M. Wells	1 Copy
Space and Missile Systems Organization/SK Air Force Systems Command Post Office Box 92960 Worldway Postal Center Los Angeles, CA 90009 ATTN: SKF P. Stadler (Space Comm. Systems)	1 Copy

AVCO Research and Systems Group
201 Lowell Street
Wilmington, MA 01887
ATTN: Library A830

1 Copy

BDM Corporation
7915 Jones Branch Drive
McLean, Virginia 22101
ATTN: Corporate Library

1 Copy

Boeing Company
P. O. Box 3707
Seattle, WA 98134
ATTN: Aerospace Library

1 Copy

The Dikewood Corporation
1613 University Bldv., N.E.
Albuquerque, New Mexico 8710
ATTN: L. Wayne Davis

1 Copy

EG and G Washington Analytical
Services Center, Inc.
P. O. Box 10218
Albuquerque, New Mexico 87114
ATTN: Library

1 Copy

General Electric Company
Space Division
Valley Forge Space Center
P. O. Box 8555
Philadelphia, PA 19101
ATTN: J. Peden

1 Copy

General Electric Company - Tempo
Center for Advanced Studies
816 State Street
P.O. Drawer QQ
Santa Barbara, CA 93102
ATTN: DASIAC

1 Copy

Institute for Defense Analyses
1801 N. Beauregard St.
Alexandria, VA 22311
ATTN: Classified Library

1 Copy

IRT Corporation
P.O. Box 81087
San Diego, CA 92138
ATTN: R. Mertz

1 Copy

JAYCOR
11011 Forreyane Rd.
P.O. Box 85154
San Diego, CA 92138
ATTN: E. Wenaas

1 Copy

JAYCOR
205 S. Whiting Street, Suite 500
Alexandria, VA 22304
ATTN: R. Sullivan

1 Copy

KAMAN Sciences Corp.
P. O. Box 7463
Colorado Springs, CO 80933
ATTN: J. Hoffman
ATTN: A. Bridges
ATTN: D. Bryce
ATTN: W. Ware

1 copy each

Lawrence Livermore National Laboratory
University of California
P.O. Box 808
Livermore, California 94550
Attn: DOC CDN for L-153
Attn: DOC CDN for L-47 L. Wouters
Attn: DOC CDN for Tech. Infor. Dept. Lib.

1 copy each

Lockheed Missiles and Space Co., Inc.
P. O. Box 504
Sunnyvale, CA 94086
Attn: S. Taimlty
Attn: J.D. Weisner

1 copy each

Lockheed Missiles and Space Co., Inc.
3251 Hanover Street
Palo Alto, CA 94304
Attn: J. Perez

1 Copy

Maxwell Laboratory, Inc.
9244 Balboa Avenue
San Diego, CA 92123
ATTN: A. Kolb
ATTN: M. Montgomery
ATTN: J. Shannon

1 Copy each

McDonnell Douglas Corp.
5301 Bolsa Avenue
Huntington Beach, CA 92647
ATTN: S. Schneider

1 Copy

Mission Research Corp.
P. O. Drawer 719
Santa Barbara, CA 93102
ATTN: C. Longmire
ATTN: W. Hart

1 Copy each

Mission Research Corp.-San Diego
5434 Ruffin Rd.
San Diego, California 92123
ATTN: Victor J. Van Lint

1 Copy

Northrop Corporation
Northrop Research and Technology Center
1 Research Park
Palos Verdes Peninsula, CA 90274
ATTN: Library

1 Copy

Northrop Corporation
Electronic Division
2301 120th Street
Hawthorne, CA 90250
ATTN: V. Damarting

1 Copy

Physics International Company
2700 Merced Street
San Leandro, CA 94577
Attn: C. Stallings
Attn: S. Wong

1 Copy each

R and D Associates
P.O. Box 9695
Marina Del Rey, CA 90291
ATTN: W. Graham, Jr.
ATTN: P. Haas

1 Copy each

Science Applications, Inc.
P. O. Box 2351
La Jolla, CA 92038
ATTN: J. Beyster

1 copy

Spire Corporation
P. O. Box D
Bedford, MA 01730
ATTN: R. Little

1 copy

SRI International
333 Ravenswood Avenue
Menlo Park, CA 94025
ATTN: S. Dairiki

1 copy

S-CUBED
P. O. Box 1620
La Jolla, CA 92038
ATTN: A. Wilson

1 copy

Texas Tech University
P.O. Box 5404
North College Station
Lubbock, TX 79417
ATTN: T. Simpson

1 copy

TRW Defense and Space Systems Group
One Space Park
Redondo Beach, CA 90278
ATTN: Technical Information Center

1 Copy

Vought Corporation
Michigan Division
38111 Van Dyke Road
Sterling Heights, Maine 48077
ATTN: Technical Information Center
(Formerly LTV Aerospace Corp.)

1 Copy

Naval Research Laboratory
Plasma Radiation Branch
Washington, D.C. 20375

Code 4720	-	50	Copies
Code 4700	-	26	Copies
2628	-	22	Copies

FI
8